# Image-guidance and computational modeling to develop and characterize microwave thermal therapy platforms

by

Pegah Faridi

B.S., Shiraz University, 2012
M.S., Shiraz University of Technology, 2014

AN ABSTRACT OF A DISSERTATION

submitted in partial fulfillment of the requirements for the degree

DOCTOR OF PHILOSOPHY

Mike Wiegers Department of Electrical and Computer Engineering
Carl R. Ice College of Engineering

KANSAS STATE UNIVERSITY
Manhattan, Kansas

2020

# Abstract

This dissertation focuses on the development of magnetic resonance imaging (MRI)-guided microwave thermal therapy systems for driving experimental studies in small animals, and to experimentally validate computational models of microwave ablation, which are widely employed for device design and characterization. MRI affords noninvasive monitoring of spatial temperature profiles, thereby providing a means to to quantitatively monitor and verify delivery of prescribed thermal doses in experimental studies and clinical use, as well as a means to validate thermal profiles predicted by computational models of thermal therapy.

A contribution of this dissertation is the development and demonstration of a system for delivering mild hyperthermia to small animal targets, thereby providing a platform for driving basic research studies investigating the use of heating as part of cancer treatment strategies. An experimentally validated 3D computational model was employed to design and characterize a non-invasive directional water-cooled microwave hyperthermia applicator for MRI guided delivery of hypethermia in small animals. Following a parametric model-based design approach, a reflector aperture angle of 120°, S-shaped monopole antenna with 0.6 mm displacement, and a coolant flow rate of 150 ml/min were selected as applicator parameters that enable conformal delivery of mild hyperthermia to tumors in experimental animals. The system was integrated with real-time high-field 14.1 T MRI thermometry and feedback control to monitor and maintain target temperature elevations in the range of 4 – 5 °C (hypethermic range). 2 - 4 mm diameter targets positioned 1 – 3 mm from the applicator surface were heated to hyperthermic temperatures, with target coverage ratio ranging between 76 - 93 % and 11 – 26 % of non-targeted tissue heated.

Another contribution of this dissertation is using computational models to determine how the fibroids altered ablation profile of a microwave applicator for global endometrial ablation.

Uterine fibroids are benign pelvic tumors located within the myometrium or endometrium,and may alter the profile of microwave ablation applicators deployed within the uterus for delivering endometrial ablation. A 3D computational model was employed to investigate the effect of 1 – 3 cm diameter uterine fibroids in different locations around the uterine cavity on endometrial ablation profiles of microwave exposure with a 915 MHz microwave triangular loop antenna. The maximum change in simulated ablation depths due to the presence of fibroids was 1.1 mm. In summary, this simulation study suggests that 1 – 3 cm diameter uterine fibroids can be expected to have minimal impact on the extent of microwave endometrial ablation patterns achieved with the applicator studied in this dissertation.

Another contribution of this dissertation is the development of a method for experimental validation of 3D transient temperature profiles predicted by computational models of MWA. An experimental platform was developed integrating custom designed MR-conditional MWA applicators for use within the MR environment. This developed platform was employed to conduct 30 - 50 W, 5 - 10 min MWA experiments in ex vivo tissue. Microwave ablation computational models, mimicking the experimental setting in MRI, were implemented using the finite element method, and incorporated temperature-dependent changes in tissue physical properties. MRI-derived Arrhenius thermal damage maps were compared to Model-predicted ablation zone extents using the Dice similarity coefficient (DSC). Mean absolute error between MR temperature measurements and fiber-optic temperature probes, used to validate the accuracy of MR temperature measurements, during heating was in the range of 0.5 – 2.8 °C. The mean DSC between model-predicted ablation zones and MRI-derived Arrhenius thermal damage maps for 13 experimental set-ups was 0.95. When comparing simulated and experimentally (i.e. using MRI)

measured temperatures, the mean absolute error (MAE %) relative to maximum temperature change was in the range 5 % - 8.5 %.

# Image-guidance and computational modeling to develop and characterize microwave thermal therapy platforms

by

Pegah Faridi

B.S., Shiraz University, 2012
M.S., Shiraz University of Technology, 2014

A DISSERTATION

submitted in partial fulfillment of the requirements for the degree

DOCTOR OF PHILOSOPHY

Mike Wiegers Department of Electrical and Computer Engineering
Carl R. Ice College of Engineering

KANSAS STATE UNIVERSITY
Manhattan, Kansas

2020

Approved by:

Major Professor
Punit Prakash

# Copyright

# Abstract

This dissertation focuses on the development of magnetic resonance imaging (MRI)-guided microwave thermal therapy systems for driving experimental studies in small animals, and to experimentally validate computational models of microwave ablation, which are widely employed for device design and characterization. MRI affords noninvasive monitoring of spatial temperature profiles, thereby providing a means to to quantitatively monitor and verify delivery of prescribed thermal doses in experimental studies and clinical use, as well as a means to validate thermal profiles predicted by computational models of thermal therapy.

A contribution of this dissertation is the development and demonstration of a system for delivering mild hyperthermia to small animal targets, thereby providing a platform for driving basic research studies investigating the use of heating as part of cancer treatment strategies. An experimentally validated 3D computational model was employed to design and characterize a non-invasive directional water-cooled microwave hyperthermia applicator for MRI guided delivery of hypethermia in small animals. Following a parametric model-based design approach, a reflector aperture angle of 120°, S-shaped monopole antenna with 0.6 mm displacement, and a coolant flow rate of 150 ml/min were selected as applicator parameters that enable conformal delivery of mild hyperthermia to tumors in experimental animals. The system was integrated with real-time high-field 14.1 T MRI thermometry and feedback control to monitor and maintain target temperature elevations in the range of 4 – 5 °C (hypethermic range). 2 - 4 mm diameter targets positioned 1 – 3 mm from the applicator surface were heated to hyperthermic temperatures, with target coverage ratio ranging between 76 - 93 % and 11 – 26 % of non-targeted tissue heated.

Another contribution of this dissertation is using computational models to determine how the fibroids altered ablation profile of a microwave applicator for global endometrial ablation.

Uterine fibroids are benign pelvic tumors located within the myometrium or endometrium,and may alter the profile of microwave ablation applicators deployed within the uterus for delivering endometrial ablation. A 3D computational model was employed to investigate the effect of 1 – 3 cm diameter uterine fibroids in different locations around the uterine cavity on endometrial ablation profiles of microwave exposure with a 915 MHz microwave triangular loop antenna. The maximum change in simulated ablation depths due to the presence of fibroids was 1.1 mm. In summary, this simulation study suggests that 1 – 3 cm diameter uterine fibroids can be expected to have minimal impact on the extent of microwave endometrial ablation patterns achieved with the applicator studied in this dissertation.

Another contribution of this dissertation is the development of a method for experimental validation of 3D transient temperature profiles predicted by computational models of MWA. An experimental platform was developed integrating custom designed MR-conditional MWA applicators for use within the MR environment. This developed platform was employed to conduct 30 - 50 W, 5 - 10 min MWA experiments in ex vivo tissue. Microwave ablation computational models, mimicking the experimental setting in MRI, were implemented using the finite element method, and incorporated temperature-dependent changes in tissue physical properties. MRI-derived Arrhenius thermal damage maps were compared to Model-predicted ablation zone extents using the Dice similarity coefficient (DSC). Mean absolute error between MR temperature measurements and fiber-optic temperature probes, used to validate the accuracy of MR temperature measurements, during heating was in the range of 0.5 – 2.8 °C. The mean DSC between model-predicted ablation zones and MRI-derived Arrhenius thermal damage maps for 13 experimental set-ups was 0.95. When comparing simulated and experimentally (i.e. using MRI)

measured temperatures, the mean absolute error (MAE %) relative to maximum temperature change was in the range 5 % - 8.5 %.

# Table of Contents

# List of Figures

# List of Tables

# Acknowledgements

Foremost, I would like to express my sincere gratitude to my advisor Dr. Punit Prakash for the continuous support of my Ph.D study and research, for his patience, motivation, enthusiasm, and immense knowledge. His guidance helped me in all the time of research. I could not have imagined having a better advisor and mentor for my Ph.D study.

Besides my advisor, I would like to thank the rest of my thesis committee: Dr. Stefan Bossmann, Dr. Steve Warren and Dr. Bala Natarajan, for their encouragement and insightful comments.

I thank my fellow labmates in Biomedical Computing and Devices Laboratory: Hojjatollah Fallahi, Jan Sebek, Austin Pfannenstiel, Faraz Chamani and Ghina Zia. I really enjoyed working with them.

Last but not the least, my deep and sincere gratitude to my family for their continuous and unparalleled love, help and support. I am forever indebted to my mom for giving me the opportunities and experiences that have made me who I am.

# 1. Introduction

## 1.1. Overview and motivation

Thermal therapy is a clinically used treatment modality, which involves modulation of tissue temperature for therapeutic effect. Thermal therapy has been used clinically for immediate *in situ* cell death (thermal ablation, [1]), as a minimally-invasive alternative to surgery, treating tumors in the liver, kidney, lung, prostate and as an adjuvant therapy (hyperthermia, [2]–[4]) to sensitize tumors to chemotherapy and ionizing radiation therapy. Thermal ablation and hyperthermia have non-oncological applications as well [5]–[7].

During a thermal therapy procedure, the objective is to manipulate the target tissue temperature to a specified range, while leaving the surrounding tissue minimally affected. The treatment outcome is a function of the intensity and duration of heating within the target tissue. Therefore, quantifying the spatial pattern of energy delivered to tissue, and subsequent temperature profile, by a thermal therapy applicator is important for predicting the extent of the treatment zone. Additionally, it is beneficial to incorporate temperature monitoring capabilities within thermal therapy systems to verify that tissue temperature is driven to the desired range relative to the desired treatment goal [8]–[11].

During the development procedure of the thermal therapy systems, to evaluate the energy delivery and temperature profiles of the target, device design and biophysical properties of the target tissue may be simulated with 3D computational models. Computational models provide an approximation of the physical processes during a thermal therapy procedure, and offer the advantages of reduced cost and time, for device design and optimization, compared to purely experimental driven approaches. These models may be used to explore device design concepts, following which the designed device is fabricated and experimentally assessed in *ex vivo* and *in*

*vivo* tissue settings. If the outcome of the experiment was not as expected, models may be further applied to alter, adapt and optimize the design of the device for the specific goal. The new designed device is again fabricated and experimentally assessed. This iterative process between simulation and experiment continues to reach a desirable outcome. Researchers investigate the reliability, reproducibility and repeatability of the thermal therapy systems during the development process before transition of the system for evaluation in the clinical trial setting.

Real-time temperature monitoring is of high significance in developing thermal therapy systems to locate the heat exposure site and measure the temperature change to prevent irreversible damage. To reduce the cost, time and risk of experiment, a thermal therapeutic concept can be learned and studied using computational models that are an abstract description of the biological and physical system. To ensure the reliability and credibility of the model outputs, verification and validation of the model is required. Deep understanding of the challenges a researcher may face during implementing each of these components is imperative to ensure the healthcare needs are addressed thoroughly, which is the topic of this dissertation.

## 1.2. Research approach

Microwave thermal therapy has been used for a large number of patients and is under investigation as a heating modality for oncological and non-oncological applications [12]–[14]. The goal of this dissertation is to present new strategies to assist the development of microwave thermal therapy systems. Specifically, contributions are focused on the integration of microwave ablation and hyperthermia systems with image-guided thermometry in *ex vivo* and small-animal and computational modeling for tissue/application-specific design and characterization. As shown in Fig. 1.1, the key elements to accomplish this goal are:

**(1) Real-time temperature monitoring.** During a thermal therapy procedure, energy delivery and temperature change may deviate from the anticipated pattern due to tissue heterogeneity. Therefore, temperature monitoring is a key factor during thermal therapy to reduce the uncertainty and increase the likelihood of delivering thermal profiles within the prescribed ranges. A key challenge is to integrate a real-time temperature monitoring technique with the energy delivery platform. Magnetic Resonance Imaging (MRI) facilitates non-invasive, real-time spatial thermometry for monitoring and guiding thermal therapy procedures [15].

**(2) Verification and validation of microwave 3D computational models.** Computational models play an important role in the design and optimization of novel applicators and energy delivery strategies [16]. Modeling tools are also under development for treatment planning, to guide clinicians in the selection of optimal energy delivery parameters for individual patients, and are increasingly important as part of regulatory submissions for characterizing device performance. A key challenge with models is the development of established procedures for validating model performance. MRI enables non-invasive measurement of spatial temperature profiles. Comparing simulated and MR-derived transient temperature profiles facilitates assessing the model accuracy.

**(3) Device design and characterization.** Researchers use computational models to quantify electromagnetic radiation patterns and temperature profiles induced by microwave applicators in tissue. New microwave applicator design prototypes are often evaluated using 3D computational models and bench-top experiments. A key challenge is characterization and optimization of novel/pre-existing microwave applicator for target or application-specific use.

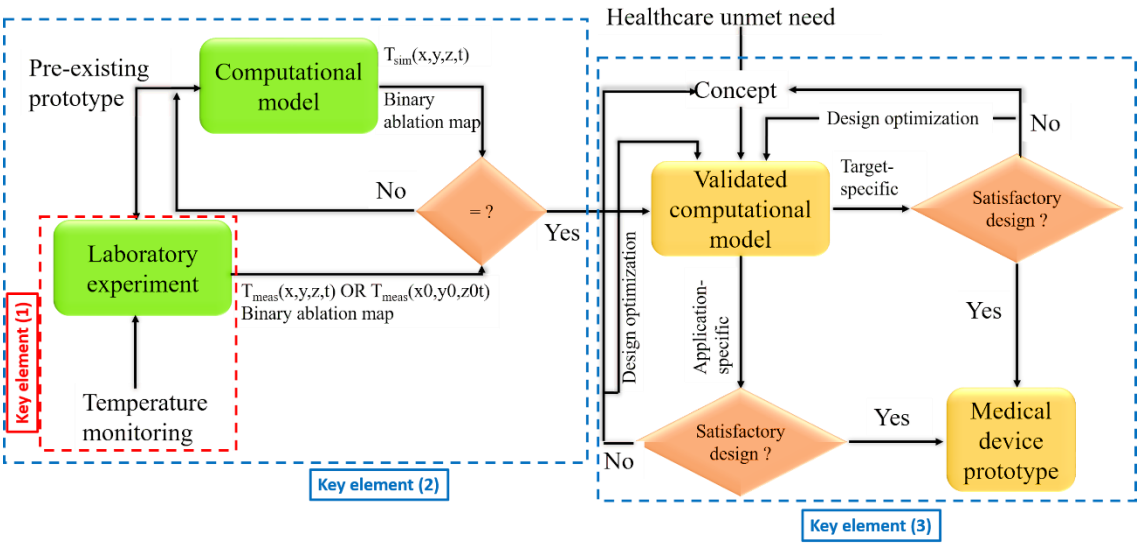


**Figure 1.1** Workflow for mathematical modeling of microwave thermal therapy for target/application-specific design and characterization

In this dissertation, the following research studies were conducted to contribute to the development of microwave thermal therapy technology, while overcoming the challenges relative to the three key elements of (1) real-time temperature monitoring, (2) verification and validation of microwave 3D computational models and (3) device design and characterization:

### 1.2.1. MR-guided localized hyperthermia delivery to small-animal

Pancreatic cancer is now one of the highest cancer-related cause of death in US [17]. For early-stage disease, surgical resection may offer a potential cure, but 80% of the patients have advanced and non-resectable pancreatic tumors at the time of diagnosis [18], [19]. For non-resectable tumors, pre-clinical studies have shown that sole chemotherapy or in conjunction with radiation therapy have impeded tumor growth [20], [21]. Studies have reported that hyperthermia sensitizes tumor cells to chemotherapy and decreases chemoresistance for pancreatic cancer cells [22], [23].

Since tumor models for small animals are widely available, small animals are frequently used for pre-clinical experimental evaluation of therapeutic strategies, including thermal

treatments [24]. To develop an accurate understanding of the effect of heat on the targeted tumor, it is important to verify the thermal doses delivered to the target tissue during hyperthermic exposure. Delivering hyperthermic thermal doses to small animals in experimental studies requires precise treatment delivery to the target while sparing surrounding tissue and controlling the core body temperature [25]. Controlling the target heating volume and conformal heating is a challenge for employing microwave energy in hyperthermia treatments.

Considering all the above, the objective of this research study is to develop small-animal MR-guided MW hyperthermia system employing a MW applicator with a localized heating pattern **(key elements 2 and 3)** and controlled energy delivery to the tumor site, relative to its real-time temperature change, to maintain tumor temperature in the hyperthermic range **(key element 1)**.

### 1.2.2. Sensitivity of ablation microwave applicator to the presence of fibroid

Menorrhagia, a condition when menstrual periods have abnormally heavy or prolonged bleeding, significantly affects quality of life, and affects ~20% of women of reproductive age [26]. Surgical interventions, e.g. hysterectomy (to remove the uterus), have been a standard treatment when medical therapy fails to mitigate the symptoms. Endometrial ablation is a procedure to destroy (ablate) a thin layer of tissue (endometrium) that lines the uterus. It is performed to stop or reduce heavy menstrual bleeding. An advantage of endometrial ablation in comparison to hysterectomy is that the procedure is that the applicator is introduced via body cavities and no incision in the body is required.

Uterine fibroids are benign lumps that grow on the uterus. Fibroids, may modify the pear shape of the uterus, which may affect the endometrial ablation pattern.

In [27], researchers have previously proposed a microwave applicator for global endometrial ablation (GEA) and investigated the feasibility of using a triangular-shaped

microwave applicator for GEA in treating uterine cavity of different sizes. The results were indicative of a suitable ablation pattern for GEA. However, since women who are candidates for endometrial ablation may also have fibroids, it is important to assess the effect of the presence of fibroids on the GEA profile.

Considering all the above, the objective of this work is to investigate the effect of presence of fibroids on the endometrial ablation profile employing validated microwave ablation computational models (**key elements 2 and 3**).

### 1.2.3. Volumetric assessment of microwave computational models validity using MR thermometry

Computational models play an important role in the design and optimization of novel applicator designs and energy delivery strategies [28]–[30]. Modeling tools are also under development for treatment planning, to guide clinicians in the selection of optimal energy delivery parameters for individual patients, and are increasingly important as part of regulatory submissions for characterizing device performance. A key challenge with models is the development of established procedures for benchmarking and validating model performance, as well as identifying sources of uncertainty.

For microwave hyperthermia and ablation procedures, the key processes that need to be modeled are microwave propagation through tissue, power absorption, and bioheat transfer [31]. At elevated temperatures, there are substantial changes in the tissue physical properties – dielectric properties [32], [33], thermal properties [34], and blood perfusion [35] – which may have a considerable impact on model predictions of treatment outcome [36]. Tissue contraction at elevated temperatures is another physical process that may be important to model for accurate prediction of ablation zone extents [37]. While temperature dependencies of tissue biophysical

parameters have been experimentally measured, experimental validation of microwave tissue heating models have been limited. Typically, model-validation is performed by comparing simulated transient temperature profiles vs. temperature measured at a few discrete points using temperature sensors such as thermocouples or fiberoptic probes [31]–[33]. In addition to the limited number of locations (often 2 – 6 sensors are employed) at which temperatures are measured, an added source of uncertainty is the position and orientation of the temperature measurement probes relative to the microwave heating device under test.

Considering all the above, the objective of this study is to develop an experimental platform providing temperature measurements at a multitude of locations to enable more comprehensive verification and validation of computational models of microwave tissue heating **(key elements 1 and 2)**.

## 1.3. Contributions

This dissertation contributes to research work carried out to address the challenges and questions of the case studies mentioned in section 1.2.

*Contribution 1:* Hyperthermia is a clinically proven sensitizer for ionizing radiation therapy, and is under investigation for thermally-mediated release of cancer therapeutic agents [38]. Due to heterogeneity in tissue biophysical properties and blood perfusion profiles, a given set of energy delivery parameters may yield highly variable thermal profiles *in vivo*. MRI affords noninvasive temperature monitoring with the Proton Resonance Frequency Shift technique, thereby providing a means to ensure adequate delivery of prescribed thermal doses [39]. Compared to existing small-animal systems for hyperthermia delivery, ultra-high field 14.1 T MRI offers the advantages of high temporal and spatial resolution for a pre-clinical platform for delivering hyperthermia to experimental small animals. MRI-derived temperature profiles during

hyperthermia, can be used to adjust applied power in order to achieve the desired thermal dose. We have designed an experimental platform for hyperthermia investigations in small animals, incorporating a microwave applicator integrated with 14.1 T ultra-high field MRI. We adapted the applicator design, to focus heating within 0.0141- 0.113 $cm^3$ tumor volume located at 1-3 mm from the skin surface, with minimal heating of the surrounding tissue. The developed platform was applied in pilot studies to assess the biophysical effects of mild heating on implanted pancreaticc tumors in small-animals. This contribution is discussed in detail in chapter 3 and in the following publications:

[40] P. Faridi, S. H. Bossmann, and P. Prakash, "Simulation-based design and characterization of a microwave applicator for MR-guided hyperthermia experimental studies in small animals," *Biomed. Phys. Eng. Express,* vol. 6, no. 1, p. 015001, Nov. 2019.

[41] S. Curto, P. Faridi, T. B. Shrestha, M. Pyle, L. Maurmann, D. Troyer, S. H. Bossmann, and P. Prakash, "An integrated platform for small-animal hyperthermia investigations under ultra-high-field MRI guidance," *Int. J. Hyperth. Off. J. Eur. Soc. Hyperthermic Oncol. North Am. Hyperth. Group,* vol. 34, no. 4, pp. 341–351, 2018.

*Contribution 2:* Uterine fibroids are benign lumps that grow on the uterus and modify the shape of the uterus, which may affect the endometrial ablation pattern. In this research, we have investigated the effect of presence of fibroids on the endometrial ablation profile. First, we have experimentally validated 3D computational model of global endometrial microwave applicator in *ex vivo* liver tissue. Next, the validated computational models were employed incorporating fibroids in variant sizes and locations mimicking real conditions of women uterus. This study served as a pre-clinical approach to investigate the effect of fibroids on the ablation profile of the GEA loop MW antenna to increase safety and identify, assess and measure risks of using this

specific antenna before translating to clinical trials. Details of this study is discussed in chapter 4 and in the following publications:

[42] P. Faridi, H. Fallahi, and P. Prakash, "Evaluation of the Effect of Uterine Fibroids on Microwave Endometrial Ablation Profiles," in *40th Annual International Conference of the IEEE Engineering in Medicine and Biology Society (EMBC)*, Jul. 2018, pp. 3236–3239.

*Contribution 3*: Microwave ablation is increasingly being used for image-guided ablation of tumors in the liver, lung, and other sites. Computational models that predict ablation outcome for specified applied energy levels are invaluable for guiding the design of ablation devices; comparative assessment of treatment delivery strategies; device characterization for regulatory submissions; and are under development for patient-specific treatment planning. Current approaches for validation of microwave ablation models have been limited to comparing simulated and experimental measurements of ablation zones at a few discrete points, as well as comparing experimentally observed ablation profiles with simulations. Here, we have developed a microwave ablation platform integrated with 3T MRI, providing a means for comparative assessment of model-predicted and measured 3D temperature and ablation profiles. This study reports paves the way for further investigation of models for application in pre-treatment planning of MWA ablation procedures. Details of this study is discussed in chapter 5 and in the following publications:

[43] Faridi, P. and Prakash, P., (2018). Experimental validation of computational models of microwave tissue heating with magnetic resonance thermometry, IEEE International Microwave Symposium (IMS), Philadelphia, PA.

[44] P. Faridi, P. Keselman, H. Fallahi, and P. Prakash, "Experimental assessment of microwave ablation computational modeling with MR thermometry," *Med. Phys.*, 2020.

## 1.4. Dissertation outline

This dissertation is organized as follows. The second chapter is dedicated to a brief introduction of image-guided thermal therapies for cancer treatments. Chapters 3, 4 and 5 report on the research topics introduced in sections 1.2.1 – 1.2.3. The final chapter presents concluding remarks and suggestions for future research directions.

# 2. Background[1]

## 2.1. Introduction

Extensive investigations of the biological effects of therapeutic heating has led to clinical translation of technologies for treatment of cancer. Several clinical trials have demonstrated the benefits of mild hyperthermia, moderate heating in the range of $39 < T < 45$ °C for 20-60 mins, as an adjuvant to ionizing radiation and chemotherapy of select cancers [46]–[48]. Thermal ablation, heating to temperatures in excess of 50 °C, is increasingly being used for treatment of surgically unresectable tumors in the liver, kidney, lung, and other organs [49].

Fig. 2.1 illustrates the components of a generic image-guided thermal therapy system. Minimally/non-invasive applicators deliver therapeutic energy from an external source to the targeted tissue. Real-time imaging facilitates accurate positioning of the applicators relative to the targeted tumors, to maximize the likelihood of delivering safe and effective treatments. Imaging data may also serve as input to simulation-based predictive models that assist physicians in selecting energy delivery parameters tailored for individual patient anatomies. Techniques for measuring spatial temperature profiles in the targeted tissue provide a means for real-time monitoring of treatment progress, which is particularly important because unknown blood perfusion profiles serve as a heat sink, and may yield highly variable thermal dose profiles for a fixed set of energy delivery parameters. These can be coupled with feedback-control techniques to afford conformal delivery of prescribed thermal doses on a patient-specific basis. This report will detail the technical foundations of each of the components summarized in Fig. 2.1.

[1] This chapter was reproduced/adapted from Ref. [45] with permission from The Royal Society of Chemistry.

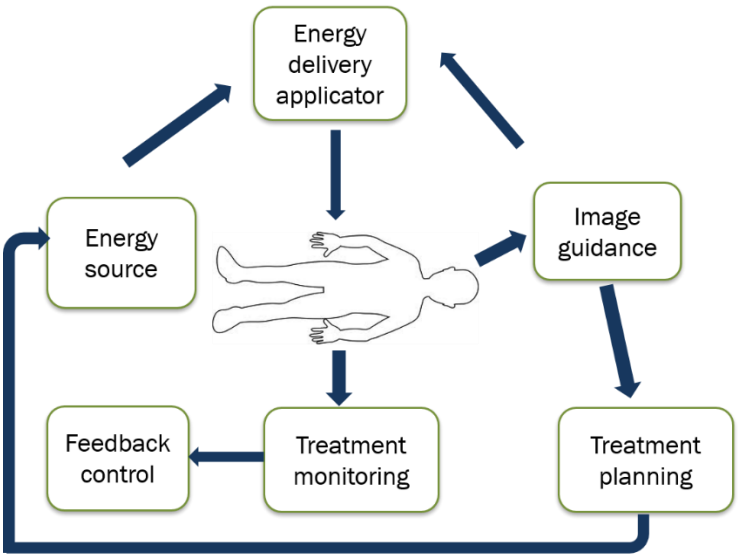


**Figure 2.1** Overview of thermal therapy systems

## 2.2. Biological Rationale for Thermal Therapy

### 2.2.1. Review of Physiological Effects of Heating and Thermal Dosimetry

Fig. 2.2 summarizes the physiological effects of heating over the temperature range 37 – 100 °C. Mild heating at temperatures in the range of 37-43 °C yields increases in local blood flow. The response of vasculature to heating differs in healthy and tumor tissues, yielding biophysical effects that can be targeted for therapeutic applications. Normal tissues have more structured vasculature compared to tumors, resulting in greater convective heat loss during heating. Furthermore, vessels in healthy tissue dilate in response to heating, thereby increasing blood flow rate which in turn leads to greater heat dissipation, temperature alleviation, and lower damage to normal tissues comparing tumors [50]. Consequently, exposure to a fixed amount of therapeutic energy may yield increased heating in tumors relative to healthy tissue. Thermosensitivity of tumors is also influenced by hypoxic cancer cells and the acidic tumor microenvironment. Low pH reduces blood flow rate which in turn leads to lower amount of oxygen delivery to the tumor

cells. At higher temperatures, in excess of 45 °C , blood flow rate decreases causing thrombosis, heat trapping and tissue necrosis [51].

Thermotolerance, impediment to thermal cytotoxicity, is regulated by the release of Heat Shock Protein (HSP). HSPs are chaperone proteins which are upregulated during heat stress, and transport misfolded proteins to the cell membrane. [52]. However, this phenomenon occurs only up to approximately 43-43.5 °C [53].

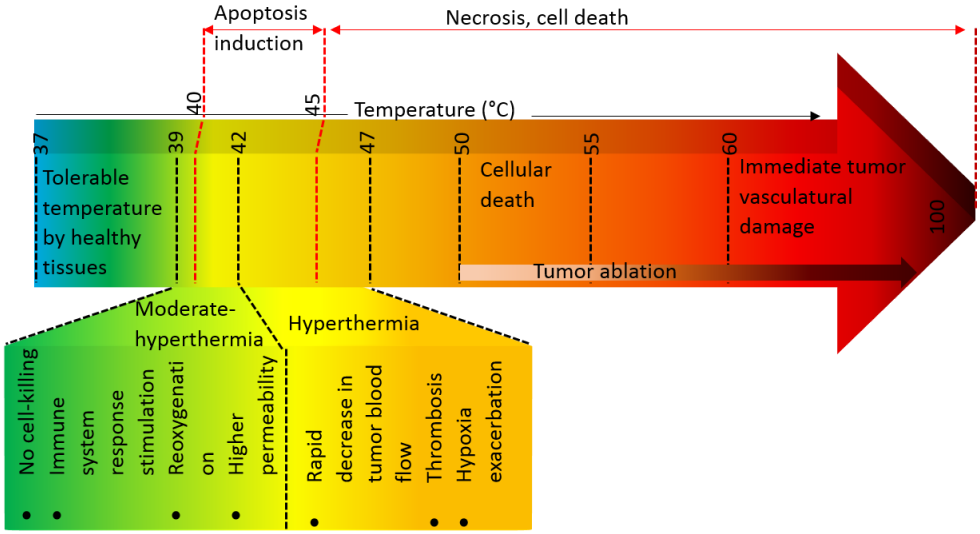


**Figure 2.2** Physiological changes induced by heating

Thermal damage induced by heating is a function of the time-temperature history during heating. Fig. 2.3 illustrates an Arrhenius plot for Chinese Hamster Ovary (CHO) cells exposed to isothermal heating at various temperatures. In Figure 2.3, $D_0$ defines the time at a particular temperature for cells to reach the 63% survival rate. Cellular deactivation due to heating can be calculated using Equation (1):

$$B = Ae^{(-E/RT)} \tag{1}$$

where B is the rate constant ($B = 1/D_0$), E is the activation energy [kcal/mole], $R$ is the universal gas constant, A is the frequency factor, and T is temperature in K. A clear breakpoint in rate of deactivation is observed at ~43 °C.

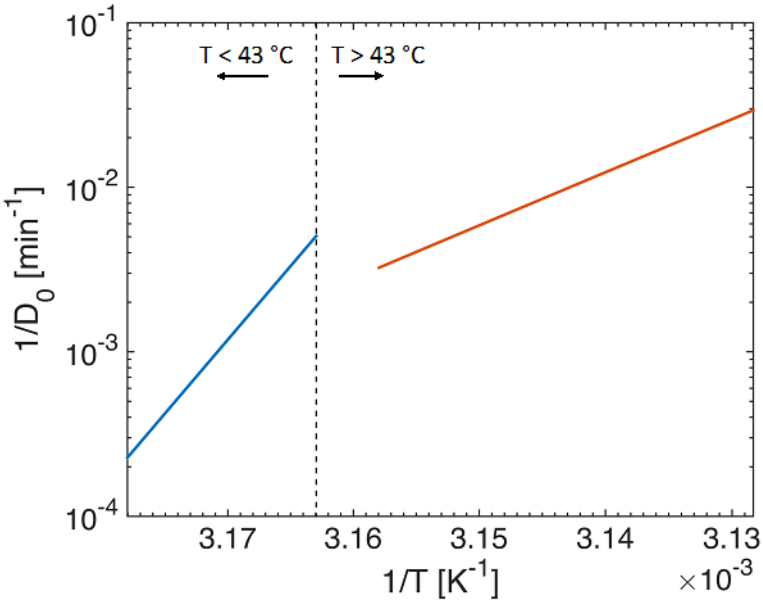


**Figure 2.3** Arrhenius plot for CHO cells (Arrhenius coefficients for generating this plot are taken from Reference **[54]**)

Sapareto and Dewey developed a thermal isoeffective dose model for comparing non-isothermal exposures to an equivalent isothermal exposure at a reference temperature. 43 °C is typically taken as the reference temperature due to the breakpoint in deactivation at this temperature. The Sapareto-Dewey thermal dose model is given by Equation (2):

$$CEM\,43 = \int_0^t R^{(T_{break} - T(\tau))}\, d\tau \qquad (2)$$

where CEM43 is the cumulative equivalent minutes at 43 °C, *R* represents the rate of damage below and above break point, and T stands for the measured temperature during heat exposure. For most cells, at temperatures below 43 °C, R = 0.25; at temperatures greater than 43 °C, R = 0.5. This thermal dose model has found widespread applications in research and clinical studies for comparative assessment of the effects of therapeutic hyperthermia exposures [55].

### 2.2.2. Moderate heating/ Hyperthermia

Moderate heating in the range of 40-45 °C for 20 to 90 minutes has the following effects:

#### 2.2.2.1 Mild cytotoxicity.

Heating in the range of 40- 45 °C for 20-90 min has a cytotoxic effect on tumor cells. While early clinical applications of hyperthermia aimed to achieve cell kill via heating, this proved to be ineffective due to the technical challenges of maintain tumor temperatures within the desired change in the absence of real-time volumetric thermometry.

#### 2.2.2.2 Increased Efficacy of Chemotherapy and/or Ionizing Radiation.

In addition to cytotoxic effects, heating at temperatures in the range of 40-45 °C synergizes with chemotherapy and ionizing radiation therapy. Large tumors have reduced blood flow compared to healthy tissues due to the disordered vasculature structure. Consequently, the effect of chemotherapy in large tumors is hampered, because the poor blood flow limits the amount of drug delivered to the tumor. During hyperthermia, physiological changes such as higher blood flow rates and higher vascular permeability due to increased vessel pore size, result in enhanced delivery of chemotherapeutic drugs [56]. Furthermore, increased blood flow also alleviates hypoxia in large tumors, which increases the efficacy of ionizing radiation therapy. Radiation therapy takes advantage of reoxygenation of the hypoxic tumor environment because molecular Oxygen ($O_2$) possesses a high potential for radio-sensitization [57]–[61]. Mild temperature hyperthermia also influences a part of cell cycle which is resistant to radiation (i.e, the S- phase) [62].

#### 2.2.2.3 Stimulation of the immune response.

Tumor cells possess antigens that are recognizable by the immune system [63]. Hyperthermia navigates a high range of these unique antigens to the tumor surface, thus enhancing the performance of the immune system response to tumors [64]. Moreover, hyperthermia initiates a negative feedback response with the induction of HSPs on the tumor site during heat exposure,

which magnifies the immune response [65]. HSPs activate Dendritic Cells (DCs) which are antigen-restricted, do not recognize normal cells, thereby inhibiting collateral damage to normal cells [63]. Additionally, hyperthermia modifies blood flow in tumor sites which in turn facilitates a higher rate of immune cells transmission to the tumor. The specific time temperature ranges within immune stimulation is observed remains the subject of active research [66].

### 2.2.3. Tumor Ablation

Thermal tumor ablation refers to the destruction of tumors by exposing tumor tissue to T > 50 °C for 10-15 minutes. Cell death at temperatures in excess of ~60 °C occurs within a few seconds. Several energy modalities have been applied for thermal ablation, including: radiofrequency current, microwaves, lasers, and ultrasound. Cryoablation refers to tissue freezing which has been clinically applied for tumor ablation. Non-thermal techniques for thermal ablation, such as irreversible electroporation have also been developed.

During an ablation procedure, a minimally invasive applicator (typically, less than 2.5 mm in diameter) is inserted into the target tumor under image guidance. Energy delivered by the device is absorbed by surrounding tissue leading to heating. In proximity to the ablation device, the majority of heating is due to direct power absorption from the energy source. Due to steep thermal gradients, heat spreads radially outward from the ablation applicator, leading to enhancement of the ablation zone by passive thermal conduction.

As illustrated in Fig. 2.4, the ablation zone can be divided into three sub-sections around the applicator, each displaying a variety of physiological changes based on the extent of tissue heating. In the central zone, tissue in closest contact with the ablation device, necrosis is the dominant feature. Tissue in the central zone is in excess of 50 °C, and peak temperatures could be greater than 100 °C depending on the energy modality used. In the transition zone, tissue

temperature is in the range of 42-47 °C; in this region, passive heat transfer due to thermal conduction is the major source of heating. Apoptosis and some forms of sublethal thermal damage are observed in the transition zone. Beyond the transition zone, the tissue temperature in the mild hyperthermia zone ranges from 39-42 °C [49], [67].

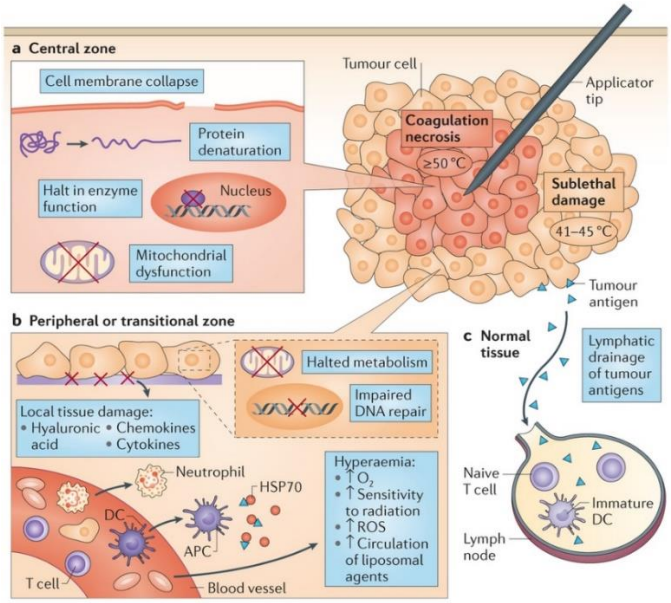


**Figure 2.4** Sub sections of ablation zone, A) central zone, B) transitional zone, C) mild hyperthermia zone **[68]**

### 2.2.4. Thermally-triggered Release of Therapeutic Agents

There are significant barriers obstructing drug delivery to cancer cells which limits the specificity of chemotherapy [69]. To alleviate this problem, therapeutic agents may be transported and delivered through carriers such as polymers, liposomes and particles. Using drug delivery systems employing carriers in conjunction with heat exposure, has led to improvement in increasing the quantity of drug delivered to tumor.

Polymers, macromolecular carriers, are biocompatible materials used for delivering chemotherapeutic agents to the target. Responsive-polymers are a specific type of polymer that respond to external stimuli (physical or chemical). One class of polymers, referred to as thermosensitive polymers, undergo a phase transition at a critical temperature. Using heat as a

trigger for responsive polymers permits the use of hyperthermia for localized drug release [70]. Temperature sensitive responsive polymers are subjected to phase transition based on distinctively selected temperature threshold according to the drug delivery system. Hydrophilic structure of responsive polymer is activated below its lower critical solution temperature (LCST) where it remains in acqueous solution; however, above LCST it collapses and releases therapeutic agents. A typical critical temperature in the range of 39-40 °C as this value is above normothermic temperature, and at the same time, lower than hyperthermic temperatures where vascular stasis occurs, thereby limiting drug release within the heated target [71].

Liposomes for drug delivery are vesicles containing a bilayer lipid surrounding aqueous solution which establishes the context of injecting and transporting hydrophilic and hydrophobic therapeutic drugs at the same time. Temperature sensitive liposomes (TSLs) exploit the contribution of hyperthermia in conjunction with liposomal drug delivery to transport, aggregate and preserve chemotherapeutic agents. TSLs are triggered above a temperature threshold, which is associated with temperature change during hyperthermia procedure, to decrease the possibility of drug extravasation into healthy cells. Fig. 2.5 illustrates the temperature dependent structure of TSLs [72].

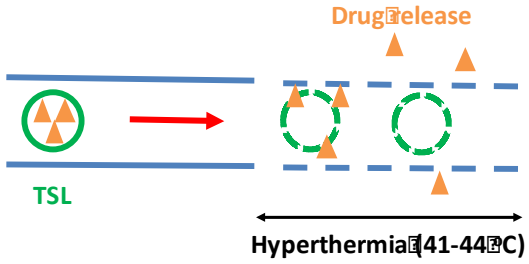


**Figure 2.5** Liposomal drug release during hyperthermia (HT) in tumors.At temperatures in the range of 41-44 °C, drug is released from temperature sensitive liposomes (TSL) within the vasculature. Extravasation is enhanced by increased vessel permeability due to heating.

### 2.2.5. Methods of Tissue Heating

#### 2.2.5.1 Microwave Tissue Heating

Microwaves, electromagnetic waves with frequency ranging between 30 MHz – 300 GHz have been widely used for thermal therapy (both hyperthermia and thermal ablation). Polar molecules in tissue, such as water and protein, attempt to align with the polarity of the electric field, leading to heating by dielectric hysteresis (see Fig. 2.6) [73].

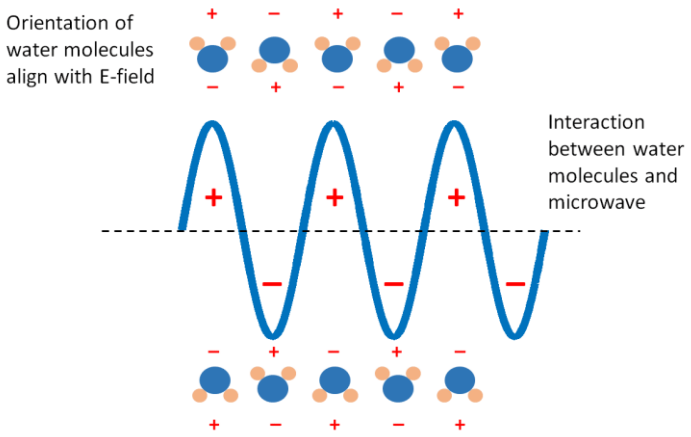


**Figure 2.6** Schematic illustration of the interaction between water molecules and microwaves. (adapted from [28])

Microwave propagation and absorption within tissue is governed by the complex dielectric properties of tissue $\varepsilon(\omega) = \varepsilon'(\omega) - \varepsilon''(j\omega)$, where $\omega$ is angular frequency. The real part, $\varepsilon'(\omega)$, is a measure of a material's ability to store the electric field, while the imaginary part, $\varepsilon''(j\omega)$, is a measure of loss. The effective electrical conductivity is given by $\sigma_{eff} = \sigma_s + \omega\varepsilon''$. Frequency dependent dielectric properties for a range of tissue types have been measured by several groups and reviewed in [74], [75]. From these fundamental properties, the absorption coefficient alpha can be computed using:

$$\alpha = \omega\sqrt{\mu\varepsilon}\left\{\frac{1}{2}\left[\sqrt{1+\left(\frac{\sigma}{\omega\varepsilon}\right)^2}-1\right]\right\}^{1/2} \quad (3)$$

The penetration depth, *d* [m], is defined as the reciprocal of the attenuation coefficient and is a measure of the distance within a material which a wave propagates before it is attenuated to 1/*e* (i.e. 36.8%) of its original intensity.

$$d = \frac{1}{\alpha} = \frac{1}{\omega\sqrt{\mu\varepsilon}\left\{\frac{1}{2}\left[\sqrt{1+\left(\frac{\sigma}{\omega\varepsilon}\right)^2}-1\right]\right\}^{1/2}} \quad (4)$$

Electromagnetic penetration depth, *d*, decreases with increasing frequency. Thus, lower frequencies are better suited for non-invasive energy delivery to deep-seated tissues. However, smaller wavelengths at higher frequencies facilitate the use of smaller antennas and ability to focus power deposition patterns to smaller regions. The choice of operating frequency for specific applications trades off these two considerations.

***Microwave hyperthermia systems***

Microwave thermal therapy systems consist of a high power signal source, power delivery cables, and microwave antennas that radiate energy to the target tissue. For hyperthermia, non-invasive applicators operating at 100-400 MHz have been developed for regional heating of pelvic [76], limb [77], and head-and-neck targets. At these frequencies, wavelengths are relatively long, leading to large focal spots, with limited precision of heating [78]. A challenge with non-invasive delivery is the unintended heating ("hot spots") due to dielectric differences at tissue interfaces.

Several microwave applicator designs have been presented in the literature and are in clinical use for hyperthermia and tumor ablation [78]. Microwave hyperthermia applicators are under development for pre-clinical small animal investigations [79]–[83]. A simulation based water loaded microwave applicator with operation frequency of 2.45 GHz was designed, optimized and implemented in [83] for murine bladder hyperthermia in combination with chemotherapy. The microwave applicator is adjustable for volume and depth of heating. *In vivo* studies shown that it

can heat small tumors to the hyperthermic range with 2-3 mm depth from the body skin. In this study, temperature was monitored subcutaneously, in vagina and rectum with 3 fiber optic probes connected to a motor that pulled them out every 1 mm for 15 levels and push them inside again for 15mm to reach the initial place. Given the real time temperature measurements, manual feedback control was applied to change the input power to keep the temperature constant in the hyperthermic range. Bladder temperature was assumed 1-2 °C higher than vagina temperature according to their in vitro validated numerical model.

Systems and devices for microwave ablation have evolved from those originally developed for hyperthermia, as recently reviewed by Ryan *et al*. [84].

***Microwave ablation systems***

Microwave ablation devices are thin cylindrical antennas, attached to a microwave generator to produce adequate amount of power at a certain frequency; 915 and 2450 MHz are most widely used in clinical systems, though higher frequency systems are under investigation [85], [86]. Early devices consisted of coaxial-based antennas. Recent developments include modified microwave devices to overcome the challenges with unintended heating along the applicator feedline. For instance, sleeves/chokes antennas are designed to control the heating along the antenna shaft [87]–[90]. Active cooling along the antenna shaft limits unintended heating to adjacent tissue due to losses within coaxial cables [7]–[9].

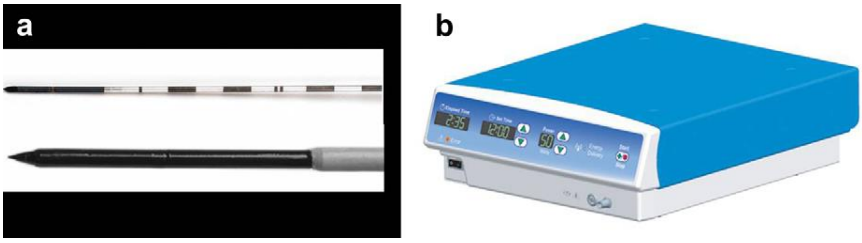


**Figure 2.7** Example clinical microwave ablation system, Evident TM Microwave ablation system/Covidien Ltd, (a) antenna, (b) microwave generator. (Images reproduced with permission from reference **[93]**)

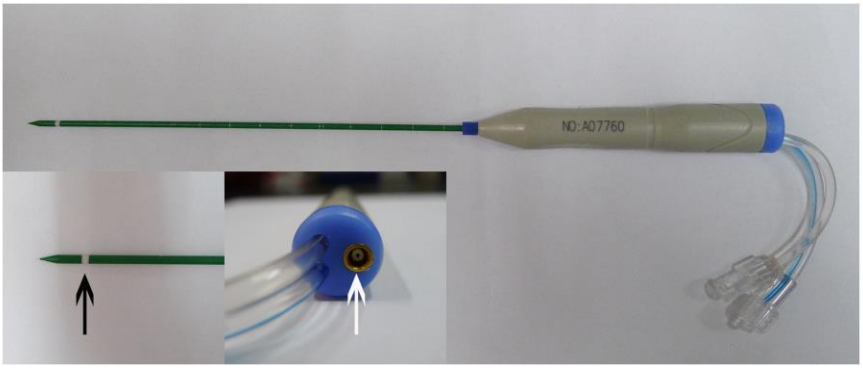


**Figure 2.8** Example of a 2.45 GHz cooled-shaft microwave ablation device from Nanjing Yigao Microwave Electric Institute, Nanjing, China. The black arrow displays the radiation section of the applicator. The microwave generator is connected to applicator via the connector indicated with the white arrow. (Image reproduced with permission from Zhou W et al., (2013) Comparison of ablation zones among different tissue using 2450-MHz cooled-shaft microwave antenna: results in ex vivo porcine models. PLOS One 8(8): e71873. doi: 10.1371/journal.pone.0071873 [94])

### 2.2.5.2 Radiofrequency Current

RF energy for tissue heating is delivered via electrodes inserted to the tissue, whether percutaneously or during open surgery. RF ablation typically employs currents operating at 460-500 kHz [95], [96]. The mechanism of heating during RF ablation is due to the agitation, oscillation and collision of ions within tissue. The peripheral ablation area is created due to thermal conduction in the surrounding tissue which is as small as few millimeters [73].

Limitations of RF ablation include: relatively small region of active heating within ablation zones, necessity of ancillary components such as grounding pads, and tissue electrical impedance limitation due to water vaporization when temperature increases up to 100 °C that impedes further electricity deposition. The latter effect is highly enunciated if charring has occurred and insulated the electrodes [97].

RF applicators can be used for either bloodless superficial incision such as skin tumors, lesions in bladder or gastrointestinal which are accessible via body cavities [98] or deep-seated tumors [99]. Examples of RF applicators in clinical use are displayed in Fig. 2.9.

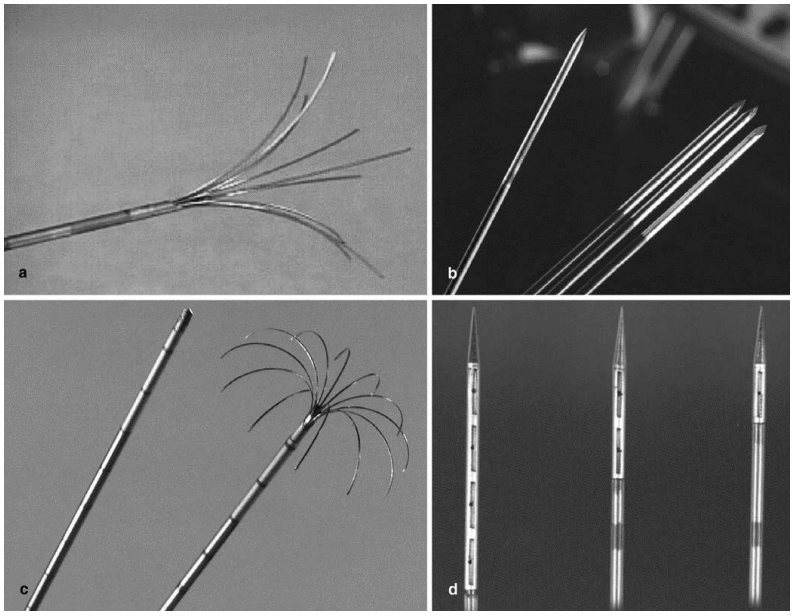


**Figure 2.9** Various commercially available RF devices, (a) RITA 14G Starburst XL needle, (b) Cooled-tip Radionics needle, (c) LeVeen pronged needle and (d) The Berchtold needle with holes at the end of the needle (Image reproduced with permission of Springer from European Radiology, Radio-frequency tissue ablation of the liver: in vivo and ex vivo experiments with four different systems, vol. 13, 2003, 2346-52, A. L. Denys et al. **[100]**)

### 2.2.5.3 Lasers

Laser-tissue interaction is based on the physical mechanism of photon penetration, absorption, and scattering in tissue. Absorption occurs via electron excitation and transmission to a higher state. Chromophores are the light absorbing component of the tissue that converts the laser beam to thermal energy by absorbing the water within the lasers path. Penetration depth reduces rapidly with increased water content [101]. Absorption coefficient, $\mu_{a,}$ is defined the same as scattering coefficient. The penetration depth of laser within tissue is given by 1/ $\mu_a$. The total energy attenuation coefficient $\mu_t$, is defined in Equation (5):

$$\mu_t = \mu_s + \mu_a \quad (5)$$

The higher absorptive capacity of the tissue compared to scattering ability results in keeping the energy in line with laser beam diameter. Greater scattering capacity diffuses the energy outside the beam light diameter [102].Taking into account all the above laser principles and optical

characteristics, $\mu_s$, $\mu_a$ and $g$, several reactions occur relevant to medical applications: chemical, thermal reactions, tissue ablation and photodisruption [103].

In addition to interstitial tumor ablation, laser thermal therapy has applications in dermatology and ophthalmology [104]. Laser is either transmitted to the target through optical fiber noninvasively or inserted invasively to the target and produce thermal ablation through its inserted tip into the tissue. One of the applications of interstitial laser ablation is focal heating and image guided drug delivery (IGDD) as shown in Fig. 2.10. Laser systems have been integrated with MRI thermometry for providing real-time assessment of target heating, and to avoid lethal damage to healthy tissue while affording drug delivered to the target and temperature profile during the experiment.

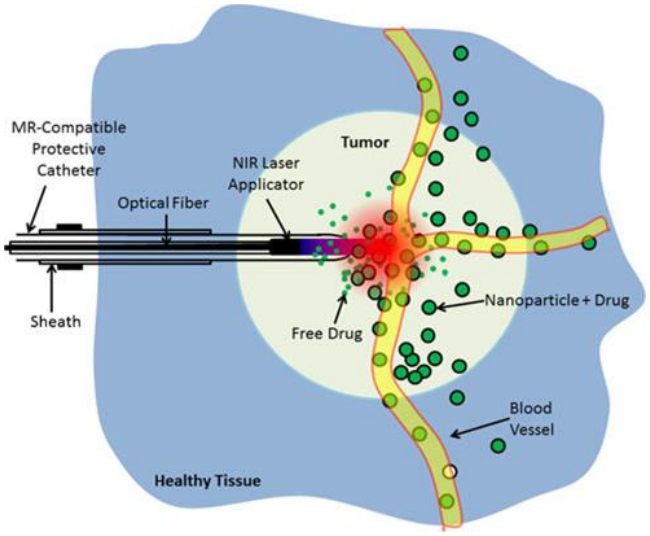


**Figure 2.10** MR compatible laser applicator used for thermal ablation and drug delivery. Nanoparticles carrying drugs are exploded during treatment releasing drugs within the tumor (Image reproduced with permission of Springer from Pharmaceutical Research, MRI-guided monitoring of thermal dose and targeted drug delivery for cancer therapy, vol. 30, 2013, 2709-17, R. Fernando et al. **[105]**)

Fig. 2.11 shows an example laser device, in clinical use for thermal ablation, incorporating a cooling catheter to restrict peak tissue temperatures within surrounding tissue and reduce the risk of applicator damage.

The size of ablation zones achievable with lasers is limited (~1-2 cm) because of the rapid absorption and scattering features of tissue small ablation zones. These ablation zone sizes are relatively small compared to the other energy modalities described previously [104].

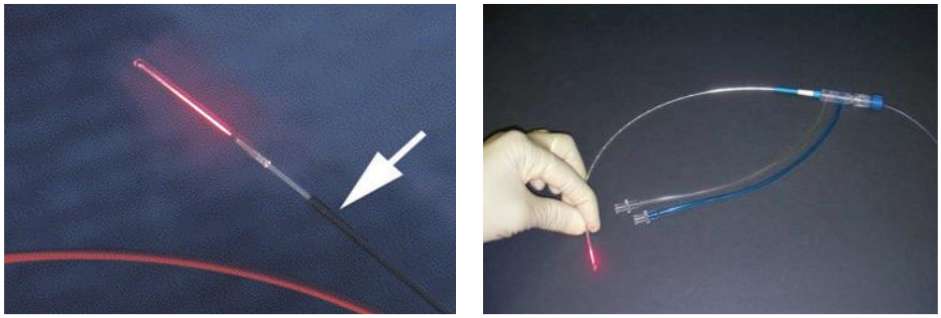

**Figure 2.11** Laser induced thermal therapy (LITT) device, (a) An illuminated fiber tip and shaft covered with magnetite particles for visibility during MR Imaging, (b) Visualase laser device with cooling shaft. (Image reproduced from **[106]**)

### 2.2.5.4 Ultrasound

Ultrasound (US) is a mechanical pressure wave, with frequency in the range 20 kHz – 10 MHz, causing 3D molecular oscillation around their mean position in the direction of wave propagation. Ultrasound propagates through the tissue which attenuates exponentially as energy moves away from the source. The energy amplitude, acoustic intensity, is the time average of energy flow through a unit area. In general, US waves are transmitted from a transducer, made from piezoelectric crystals which vibrate in response to the applied input voltage thereby generating high frequency sound pressure waves, focused in a desirable spot with diameter less than applicator diameter at a distance of 5-20 times larger than the applicator diameter (Fig. 2. 12) [107].

US can be used for either hyperthermia with long time heat exposures and low temperature rise to sensitize tissue to radiotherapy/ chemotherapy as discussed in section 1, or ablation with low time duration of experiment and great temperature rise. When temperature increases to 100 °C, tissue water evaporates and changes its state to gas. US energy interaction with gas bubbles

inside the tissue significantly differs from liquid water molecules, due to different density and sound speed, and, therefore, temperature distribution is modified based on higher rate of reflection and scattered beams in the gas bubbles. High pressure ultrasound produces microbubbles, in a process called acoustic cavitation. Inertial cavitation is a phenomenon caused by microbubbles explosion due to high amplitude pressure and consecutively expansion and contraction of microbubbles, which results in mechanical tissue destruction [107].

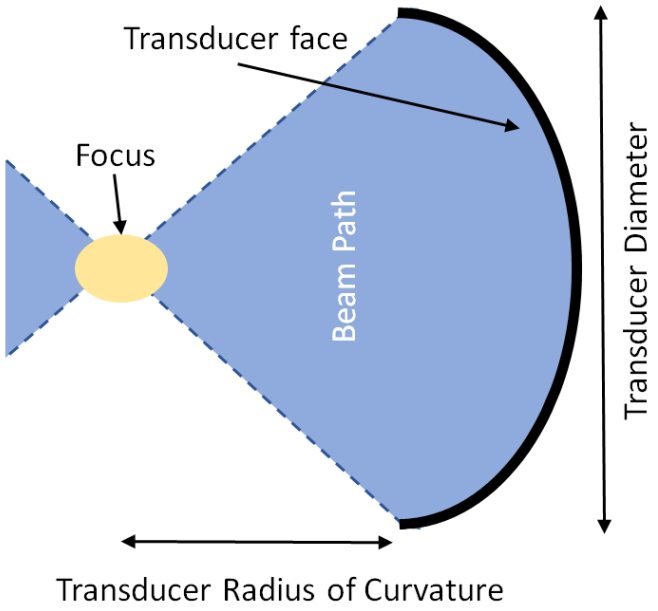


**Figure 2.12** (a) Illustration of beam path and focal spot from a curved ultrasound transducer (illustration adapted from [107]).

High intensity focused ultrasound (HIFU) ablates the tumor based on two strategies; (a) thermal effect and (b) mechanical effect. Thermal effect of US allows the tissue to absorb the energy, convert to heat leading to coagulative necrosis while mechanical effect is manufactured with mechanical force and displacement of US transducer such that it creates an acoustic cavitation [108]. High frequency mechanical acoustic waves delivered to the localized target causes tissue dilution leading to periodic elevation and alleviation of tissue pressure. As a consequence of

alternative changes in tissue pressure, gas bubbles are created inside tissue which can interact with US waves to eradicate tumor cells via necrosis. A clinical HIFU system is shown in Fig. 2. 13.

**Figure 2.13** JC HIFU system used for monitoring and therapeutic systems (HAIFU Technology Company, Chongqing, PR China) (Image reproduced with permission from reference **[109]**).

Single element HIFU systems may not be capable of heating the large regions of interest and requires mechanical steering of the beam to treat the entire target region. This displacement may cause heterogeneous temperature distribution and is a time consuming procedure [105]. To overcome these challenges, phased array transducers are employed allowing electronically steering of the ultrasound beam, by applying a time delay or change in phase angle to the signal exciting each transducer, such that an optimized amount of energy is projected to the desired spot. Phased array transducers enabling heating of the target with varying beam shapes and sizes, adjustable focal point size and position to avoid discontinuities between the focused points of all the transducers. Phased array transducers may perform with phase difference to focus on a single focal spot, or may possess multiple focal points to heat up a larger area at the same time to reduce the treatment time [107], [110]–[113]. As such, phased array transducers provide strong flexibility for adjusting focal spot size, shape, and location, to minimize unintended heating of non-targeted tissues [114].

Although thermal HIFU has been investigated for more than a decade, mechanical HIFU is still under development [10] and the corresponding physiological changes occurring during HIFU ablation are still not well understood [115], [116]. HIFU integration with monitoring techniques such as magnetic resonance imaging (MRI) is recognized as a platform for hyperthermia experiments due to its capability of maintaining temperature constant [117].

### 2.2.6. Image Guidance and Monitoring for Thermal Therapies

#### 2.2.6.1 Significance of Image Guidance

Thermal therapy regimes target tumor sites with negligible damage to healthy tissue. During a thermal therapy procedure, biological and physiological changes in the tissue, accurate heat localizing and the amount of thermal dose delivered to the tissue are not well determined due to heterogeneity in tissue physical properties. One of the most significant changes is the blood perfusion which functions differently based on tissue architecture. In order to verify the amount of thermal dose delivery to the treated target and to evaluate the performance of the procedure, real time monitoring and image guidance is of high importance. Image guidance improves the accuracy of thermometry, provides a thermal map to validate the precise thermal tissue targeting and offers the therapeutic system the ability to control the amount of heat delivery to the tumor site while sparing the surrounding tissue.

#### 2.2.6.2 Techniques for Monitoring Treatment Progression

Noninvasive thermal dose monitoring techniques are utilized with integration to heating modalities to acquire thermal map, for real time monitoring and treatment guidance. These imaging techniques exclude the invasive insertion of thermocouples, thermistors and fiber optic temperature probes.

***MR Thermometry***

Magnetic Resonance Imaging (MRI) is one of the most prevalent, reliable and comprehensive thermal monitoring methods to measure temperature profiles inside the tissue along with illustrating anatomical information. MR images consists of two sets of data; *Magnitude Imaging* monitors anatomic information such that different organs, tumor site and the location and direction of thermal applicator. *Phase Imaging* provides a relative measurement of temperature change with the proton resonance frequency shift (PRFS) method [83], [84].

Using PRFS method, temperature change can be measured by way of phase changes occurring during imaging due to PRFS temperature dependent parameters. Frequency of water protons are sensitive to temperature change and can be expressed as [118], [119]:

$$f_{water} = \gamma(1 + \sigma_T + \sigma_0)B_0 \quad (5)$$

where $B_0$ is the MR static magnetic field, $\gamma$ is the gyromagnetic ratio and $\sigma_T$ and $\sigma_0$ are local magnetic susceptibilities caused by temperature and non-temperature components. In water-rich organs (not lipids), $\sigma_0$ is negligible and the changes in the proton frequency are due to temperature changes in tissue caused by thermal treatment [120]. The frequency changes can be written as:

$$\sigma_T = \alpha.\Delta T \quad (6)$$

$$\Delta f = \gamma\alpha\Delta T B_0 \quad (7)$$

where $\alpha$ is temperature dependent coefficient (°C/ppm). For a given echo time (TE) defined in the imaging sequences, phase difference is converted to temperature changes as described in Equation (8):

$$\Delta\phi = \Delta f.TE = \gamma\alpha\Delta T B_0 TE \quad or, \Delta T = \frac{\phi_T - \phi_0}{\gamma\alpha B_0 TE} \quad (8)$$

where each phase image during heating experiment, φ(T), is subtracted from the initial phase image which contains a specified temperature information, $\varphi(T_0)$ so that the phase change becomes proportional to temperature change.

Fig. 2.14 demonstrate MRI images of a phantom and live mouse derived from a 14 T vertical scanner (Bruker Ascend III, 30 mm diameter micro-imaging probe).

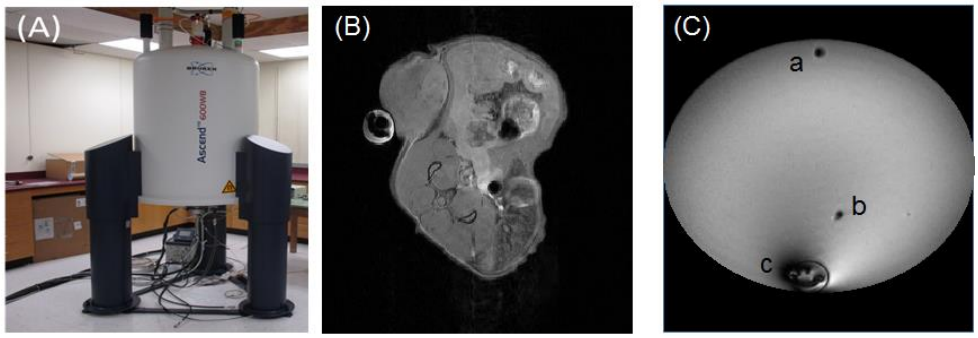


**Figure 2.14** (A) Photograph of a vertical MRI scanner, (B) in vivo anatomical image of mouse, (C) tissue-mimicking phantom, a and b are fiber optic temperature probes inserted inside the phantom to validate the temperature measurement with PRFS method and c shows the heating applicator

MRI guided thermal therapy provides a noninvasive temperature monitoring method which can be integrated with different heating modalities to improve the accuracy of treatment. As shown in figure above, MR can locate tumor site, heating applicator position and direction along with monitoring spatio-temporal temperature map to limit healthy tissue damage. Figure 2.15 shows MR temperature map during breast cancer ablation using MR guided focused ultrasound (MRgFUS). MR thermometry is also investigated for guiding liver RF ablation illustrated in Fig. 2. 16.

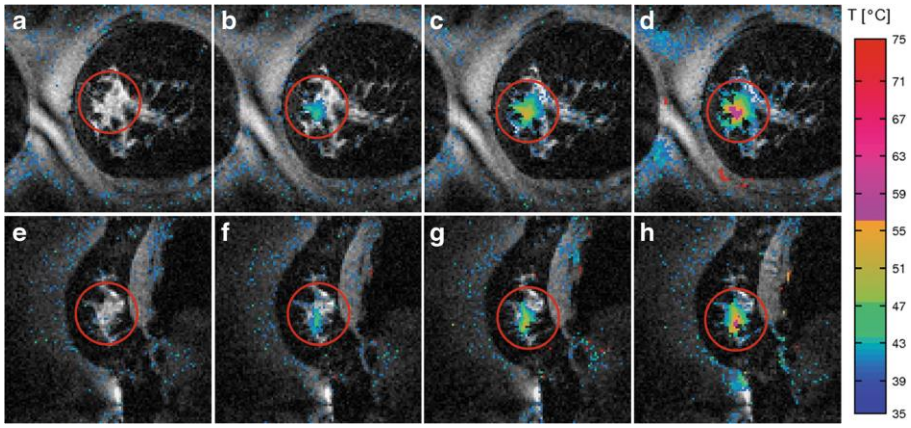


**Figure 2.15** Temperature superimposition on MR magnitude images of breast cancer using HIFU with temporal resolution of 2.5 s, (a)-(d) display the coronal and (e)-(h) display the sagittal images **[121]**)

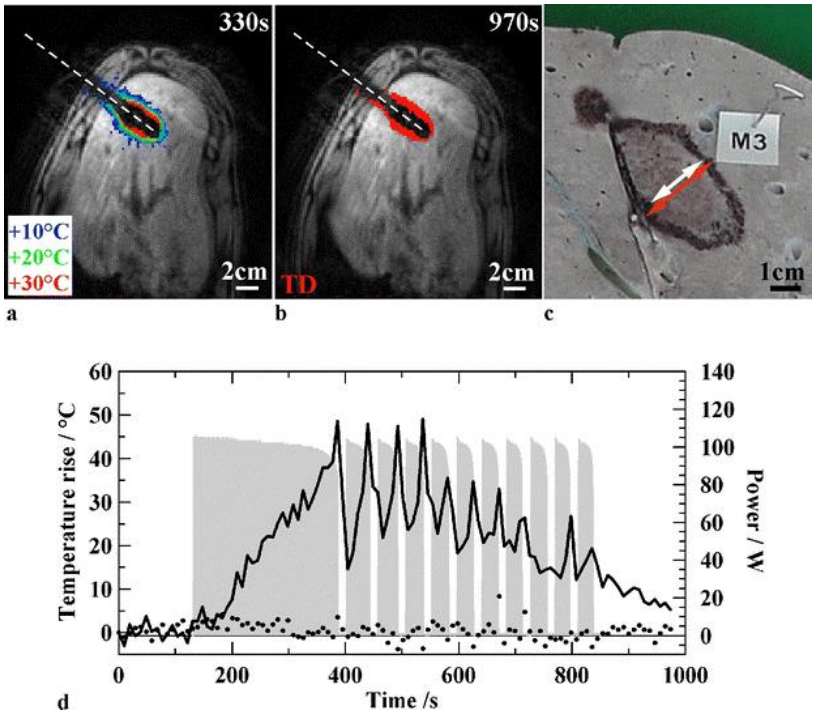


**Figure 2.16** In vivo RF ablation on the liver of pig, (a) MR temperature overlay on the anatomic image after 330 s, (b) Thermal dose map after 970 s at the end of treatment showing thermal damage reached tissue surrounding the RF applicator, (c) Macroscopic image of ablation zone after liver fixation in which diameter of the ablated zone (white and red arrows) is measured perpendicular to RF applicator, (d) Temperature change during thermal ablation, input power is demonstrated in gray, black dashed and dotted lines indicate the temporal evolution of temperature in 10 mm and 40 mm away from the applicator which is illustrated in dashed white line (Image reproduced with permission of Springer from European Radiology, Real time monitoring of radiofrequency ablation based on MR thermometry and thermal dose, vol. 18, 2008, 408-16, O. Seror et al. **[122]**)

A major drawback of PRF phase mapping method is sensitivity to motion inside the MR scanner. For in vivo procedures, movement of the rodent inside the device while scanning causes motion artifacts such as blurring and ghosting in anatomical images and also, it's an impediment

for temperature measurements [123]. According to equation 6, the subtraction of phase images is proportional to temperature change, however, movement of the object alters the position of specific area in each image with respect to the baseline image. Therefore, to circumvent this problem, different methods such as referenceless and multi-baseline method have been investigated [124]–[126].

***US thermometry***

Sound waves transmitted to organs inside the body by piezoelectric transducers are partially reflected due to the variety of tissues and organs density. The high frequency reflected beam waves are detected by piezoelectric transducer, converted to electric signals with different strength carrying anatomical information and thus constructing US images.

The goal of US imaging guidance, the same as other imaging techniques, is to localize the tumor site and its boundaries inside the organs. US imaging may not be repeatable due to its operator dependency in finding the target tumor, inconsistency and artifacts caused by bone and air interaction with US beams that decrease the quality of imaging. US is better defined for imaging superficial soft tissue. In comparison to MRI images and MRI-HIFU guidance, organs and abnormal tissues visualization is of lower spatial and temporal resolution with US and also, US is not capable of measuring temperature change [107]. However, some developments exist that improves the US thermometry for guiding HIFU ablation monitoring [127], [128].

Besides all the weaknesses of US compared to MR treatment guidance discussed above, US imaging hast its own merits and strengths. US is an available, small and inexpensive device. Because of its real time monitoring ability, the whole tumor treatment procedure can be visualized along with a variety of changes that occurs in tumor, marginal tissues and also blood flow. Although, sometimes tumor disappears during treatment when temperature increases. US

thermometry employs different image acquisition geometries including passive, pulse-echo, and hybrid which are briefly described below [129].

In *passive* geometry, thermal strain and cavitation are influenced by temperature change dependent characteristics including speed of sound and beam attenuation, leading to the ability of ablation temperature monitoring. A diagnostic transducer receives the acoustic beams emitted from the HIFU treated ablation zone [129]. In some cases, the beam generating transducer, the active transducer, and the diagnostic one, passive transducer, are the same [130].

As for *pulse-echo* imaging, same transducer is utilized for generating and receiving signals. During the pulse-tissue interaction, temperature dependent parameters may be altered and produce some acoustic echoes which can be used for temperature estimation. In both of the above geometries, single or array elements can be used for monitoring. Array elements can monitor a wider range of tissue [129].

*Hybrid* method combines ultrasonic imaging with an alternative imaging modality to improve the performance of thermometry. Photoacoustic is of great interest which uses US images with high spatial resolution and low contrast combined with optical imaging with reciprocal features where the inner chromophores result in high contrast image. In summary, optical laser produces a sharp with low bandwidth pulse, leading to temperature distribution and elevation and consequently, generating acoustic waves. These acoustic waves are received by diagnostic transducer, generating photoacoustic images [129].

***CT Thermometry***

As with US and MR thermometry, computed tomography (CT) scans possess a CT number which is temperature dependent allowing the noninvasive X-ray CT scan to provide thermal map during thermal therapy procedures. A major drawback of CT compared to MRI-based thermometry

is the patient exposure to radiation for acquiring CT scans. However, CT scans are available at lower costs compared to MRI scanners. CT number is a function of the density of the treated tissue which in turn changes with temperature modification [131]. During thermal therapy, temperature of target region increases leading to tissue expansion and density reduction. Fig. 2. 17 reports the dependency of CT scans on the temperature.

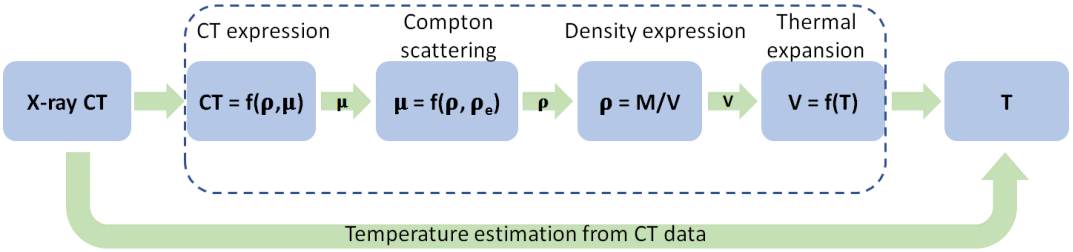


**Figure 2.17** The dependency of CT value on temperature (illustration adapted from reference **[131]**)

### 2.2.7. Feedback Control Techniques

As for the different strategies of thermal therapy, the amount of temperature change and blood flow rate differ. Thermotherapy procedure cannot follow the same heating and therapy pattern due to different tissue properties in each individual, unknown fluctuations of blood perfusion and undefined disturbance. The need for adjusting the thermal dose and keep track of temperature change necessitates using a feedback control, particularly during long time heat exposure such as mild hyperthermia experiments. In order to reach the desired treatment plan during the practical experiments, temperature dependent tissue properties, blood perfusion rate, post treatment thermal effects while limiting thermal damage to healthy tissues should be incorporated in simulations along with feedback control loop to increase the accuracy of simulation evaluations.

Target temperature during thermal therapy is locally monitored either invasively inserting temperature sensors measuring temperature in specific spots [132], [133] or non-invasively utilizing imaging modalities providing spatial temperature map.

Real time monitoring is a prerequisite for non-invasive feedback control. By way of real time monitoring, thermal dose delivering to the correct region is displayed and, consequently, feedback control can be adjusted to keep the experiment parameters in line with the experiment goal. Feedback controlled closed loop system can be designed based on the temperature and heat energy distribution and thermal zone estimation [134]–[138]. Controllers such as PI [138], [139], PID, multipoint adaptive control [140] and linear quadratic regulator [141] can be optimized based on the outcome of simulations. Estimating temperature change based on the pattern of derived temperature profiles throughout the whole procedure may also be helpful for optimizing model predictive controller especially in the case of continuous thermal dose effects after turning of the thermal source [142].

Magnetic Resonance Focused Ultrasound System (MRgFUS) is displayed in Fig. 2.18. In this system, a 16 element annular array is coupled to the animal resting position while performing feedback control maintaining temperature in the desired range.

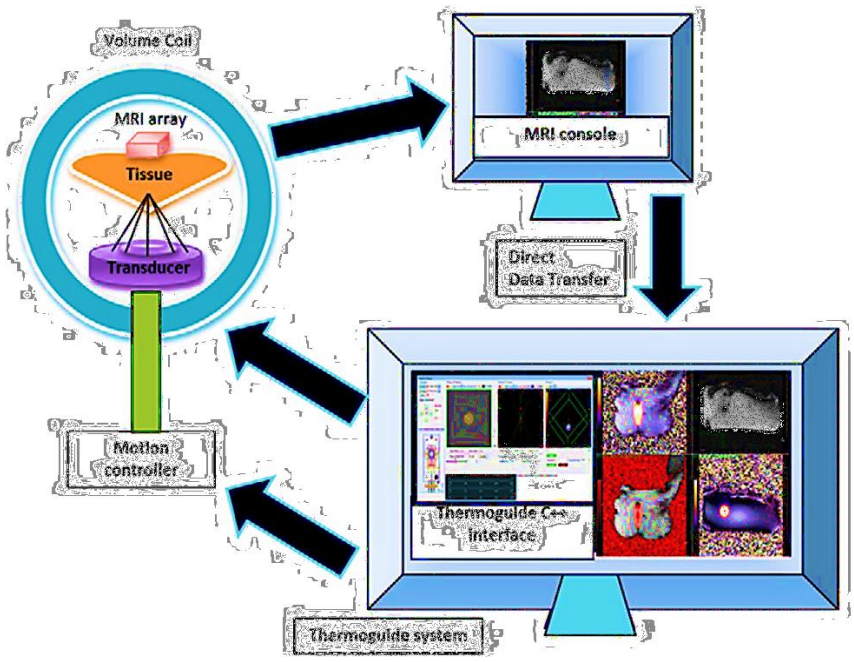


**Figure 2.18** An example of feedback controlled MFgFUS procedure (Image reproduced from Fite BZ et al., (2012) Magnetic resonance thermometry at 7T for real-time monitoring and correction of ultrasound induced mild hyperthermia. PLOS One 7(4): e35509. doi: 10.1371/journal.pone.0035509 **[143]**)

MRI-HIFU is considered as a noninvasive and accurate image guided thermal therapy system because of its ability of real time temperature monitoring. Conjunction of MRI-HIFU with feedback control in hyperthermia experiment possesses a variety of advantages:

- Providing anatomic information to manage the system settings
- Real time temperature monitoring to limit damage to healthy tissue
- Applying control feedback on the input power in correspondence to temperature change to keep the temperature in the mild hyperthermia range (39-42 °C)

Figure below shows temporal evolution of temperature elevated and maintained constant inside the target utilizing a binary feedback control integrated with MRI-HIFU hyperthermia system. Temperature map confirms the fact that temperature decreases with distance from the target.

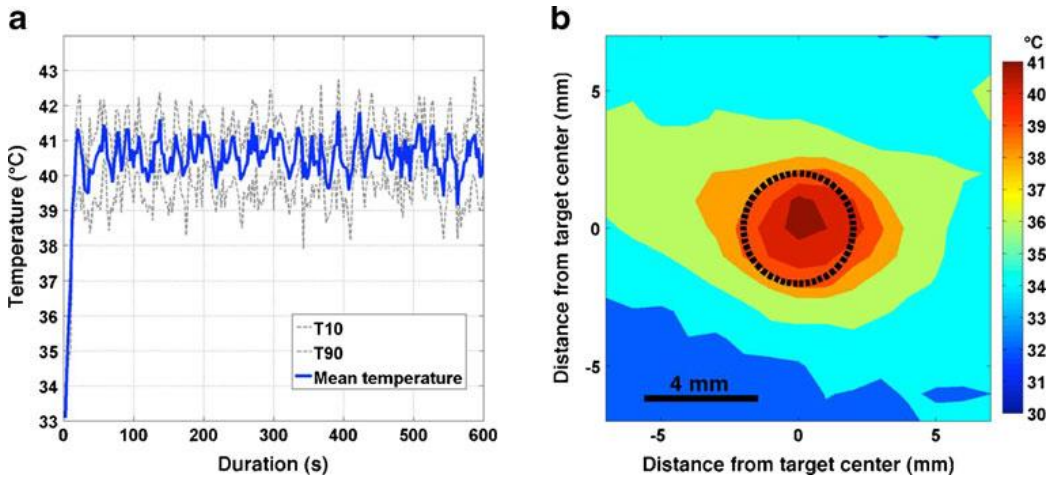


**Figure 2.19** Temperature profile during MRI-HIFU hyperthermia experiment, (a) Temperature acquired by MR thermometry, (b) Time averaged temperature distribution inside and around the target (black dashed line) (Image reproduced with permission of Springer from Pharmaceutical Research, MRI-guided monitoring of thermal dose and targeted drug delivery for cancer therapy, vol. 30, 2013, 2709-17, R. Fernando et al. **[105]**)

## 2.2.8. Post-treatment Verification

Post processing has always been an important system in computer aided diagnosis (CAD) systems. Post processing techniques improve the quality of obtained image for a clearer visualization and higher analysis performance. Most common post processing methods includes contrast enhancement [144]–[149], image denoising [150]–[153] and filtering. Contrast increase can also occur during the experiment and, therefore, obtaining an enhanced image as the outcome of the scanning.

Temperature sensitive contrast agents can be injected to the sample, ex vivo or in vivo, to enhance the thermal therapy image guidance. Gadolinium has gained interest among researchers as a MRI contrast agent [154], [154]. Gadolinium is a composition of paramagnetic thermosensitive liposomes which go through a phase transition based on a defined temperature. In vivo application of contrast agents are also investigated in which utilizing non-toxic agents holds a great significance [155], [156].

# 3. Simulation-based design and characterization of a microwave applicator for MR-guided hyperthermia experimental studies in small animals[2]

## 3.1. Introduction

Mild hyperthermia, moderate heating of tissue within the temperature range 40- 44 °C for 30-60 minutes, has been clinically applied as an adjuvant therapy for sensitizing tumor cells to radiation and/or chemotherapy. The objective of clinical hyperthermia procedures is to maintain therapeutic temperatures within the targeted tissue for the duration of the procedure, while restricting temperature of non-targeted tissues below a specified threshold [158]. This is often challenging because tissue biophysical properties, especially blood perfusion, vary widely across patients and during the course of the hyperthermic exposure [38]. Treatment outcome following hyperthermia procedures is linked to the ability to deliver desired thermal dose profiles [159], [160]. Thus, practical systems for delivering hyperthermia should include methods for monitoring spatio-temporal temperature profiles so that energy delivery can be adjusted in real-time to achieve the desired thermal dose objectives. Hyperthermia delivery techniques and methods for temperature monitoring were recently reviewed by Faridi et al [45].

---

 This chapter was published as: P. Faridi, S. H. Bossmann, and P. Prakash, "Simulation-based design and characterization of a microwave applicator for MR-guided hyperthermia experimental studies in small animals," *Biomed. Phys. Eng. Express*, vol. 6, no. 1, p. 015001, 27 November 2019. https://iopscience.iop.org/article/10.1088/2057-1976/ab36dd [157]

In addition to the therapeutic applications that are already in clinical use, the use of mild hyperthermia for modulating the anti-tumor immune response [161]–[163], targeted drug delivery [164]–[166], and other applications, is under investigation as the focus of ongoing research.

Small animals have long been used for experimental tumor models as they can be genetically manipulated to host human disease, making them a powerful tool for researchers investigating the biological effects of anti-tumor therapies, including heating [24], [167], [168]. Similar to delivery of hyperthermia in humans, investigations in small animals require instrumentation suitable for delivering desired thermal dose profiles to targeted sites. Due to the considerably smaller size of small animals, investigations of therapeutic heating in small-animals often requires the development of instruments optimized for their size. An additional challenge during application of heat to small animals is maintaining core body temperature within normothermic limits.

Hyperthermia may be administered with a variety of energy modalities, including high-intensity focused ultrasound (HIFU) [143], [168]–[172] and electromagnetic energy, such as laser [106], [173], radiofrequency [174] and microwave [81], [83], [175] modalities. HIFU offers the advantage of non-invasive and precise energy delivery (~2 mm focal spot) due to the short wavelength and large penetration depth of acoustic energy at ultrasonic frequencies. However, the use of HIFU may not always be feasible because acoustic energy does not pass through bone and air in a controlled manner. Another commonly used technique for delivering hyperthermic exposures to small animals is the immersion of the tumor in a temperature-controlled water bath [166]. The water bath is easily administered, but since heating originates from thermal conduction, it can be difficult to achieve therapeutic temperatures within deep targets without overheating the skin and other organs that may be in thermal contact with the water bath. This places constraints

on the use of water-bath for applications where limiting heating to non-targeted tissues is essential e.g. survival studies.

Microwave applicators operating at 2.45 GHz have been applied to mild heating of tumors in various small animal targets, including: bladder [83], lung [81], [176], and implanted tumors in the flank [177], [178] and hind limb [175]. A simulation-based approach was used to design and characterize a water loaded 2.45 GHz microwave applicator for delivering mild hyperthermia to the murine bladder [83]. In vivo studies showed that the applicator could be used to heat small tumors, at a depth of 2 - 3 mm beneath the skin, to the hyperthermic range, while maintaining core temperature below 40 °C.

We have previously developed an experimental platform for delivering mild hyperthermia to experimental small animals integrated with ultra-high field 14.1 T MR thermometry [175]. The accuracy of MR thermometry at 14.1 T vs. fiber-optic thermometry was established (maximum discrepancy between MRI and fiber-optic thermometry ~ 0.4 °C) and an MR compatible 2.45 GHz directional water-cooled microwave applicator was employed to heat implanted 4T1 tumors (murine breast cancer) in the hind limbs of mice [175]. While this study demonstrated the feasibility of heating small-animal targets and simultaneously monitoring temperature profiles with 14.1 T MRI, the relatively broad heating profiles of the proof-of-concept applicators is not well suited for experimental studies where limiting heating in non-targeted tumors is essential.

The objective of this study was to employ computational models to characterize the design of the proof-of-concept microwave applicator to focus heating (4 °C < $\Delta$T < 5°C) within 2 – 4 mm targets located at 1 - 3 mm from the applicator surface, with minimal heating of adjacent regions ($\Delta$T < 4 °C). Such an applicator would be suitable for in vivo experimental studies in small-animals, for delivering mild hyperthermia to 2 – 4 mm diameter tumors located at depths ranging

between 1 – 3 mm beneath the skin. As a first step, we employed MRI thermometry to characterize temperature profiles during heating with a prototype microwave hyperthermia applicator in order to assess the validity of computational models of microwave heating, and to identify antenna geometry and thermal cooling parameters that have the greatest impact on temperature profiles. Next, the experimentally validated computational models were employed to identify antenna geometry and circulating water flow parameters with the objective of maximizing therapeutic heating within simulated targets, while limiting heating in other regions. Finally, the most promising applicator design was fabricated and experimentally evaluated in tissue-mimicking phantoms during experiments performed under real-time MR thermometry. During these experiments, we evaluated the ability of the designed applicator to effectively heat targets at distances 1 – 3 mm from the applicator surface.

## 3.2. Methods

### 3.2.1. Computational model of the microwave hyperthermia applicator

We employed multi-physics computational models to optimize 2.45 GHz water-cooled directional microwave applicators, similar to the design presented in [175], for non-invasive heating of targets in small-animals from a lateral position. As illustrated in figure 3.1, the applicator consists of a coaxial monopole antenna, with an eccentric monopole element displaced from the coaxial cable's central axis, and a hemi-cylindrical metallic reflector to restrict energy deposition to approximately one half of the angular expanse. Water is circulated through the reflector tube to limit waste heating along the length of the applicator, and provide adequate impedance matching of the antenna to the feedline transmission line. Computational models were implemented to mimic applicator positioning within the experimental environment.

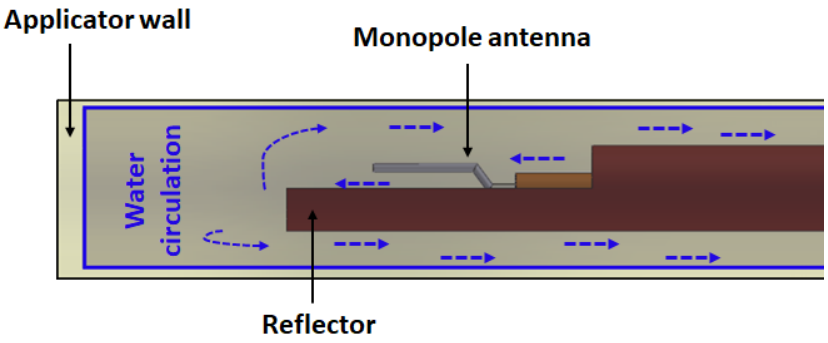


**Figure 3.1** Geometry of the distal tip of the microwave hyperthermia applicator illustrating the monopole radiating element and metallic hemi-cylindrical reflector

Here, we implemented 3D electromagnetic-bioheat transfer simulations with COMSOL Multiphysics, v 5.3. The model consists of the applicator positioned centrally within a 27 mm diameter cylindrical agar phantom, to mimic experimental procedures where the agar phantom is enclosed in a large Eppendorf tube (O.D. 30 mm; I.D. 27 mm) that fits snugly within the 30 mm imaging coil of a Bruker 14.1 T Advance III scanner. The model consists of two steps: computing the electric field radiated into the tissue and subsequently computing transient temperature profiles due to the absorbed electric field heat source. The model solves the time-harmonic Helmholtz equation to determine electric fields radiated to the tissue, subject to the following boundary conditions. The metallic parts of the applicator are defined as perfect electric conductors (PECs; i.e. conductivity, $\sigma \rightarrow \infty$). Scattering boundaries were applied on all the outer surfaces of the model, and act to absorb electromagnetic energy at the model boundaries. A coaxial port boundary condition was applied at the proximal surface of the coaxial cable's dielectric region to specify the excitation.

Two types of heat transfer models were implemented; one model simulated heating in a homogenous agar phantom and was used for experimental validation of the computational model and design optimization of the applicator. A second model, *in vivo* model, included concentric layers of skin, fat and muscle, and used the Pennes' bioheat transfer equation to account for the

effects of blood perfusion and metabolic heat generation [179]. Given the promising application of thermal models in previous studies [83], [179], [180], we employed a similar approach. Temperature dependant metabolic heat and perfusion rates after anesthesia were incorporated in the thermal models and was used to assess the impact of heterogeneity and physiological changes on the temperature profiles of the microwave applicator developed in this work. The electromagnetic power loss density, determined from the electromagnetic simulations, was used to specify the heat source. A convective heat transfer boundary condition at the outer wall of the catheter was used to approximate heat transfer due to circulating water within the applicator. For *in vivo* simualtions, we considered a multi-layer geometry incorporating multiple tissue types. The thickness of skin layer in mice ranges from 0.2 – 0.4 mm in males, and 0.13 – 0.2 mm in females, and the thickness of sub-cutaneous adipose tissue ranges between 0.05 – 0.17 mm in males, and 0.15 – 0.23 mm in females [181]. In our multi-layer model, we employed the largest thicknesses from these ranges for skin (0.4 mm) and sub-cutaneous fat (0.23 mm) layers. Table 3.1 lists material properties used in simulations.

| | Relative permittivity $\varepsilon_r$ | Conductivity $\boldsymbol{\sigma}$ $(\boldsymbol{S/m})$ | Density $\boldsymbol{\rho}$ $(\boldsymbol{kg\ m^{-3}})$ | Heat capacity $\boldsymbol{C}$ $(\boldsymbol{J\ Kg^{-1}{}^{\circ}C^{-1}}$ | Thermal cond. $\boldsymbol{k}$ $(\boldsymbol{W\ m^{-1}{}^{\circ}C^{-}}$ | Metabolic heat rate $\boldsymbol{M_A}$ $(\boldsymbol{W\ m^{-3}})$ | Blood perfusion $\boldsymbol{\omega}$ $(\boldsymbol{kg\ s^{-1}\ m^{-3}})$ |
|---|---|---|---|---|---|---|---|
| Polyimide | 3.4 [182] | - | - | - | - | - | - |
| Water | 78.6 | 1.45 | - | - | - | - | - |
| Agar phantom | 57.99 [Measured] | 2.3 [Measured] | 1300 [Measured] | 4182 [183] | 0.6 [183] | - | - |
| Muscle | 52.7 | 1.74 | 1090 | 3421 | 0.49 | 1734[179] | 2.161[179] |
| Fat | 10.8 | 0.268 | 911 | 2348 | 0.21 | 1734[179] | 2.161[179] |
| Skin | 38 | 1.46 | 1109 | 3391 | 0.37 | 2002[179] | 1.359[179] |

| | | | | | | | |
|---|---|---|---|---|---|---|---|
| Blood | - | - | 1050 | 3617 | - | - | - |

**Table 3.1** Material properties used in simulations

[a] All material properties are from [184] except the indicated ones from [179], [182], [183] and measured properties in our laboratory.

The applicator's heating pattern, as assessed by specific absorption rate (SAR) profiles, can be controlled by modifying the reflector's aperture and shape, as well as position of the monopole element, as shown in previous studies [185], [186]. The length of the monopole radiating element was restricted to 6 mm, for optimally matching the antenna at 2.45 GHz. Figure 3.2 depicts the antenna geometry parameters we investigated in this study: reflector angle ($\theta_r$), monopole element shape (line or S-shape) and displacement from the center ($m$) to control the applicator's SAR pattern.

To assess the impact of microwave applicator geometry on the heating pattern, we modeled and implemented two applicators, one with $\Theta_{r1}$ = 150 °, $m$ = 0.6 mm (applicator 1), and another with $\Theta_{r2}$ = 120 °, $m$ = 1 mm (applicator 2).

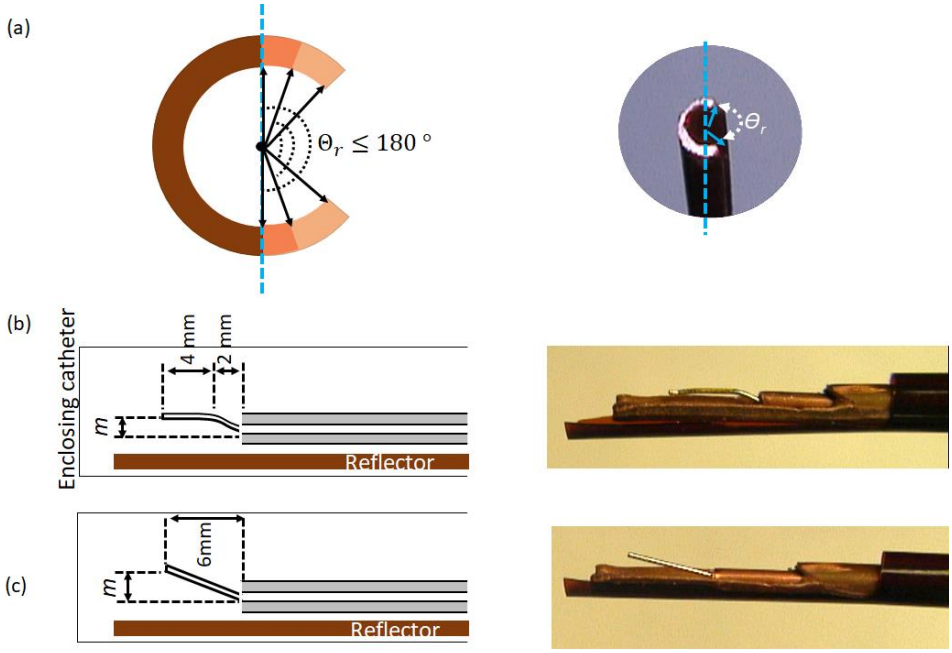


**Figure 3.2.** Schematic (left column) and photograph (right column) of fabricated microwave applicator geometry, (a) transverse view of reflector geometry, (b-c) longitudinal view of S (with 4mm monopole

element parallel to the outer catheter wall according to Sebek et al. **[186]**) and line-shape monopole radiation element with m displacement from the center of coaxial cable

Besides the antenna geometry, the temperature ($T_{\text{cool}}$) and flow rate of water circulated within the applicator were expected to have an impact on temperature profiles, particularly, the extent of tissue adjacent to the applicator that could be thermally spared. To assess the effect of convective heat transfer on thermal profiles, we conducted microwave heating experiments in tissue mimicking phantom employing three flow rates, corresponding to different convective heat coefficient ($h$), and three cooling temperatures ($T_{cool}$). Temperature profiles during these experiments were measured using MRI thermometry.

### 3.2.2. Experimental assessment of computational models

Preliminary microwave heating experiments were conducted, with temperature profiles measured using 14.1 T MRI thermometry, with the objective of providing a dataset for assessing the validity of computational models, and identifying the antenna geometry and circulating water flow parameters that have the greatest impact on thermal profiles. Specifically, we compared the measured and simulated $\Delta$T = 6 °C and 8 °C hyperthermic isotherms using the Dice Similarity Coefficient (DSC) defined using equation below, where X and Y are the measured and simulated isotherms.

$$DSC = \frac{2|X \cap Y|}{|X| + |Y|} \tag{9}$$

We conducted several microwave heating of tissue mimicking agar phantom integrated with real-time MR thermometry. During each of these experiments, one parameter of either geometry or convective heat transfer was considered as a variable while other parameters were kept constant. Table 3.2 summarizes the experimental settings of the described experiments. During these experiments, input power varied in the range of 4 – 11 W at the applicator.

**Table 3.2** Experimental settings to assess the significance of the impact of each parameter

| Variable | Geometry | $T_{cool}$ (°) | | | Water flow rate (ml/min) | | |
|---|---|---|---|---|---|---|---|
| Water flow rate | applicator 1 | $T_{phantom}$ = 16.5 | | | 50 | 150 | 300 |
| Tcool | applicator 1 | 13.5 | 16.5 | 29.5 | | 150 | |
| Geometry | applicator 1<br>applicator 2 | $T_{phantom}$ = 16.5 | | | | 150 | |
| Geometry | applicator 1<br>applicator 2 | $T_{phantom}$ = 16.5 | | | | 150 | |

MR thermometry was implemented using a FLASH sequence with the following parameters: FOV = 30 mm, image size = 128 × 128, flip angle = 15°, TR/TE = 30.15/4.0 ms, slice thickness = 1 mm, scanning duration = 3.87 s. During the experiments, MR thermometry scans were acquired either three transaxial or sagittal slices, or one transaxial and sagittal slice simultaneously. Models were implemented to mimic the experiments taking into account the two different applicator geometries and various heat transfer parameters.

### 3.2.3. Parametric design of the microwave hyperthermia applicator

The goal of the parametric design process is to adapt the microwave hyperthermia applicator design for treating targets of varying size located at varying depths within the small-animal's body. To evaluate the quality of a candidate applicator design, the following metrics were employed: (1) the fraction of the target volume covered within the desired hyperthermic range and (2) the fraction of surrounding non-target regions heated above a threshold.

A two-stage design process was employed; 1) SAR-based geometry design; controlling electromagnetic power transfer to the tissue, 2) temperature profile-based selection of convective cooling parameters; assessing the impact of thermal parameters.

In the first stage, electromagnetic simulations were employed to identify the optimal S-shaped monopole displacement, *m*, and reflector aperture angle, $\Theta_r$. The parameter *m* was varied in the range of 0 - 1 mm with the increment of 0.2 mm and $\Theta_r$ was varied between 100 – 180° with increments of 10°. Candidate designs that delivered less than 30 % of applied power to the agar phantom (i.e. 70% of microwave power was absorbed within the applicator), were discarded from further consideration, as they would require excessively large applied input powers to heat tissue, which would compromise the efficacy of surface cooling due to microwave absorption within circulating water. Similarly, candidate designs that delivered more than 70% of power to the agar phantom were also discarded, as these designs yielded broad heating patterns.

In the second stage, heat transfer simulations were employed to assess the most promising antenna designs, namely combinations of *m*, 0.4 and 0.6 mm, and $\Theta_r$, 160° to 100° with decrement of -10°, with convective heat transfer coefficient restricted to $h$ =2000 [W $m^{-2}$ $K^{-1}$] (correspondence to flow rate of 150 ml/min). The combination of *m* and $\Theta_r$ experiencing higher coverage and safety rates compared to the remaiming combinations, were saved as parametric design process applicator called *applicator 3*.

To determine the versatility of designs for delivering hyperthermia to a wide range of target sizes at varying distances from the applicator, input power and $T_{cool}$ were introduced as control variables that could be selected by the user, and that are independent of the antenna geometry. The impact of varying these cooling parameters was assessed using transient heat transfer simulations over a period of 5 mins.

Finally, the end result of this parametric design process, *applicator 3*, was incoporated in the *in vivo* model to assess the feasibility of delivering localized hyperthermia in the presence of

tissue heterogeneity taking into account the effect of anesthesia, blood perfusion and metabolic heat generation on the transient temperature profiles of *applicator 3*.

*Applicator 3* (with $\Theta_r$ = 120 °, *m*= 0.6 mm) was fabricated, as illustrated in figure 3.3. We used a 3D template with an open angle of $\Theta_r$ = 120° and an ID equal to the reflector OD (2.4 mm) to precisely machine the reflector dimensions. The monopole element was moved outward slightly greater than 0.5 mm relative to the ruler precision. The fabricated applicator has a resonance close to 2.45 GHz, and is well matched (i.e. s11 < -10 dB) over a 300 MHz bandwidth as shown in figure 3.3 (d). The performance of this fabricated prototype was experimentally evaluated during 5 min and 30 min microwave heating experiments conducted under real-time MR thermometry.

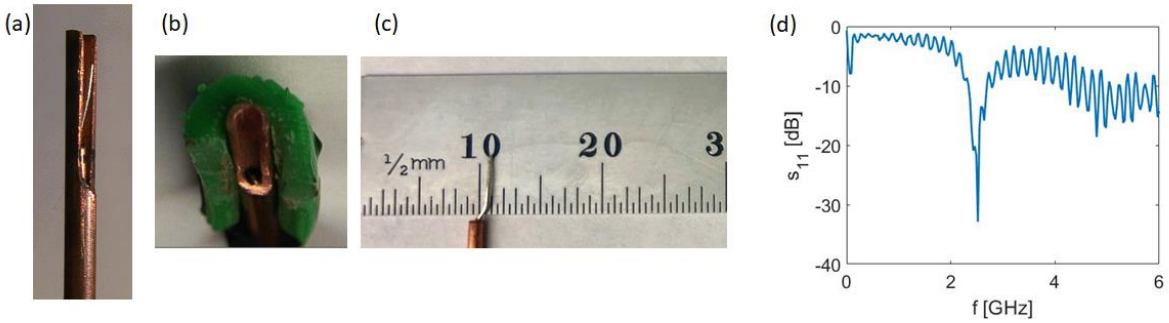


**Figure 3.3** (a) Photograph of fabricated prototype of applicator 3 (outer catheter is not enclosed), (b) Cutting the reflector cylinder to the desired angle using a 3D printed template, (c) monopole element displacement from the center (m) measured with a 0.5 mm precision ruler, (d) applicator 3 reflection coefficient.

During these experiments, a binary control scheme (i.e. bang-bang control) was employed, similar to Farr et al. 12. The objective was to modulate the input power to keep the average temperature change of the pre-defined target ROI within the range 4 - 5 °C, while ensuring the maximum temperature change in the phantom did not exceed 8 °C (corresponding to 45 °C in-vivo presuming 37 °C as a normothermic temperature). We considered circular target ROIs with diameters of 2, 3 and 4 mm while specifying the distance between the applicator edge and ROI boundary as 1, 2, and 3 mm. Real-time temperature monitoring was performed using Thermoguide (IGT, Pessac, France), an MRI based temperature imaging software. To assess the performance of

the end result of parametric design process geometry and thermal design, we employed two cost functions to quantify the quality of the hyperthermic exposure: coverage and safety. The coverage metric defines the fraction of the target volume heated to the target temperature range (i.e. 4 °C < ΔT < 8 °C). The safety metric is defined as the volume of the surrounding tissues (i.e. non-targeted regions) with temperature rise below 4 °C. Both the coverage and safety metrics are computed during the interval of time over which the binary controller was activated (See Fig. 3.10). Coverage and Safety were defined using the following functions:

$$\text{Coverage} = \int \frac{4\,^{\circ}C < Control\ ROI < 8\,^{\circ}C}{Control\ ROI} dv \tag{10}$$

$$\text{Safety} = \int \frac{Surrounding\ tissue < 4\,^{\circ}C}{Surrounding\ tissue} dv \tag{11}$$

Since these metrics are competing, a desired applicator design and/or treatment delivery parameters has to be selected to balance the coverage and safety as prescribed by the constraints of the specific subject.

## 3.3. Results

### 3.3.1. Primary experimental characterization of microwave hypertehrmia applicators

MRI thermometry maps and radial temperature profiles within agar phantoms after 5 min microwave heating are shown in figure 3.4. These data illustrate that the reflector aperture angle, $\Theta_r$, and the monopole shape and displacement, *m*, considerably affect the peak temperature and width and depth of the hyperthermic zone and provide degrees of freedom for modulating thermal profiles. Using the S-shaped monopole leads to more uniform heating along the applicator length, as demonstrated by the radial temperature profiles in different transaxial planes illustrated in figure

3.4 (d) and 3.4 (h). Further, the S-shape monopole affords thermal sparing of tissue immediately adjacent to the applicator, which is not feasible with the line-shaped monopole.

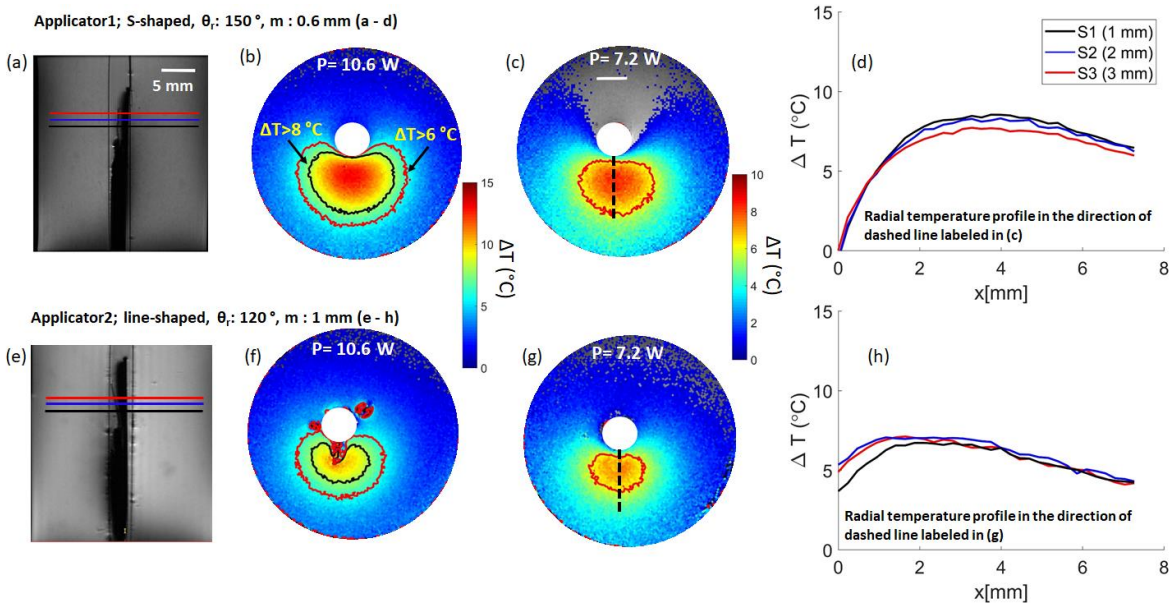


**Figure 3.4** MR thermometry temperature measurements after 3 and 5 minutes of heat exposure in a transaxial slice S2 with 10.6 W (b and f) and 7.2 W (c, d and g, h) input power, respectively using, (b - d) applicator 1, (f - h) applicator 2, (d) and (h) show the radial temperature profile in the direction of maximum heating labeled in (c) and (g), (three horizontal lines in sagittal views of the applicators inserted inside the phantom, (a) and (e), are showing three transaxial MR thermometry slices, S1, S2 and S3).

Figure 3.5 shows the impact of varying the circulating water flow rate and temperature, $T_{cool,}$ on radial temperature profiles when using applicator 1 in an agar phantom. Figure 3.5 (a) demonstrates that using a water flow rate of 150 ml/min enables sparing of regions adjacent to the applicator surface, while this region is heated to the hyperthermic range when using lower and higher flow rates. The effect of three different values of $T_{cool}$ on radial temperature profiles is shown in figure 3.5 (b). Increased $T_{cool}$ leads to higher maximum temperatures, as well as decreased radial penetration of hyperthermic zones, thereby increasing the risk of overheating the skin surface.

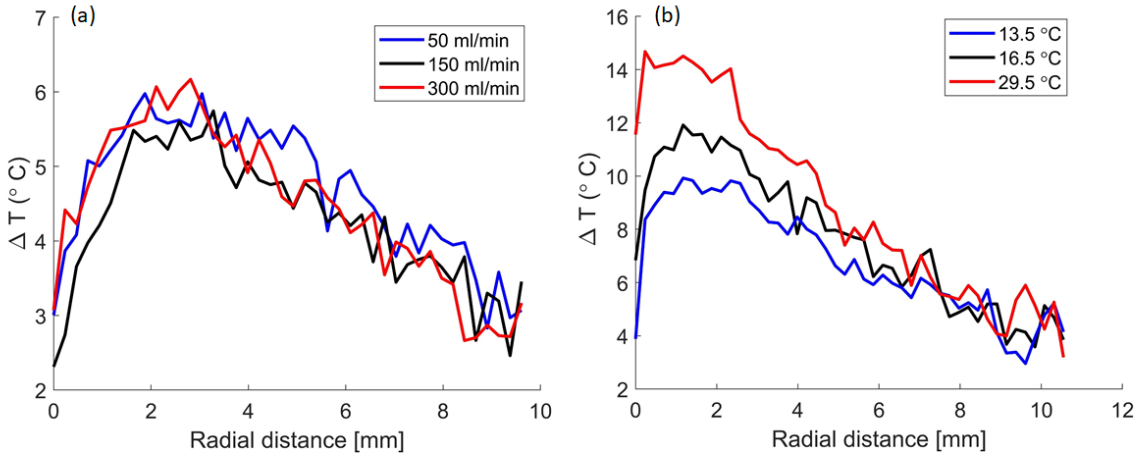


**Figure 3.5** Temperature profiles measured with MR thermometry while (a) water flow rate and (b) $T_{cool}$ are adjusted.

### 3.3.2. Experimental assessment of computational models

Simulated and experimentally measured temperature maps are illustrated in figure 3.6. The DSC between the simulated and measured ΔT= 6 °C and 8 °C isotherms were 0.97 ± 0.02 and 0.98 ± 0.01, respectively, which suggests that computational model predicts temperatures that are in alignment with experimental measurements. We have previously comparatively assessed the validity of simulated transient temperature profiles in multiple ROIs with MR thermometry and the maximum error between simulated and MR measured temperatures were 0.7 °C [187].

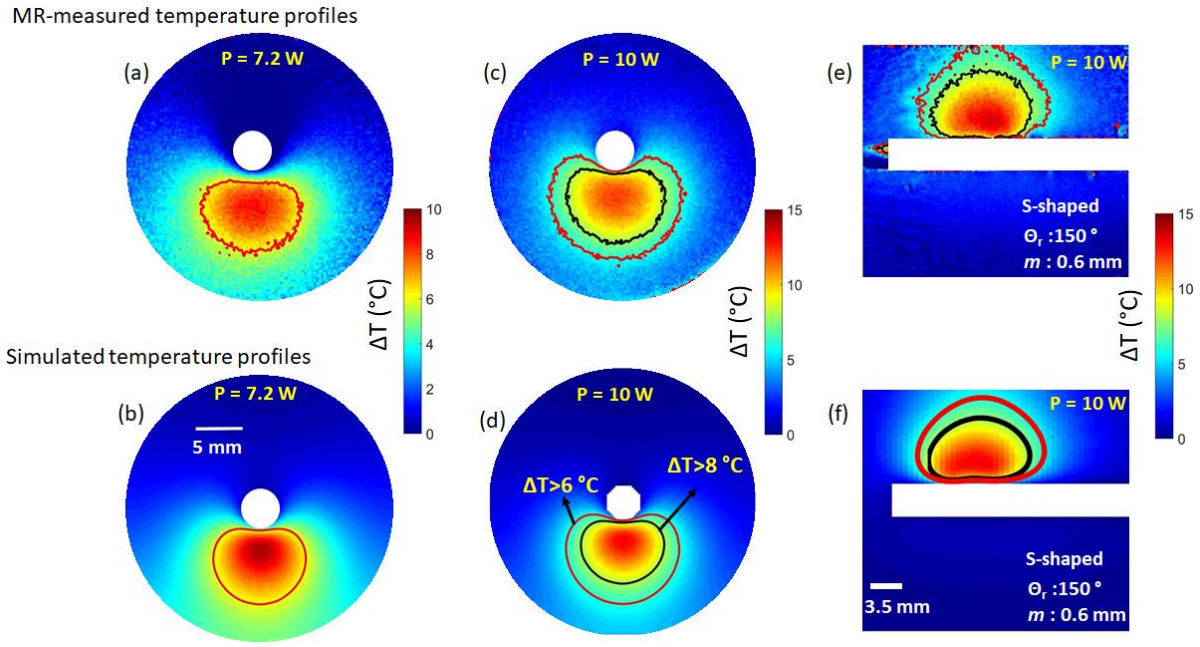


**Figure 3.6** Experimentally measured (first row) and simulated (second row) temperature profiles after (a-b) 5 min of heat exposure with an input power of 7.2 W in transaxial view, (c-d) and (e-f) 3 min of heat exposure with an input power of 10 W in transaxial and sagittal view, respectively. Circulating water temperature ($T_{cool}$) is equal to phantom temperature ($T_{phantom}$) with flow rate of 150 ml/min. Full white circles and rectangles show the antenna position.

### 3.3.3. Simulation-based parametric design and simulations under *in vivo* conditions

Figure 3.7 displays normalized SAR profiles of a range of candidate applicator designs with varying Θr and *m* . Based on these simulations, the number of candidate designs was narrowed down to 8 from an initial 30 combinations of Θr and *m*, by considering only those applicators where the power deposited within the phantom ranged between 30 – 70 % of the applied power.

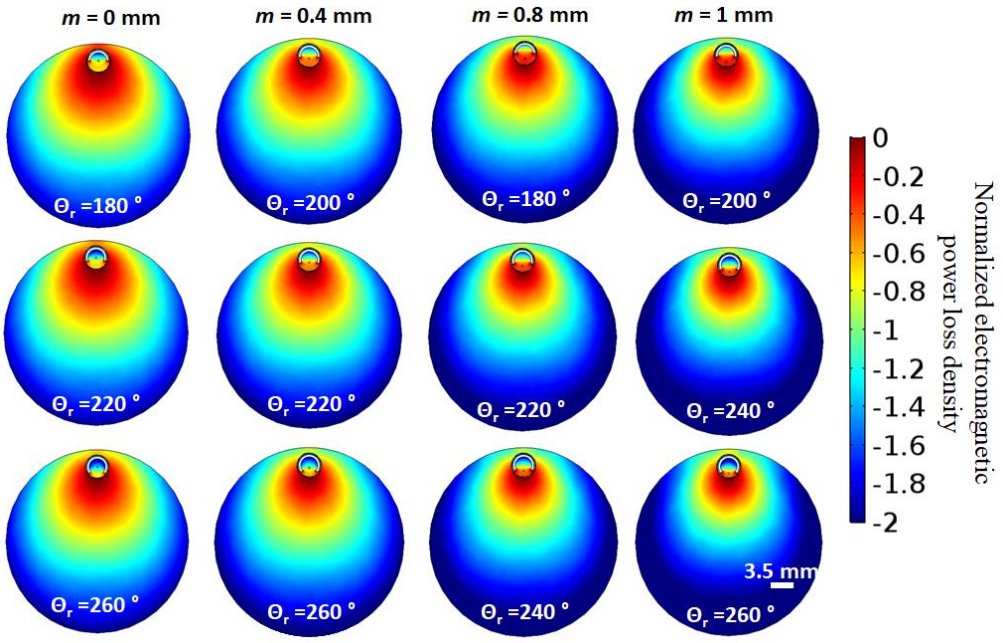


**Figure 3.7** Normalized SAR profile of applicator designs employing varying combinations of Θr and m (profiles are shown here for 12 out of a total 30 combinations that were investigated).

At the end of thermal simulations, applicators with m = 0.4 mm and Θr = 140° and m = 0.6 mm and Θr = 120° yielded higher Coverage and safety values compared to the rest of combinations. While both of these geometries could be employed for delivering hyperthermia to the target with similar coverage and safety values, the applicator with m = 0.6 mm and Θr =120° was selected as the end result of the parametric design process, applicator 3, because of its adaptibility to larger number of target sizes and distances from the surface. Figure 3.8 depicts variations of temperature profiles in phantoms following heating with the optimal applicator design (Θr = 120° and m = 0.6 mm), when using different combinations of applied power and Tcool. Figure 3.8 further illustrates that applicator 3 (Θr = 120° and m = 0.6 mm), enables a range of temperature profiles that can be achieved with other applicator geometries, simply by adjusting the applied power level and Tcool. Importantly, adjusting applied power level and Tcool for other applicator geometries, provided only limited flexibility in modifying hyperthermic profiles.

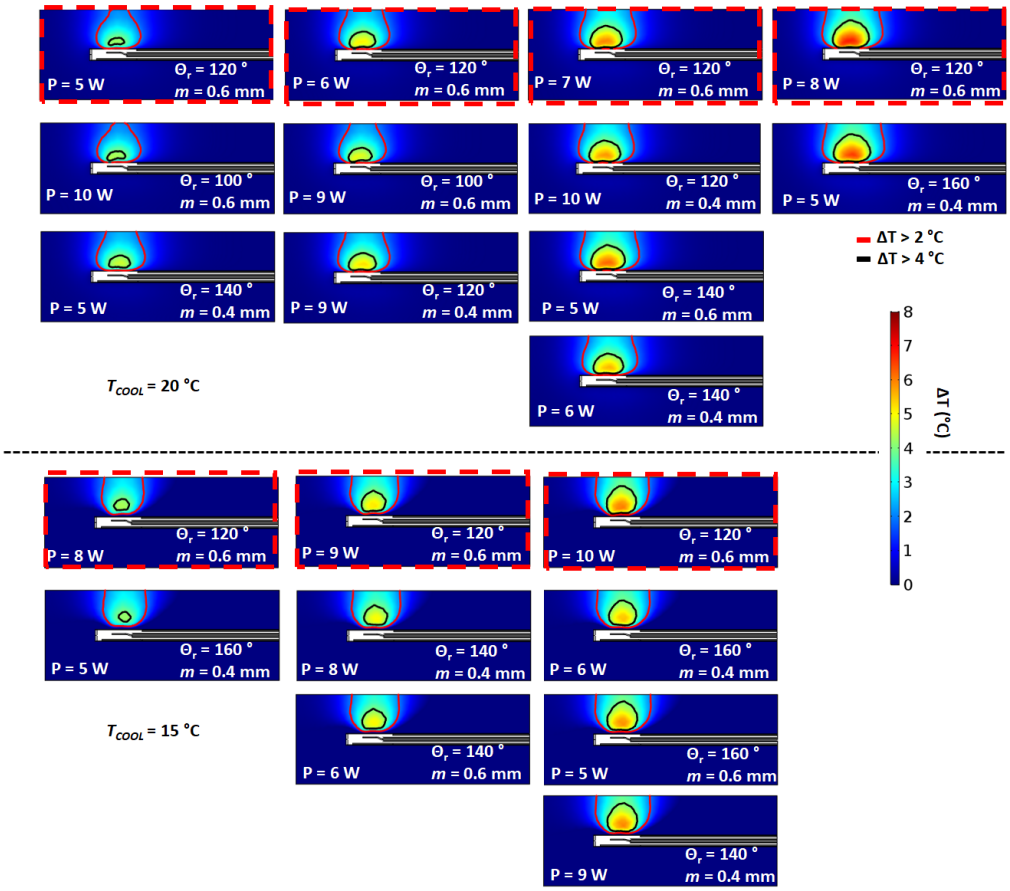


**Figure 3.8** Simulated temperature profiles among the 8 remaining combinations of Θr and m from SAR patterns that are well-suited for hyperthermia delivery to small tumors at t = 300 s with input powers of P= 5, 6, 7, 8, 9 and 10 W, $T_{cool}$ = 15°C or 20 °C while $T_{phantom}$ is 20 °C. The red dashed border indicates the selected optimal design. Each column shows that temperature pattern achieved with the optimal desgin, by appropriately choosing applied power and $T_{cool}$, spans the range of temperature profile achieved by applicators with other Θr and m combinaions; emphasizing that the optimal design embraces all the possible hyperthermic temperature profiles.

Figure 3.9 depicts transient temperature profiles of *in vivo* model using *applicator 3* which restricts the extent of heating to the tumor site with minimal collateral heating.

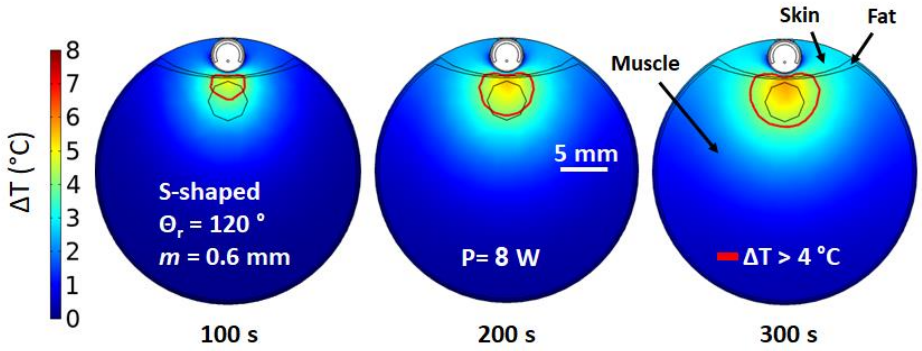


**Figure 3.9** Transient temperature profiles of in vivo simulation using applicator 3

### 3.3.4. Experimental evaluation of optimal applicator design

Figure 3.10 illustrates MRI thermometry profiles following 7 W, 5 min heating of agar phantom using *applicator 3* (Θr = 120° and *m* = 0.6 mm). Temperature profiles are shown for exposures with and without feedback-control. Figure 3.10 (b) shows the average transient temperature during the application of binary temperature control (figure 3.10 (c)) which kept the average temperature of ROI (r = 1mm and D = 2 mm) in the target hyperthermic range.

To evaluate the performance of *applicator 3* for delivering hyperthermia to the target, control targets were defined, with *r* = 1, 1.5 and 2 mm, and D = 1 – 3 mm from the applicator surface (figure 3.11). Tables 3.3 and 3.4 include coverage and safety rates in transaxial and sagittal planes of each of the controlled hyperthermic experiments conducted with $T_{cool} = T_{\text{phantom}}$ and $T_{cool} = T_{\text{phantom}} - 5°C$.

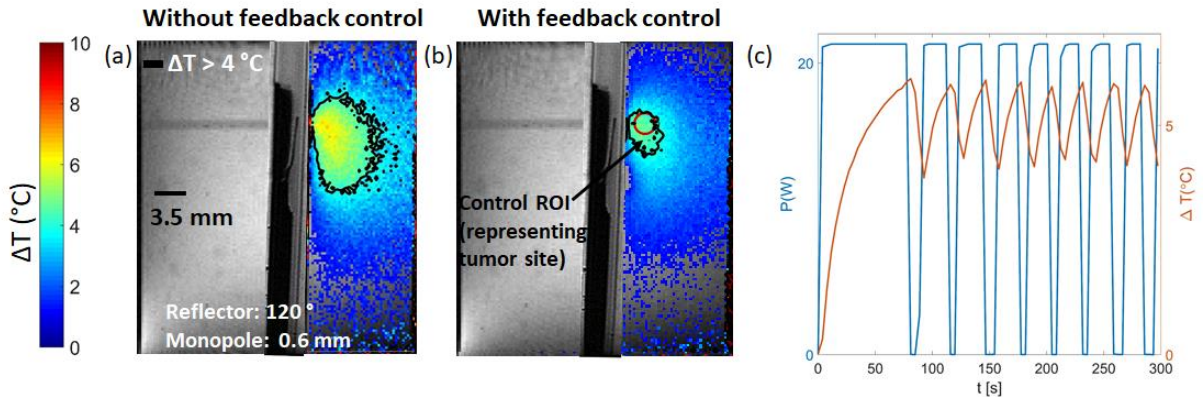


**Figure 3.10** (a) temperature profile measured by MR thermometry with P = 7 W at the applicator at t = 300 s, (b) Average temperature profile during feedback-controlled heating, (c) Input power termination (21 W at power meter was equal to 7 W) and average temperature of the target ROI during feedback-controlled heating. $T_{cool}$ and $T_{phantom}$ were both 18.5 °C with water flow rate of 150 ml/min**.**

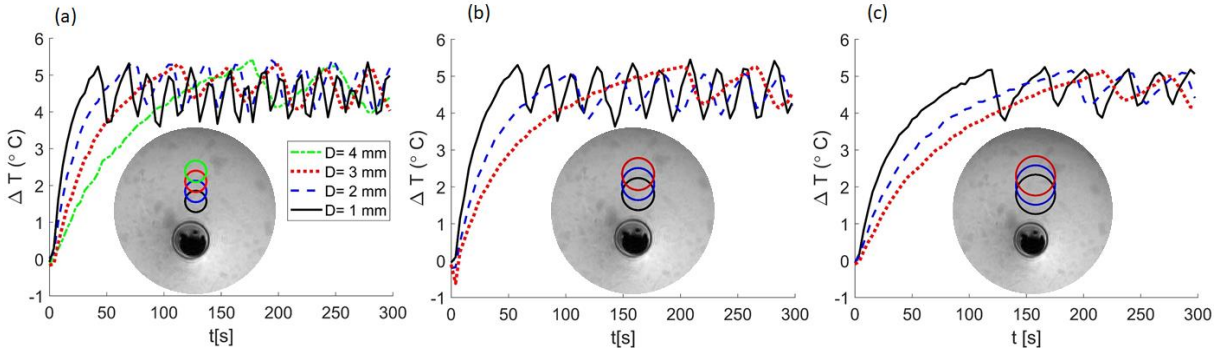


**Figure 3.11** Temperature maps during 5 min heating (P=8 W) to maintain average temperature change of control ROIs with radius (a) 1 mm, (b) 1.5 mm and (c) 2 mm, in the range of 4 - 5 °C utilizing binary feedback control. D indicates the distance between the applicator edge and closest ROI boundary.

**Table 3.3** Coverage and safety of the controlled hyperthermia experiments in phantoms at a time following activation of the binary controller with Tcool = Tphantom

| **P= 8 W** | | **Sagittal** | | **Axial** | | **Coverage [%]** | | | | **Safety [%]** | | **SS** |
|---|---|---|---|---|---|---|---|---|---|---|---|---|
| **r (mm)** | **D (mm)** | **Max (°C)** | **Ave (°C)** | **Max (°C)** | **Ave (°C)** | **Sagittal** | | **Axial** | | **Sagittal** | **Axial** | **t [s]** |
| | | | | | | **Max** | **Ave** | **Max** | **Ave** | | | |
| **1** | **1** | 6.8 | 4.2 | 7.7 | 4.3 | 100 | 86 | 99 | 88 | 89 | 80 | 43 |
| | **2** | 7.1 | 4.3 | 7.6 | 4.4 | 100 | 86 | 100 | 87 | 88 | 79 | 73 |
| | **3** | 6.9 | 4.1 | 7.5 | 4.2 | 99 | 84 | 99 | 84 | 87 | 78 | 112 |
| **1.5** | **1** | 6.7 | 3.9 | 7.5 | 3.9 | 100 | 84 | 100 | 84 | 88 | 80 | 58 |
| | **2** | 7.4 | 4.2 | 8.1 | 4.3 | 98 | 75 | 98 | 77 | 87 | 79 | 104 |
| | **3** | 6.8 | 3.9 | 7.7 | 4.1 | 91 | 74 | 97 | 76 | 87 | 79 | 178 |

| | | | | | | | | | | | | |
|---|---|---|---|---|---|---|---|---|---|---|---|---|
| **2** | **1** | 6.9 | 3.8 | 7.4 | 4 | 99 | 93 | 99 | 86 | 84 | 77 | 120 |
| | **2** | 7.2 | 4 | 8 | 4.2 | 93 | 81 | 95 | 83 | 80 | 76 | 190 |
| | **3** | 7.7 | 4.5 | 7.8 | 4 | 93 | 77 | 96 | 80 | 77 | 74 | 207 |

**Table 3.4** Coverage and safety of the controlled hyperthermia experiments at a time following activation of the binary controller with Tcool = Tphantom – 5 °C

| **P= 8 W** | | **Sagittal** | | **Axial** | | **Coverage [%]** | | | | **Safety [%]** | | **SS** |
|---|---|---|---|---|---|---|---|---|---|---|---|---|
| **r (mm)** | **D (mm)** | **Max (°C)** | **Ave (°C)** | **Max (°C)** | **Ave (°C)** | **Sagittal** | | **Axial** | | **Sagittal** | **Axial** | **t [s]** |
| | | | | | | **Max** | **Ave** | **Max** | **Ave** | | | |
| **1** | **1** | 6.6 | 4.2 | 7.4 | 4.2 | 100 | 77 | 99 | 73 | 89 | 80 | 104 |
| **1.5** | **1** | 6.8 | 4.1 | 7 | 4.3 | 96 | 72 | 98 | 74 | 89 | 79 | 66 |
| **2** | **1** | 7.2 | 3.9 | 7.9 | 4 | 91 | 74 | 95 | 76 | 84 | 77 | 208 |

Figure 3.12 illustrates the operation of the feedback-controlled power delivery approach and transient temperature profiles during 30 min of heat exposure. Figures 3.11, 3.12 and tables 3.3 and 3.4, illustrate the capability of *applicator 3* to deliver and maintain hyperthermic temperature to the targets of diameter 2 - 4 mm within 1 - 3 mm distance from the applicator surface.

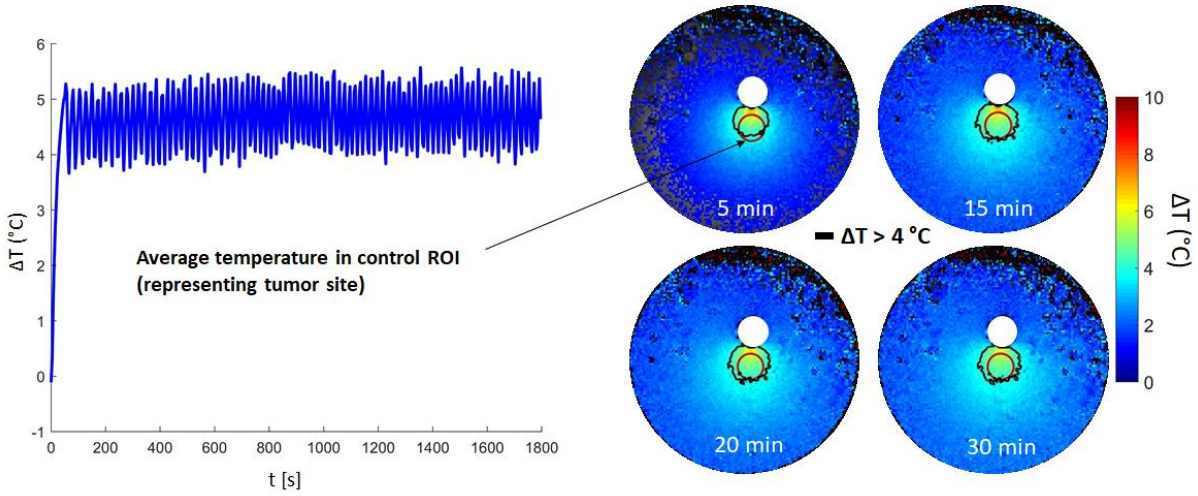


**Figure 3.12** (a) Average temperature of target sized 3 mm in diameter located at 1 mm from the applicator boundary incorporating binary feedback control to trigger the input power (P= 7 W), (b) transient temperature profiles during 30 min heat exposure

## 3.4. Discussion

Localized hyperthermia treatment requires (1) precise energy delivery to the targeted tissue and (2) maintaining the temperature in the hyperthermic range for 30- 60 minutes. In this work, we have optimized a previously presented non-invasive 2.45 GHz directional water-cooled microwave applicator to limit the extent of hyperthermic zone to 1 – 3 mm targets and preserve surrounding tissue. Real-time MR temperature monitoring and feedback control enabled maintaining temperature within the hyperthermic range. An advantage of the described system is it enables precise delivery of hyperthermia to small target sites with an easy to implement microwave applicator. Specifically, hyperthermic profiles to 1 – 3 mm targets could be controlled through selection of applied power level and $T_{cool}$. Compared to small-animal hyperthermia systems employing focused ultrasound, which may offer extended control of heating to deep seated targets, the presented system may afford simplified hyperthermia delivery, as it does not require careful selection of phased array excitation parameters [143], [169].

We evaluated the impact of geometrical and thermal design of the microwave applicator on the temperature profiles. The evaluation of experimentally measured temperature profiles using the fabricated applicators with different geometrical design indicated that the reflector angle, Ɵr, and monopole displacement from the center, *m*, modify the width and depth of the heating pattern and peak temperature. Specifically, increasing *m* moves the radiating monopole closer to the targeted tissue, which results in greater electromagnetic power absorbed within the tissue. Conversely, increasing Ɵr results in more power remaining within the catheter. In addition to Ɵr and *m*, the monopole antenna shape impacted the ability to shift the onset of the hyperthermic zone from immediately adjacent to the applicator surface, to deeper regions within tissue. This may be important because of the need to thermally spare the skin surface for several applications (figure

3.4). During experimental evaluation of thermal parameters, using a convective heat transfer rate of 150 ml/min increased radial penetration of the peak temperature from the surface of the applicator compared to flow rates of 50 ml/min and 300 ml/min (figure 3.5). This enables increased skin cooling and treatment of tumors up to 4 mm from the skin surface. The choice of $T_{\text{cool}}$ relative to $T_{phantom}$ has a considerable impact on the temperature profile. High values of $T_{cool}$ leads to convective heating, in addition to direct microwave heating, which increases the tissue temperature, particularly at the applicator boundary, and broadens the extent of the hyperthermic zone (figure 3.5). Temperature rise also appears along the applicator length due to convective heating which heats up the whole tissue sample. Therefore, circulating water with higher temperature relative to tissue sample is not suitable for localized hyperthermia delivery to small animal targets. Using lower $T_{\text{cool}}$ reduces the peak temperature, as well as the width of the hyperthermic zone.

Temperature profiles predicted by the 3D computational model were comparatively assessed with MRI thermometry data from experiments in tissue-mimicking phantoms. The hyperthermic isotherms of measured and simulated temperature profiles were highly correlated (DSC = 0.95 – 0.99) for multiple input powers (figure 3.6). The validated computational models were then utilized for design and characterization of the applicator based on the normalized SAR and temperature profile. For the SAR-based parametric design (figure 3.7), monopole shape was restricted to S-shape because of the ability to thermally spare regions between the applicator edge and the hyperthermic zone. This gap lowers the risk of skin burn during *in vivo* hyperthermia treatments. From thermal simulations, using a convective heat transfer coefficient of $h$=2000 [$W/m^2 K$] (corresponding to a flow rate = 150 ml/min), $\Theta r$ = 120 °C and $m$ = 0.6 mm was selected (*applicator 3*), because compared to other $\Theta r$ and $m$ combinations, this selection enabled heating

of a wider range of target sizes at greater distances from the skin, while maintaining a similar safety rate. It is worth noting that the range of thermal profiles that can be achieved by *applicator 3*, by appropriate selection of $T_{cool}$ and applied power, spans the range of temperature profiles achieved by the majority of the eliminated designs, which have distinct antenna geometries (figure 3.8).

The ultimate goal of the parametric design process was to identify an applicator design suitable for delivering localized hyperthermia to small animal targets *in vivo*. The temperature profiles predicted by computational models using *applicator 3* when considering a multi-layer perfused skin, fat and muscle layer and metabolic rate after anesthesia (mimicking *in vivo* treatments) demonstrate the suitability of using the design presented in this work for localized heating of small-animal targets. Comparing the temperature profiles simulated under *in vivo* conditions (figure 3.9) in a multi-layer medium, including blood perfusion and metabolic heat generation, with temperature profiles in the homogeneous phantom (figures 3.6 and 3.8), it is apparent that, for the same applied power level, the shape of the hyperthermic zones remain similar, suggesting that the shape of the hyperthermic profiles are not substantially impacted by dielectric heterogeneity. However, for the same applied power level, the peak temperature and the volume raised to the hyperthermic temperature in *in vivo* simulations compared to homogeneous phantoms is decreased, which may be attributed to the additional heat sink terms. We anticipate that applying power using the binary feedback control algorithm would facilitiate increased peak temperatures and hyperthermic treatment zones, although these may still remain below the size of hyperthermic zones that could be achieved in homogenous phantoms. It is noted that we employed a simplified model where the skin, fat, and muscle layers were geometrically modeled as concentric cylinders. While these simulations illustrate the impact of heterogeneity and blood

perfusion and metabolic heat generation on thermal profiles compared to those simulated in homogeneous agar phantoms, models incorporating the anatomy of the animal [80], [83] may provide a more comprehensive prediction of temperature profiles for a particular administration of heating.

Integrating *applicator 3* with binary temperature-based feedback control of applied power, localized the heating to the targeted region of interest (figure 3.10). Real-time MR temperature monitoring using *applicator 3* with the application of temperature feedback control enabled precise delivery of hyperthermia to target ROIs over a narrow temperature range (4 - 5 °C) (figure 3.11). The average temperature within the targeted ROI reached the hyperthermic range within a few minutes; for example, hyperthermic temperatures for target ROIs with r = 1 mm and D = 1 mm were obtained after 43 s, and for target ROIs with r = 2 mm and D = 3 mm, after 207 s. In this study, binary feedback control was employed to terminate the input power when average temperature change of the pre-defined target ROI reached 5 °C. The uniform distribution of hyperthermic temperatures in the selected ROIs, compared to non-uniform distribution previously reported for MR-guided pancreatic hyperthermia in mice [168], may facilitate *in vivo* hyperthermia treatment for target sizes of 2 - 4 mm in diameter in 1 - 3 mm distance from the applicator yielding high target coverage (tables 3.3 and 3.4). The placement of the monopole antenna could change the maximum temperature of the target by 1 - 2 °C. However, average temperature of the target ROI remains in the hyperthermic zone with relatively high coverage and safety rates (safety = 74 - 77 %; coverage = 80 - 94 %).

Figure 3.12 illustrates the feasibility of using *applicator 3* integrated with feedback control for delivering hyperthermia over a 30 min period. During 30 min of heating, hyperthermic zones remained confined to the target while maintaining the safety rate of non-targeted surroundings.

We calculated the safety and coverage metrics over an average of 60 s prior to the timepoints shown in figure 3.12. The safety metric ranged between 77 – 79 %, and the coverage metric ranged between 70 – 90 %. These data illustrate the ability of the proposed system to maintain localized heating to targeted regions over an extended duration of time. While baseline drift is known to be a potential source of error during MRI thermometry for long durations [169], we observed the maximum drift over 60 min to be 0.4 °C; further, this level of drift could be corrected with established drift compensation techniques [188]–[190].

A limitation of this work is the absence of *in vivo* experiments. The dissimilarity between *in vivo* and phantom studies are tissue heterogeneity, blood perfusion, metabolic heat generation and small animal movement inside the MR scanner. Although the optimal system described here was not employed to deliver hyperthermia to small animals, we expect accurate energy *in vivo* delivery according to the temperature profiles of validated 3D *in vivo* computational models. In this study, we applied feedback control relevant to temperatures measured in one transaxial plane, however, temperature was monitored in sagittal plane simultaneously to avoid temperature rise above 8 °C. Coverage and safety rates in sagittal plane were similar to those measured in the transaxial control plane.

## 3.5. Conclusion

We employed a model-based approach for the design and characterization of 2.45 GHz water-cooled microwave applicators for delivering hyperthermia to small-animal targets under 14.1 T MRI guidance. Computational models of microwave heating were experimentally validated and used to comparatively assess the range of applicator parameters that affect thermal profiles, namely: monopole antenna shape and displacement, reflector aperture angle, circulating water temperature, and flow rate. The result of the parametric design process, *applicator 3*, employed a

reflector with aperture angle Θr = 120 °C and an S-shaped monopole displaced 0.6 mm from the antenna's central axis. Adjusting the applied microwave power and circulating water temperature enabled using the selected applicator design to deliver hyperthermic profiles to a range of target ROIs. In experiments using *applicator 3*, a binary feedback control scheme was employed to deliver heating to target ROIs targets 2 - 4 mm in diameter positioned 1 - 3 mm from the applicator surface. In these experiments, 76 - 93 % of the target ROI was heated to the target temperature while 74 - 89 % of non-targeted regions were maintained below the hyperthermic threshold.

# 4. Evaluation of the effect of uterine fibroids on microwave endometrial ablation profiles[3]

## 4.1. Introduction

Thermal ablation is a minimally invasive technique employed for treatment of menorrhagia (i.e. excessive menstrual bleeding) [191]. The objective of the procedure is to thermally coagulate vessels in the endometrial lining of the uterus, while precluding thermal damage to the myometrium and other tissues. Systems employing a variety of energy modalities including radiofrequency [192], laser [193], hot water/steam [194] and cryotherapy [195] are in clinical use for endometrial ablation. Thermal ablation may be delivered to the endometrium in a global or local manner. Local ablation refers to delivering energy to a small localized region, requiring the physician to translate the instrument within the cavity in order to achieve adequate ablation of the entire target [196]. Global endometrial ablation procedures deliver therapeutic energy to the entire endometrium in a single application of energy, without requiring repositioning of the applicator.

Microwave ablation systems have been developed for treatment of tumors in the liver and other organs [197], and are under consideration for treatment of other indications. We have recently presented a system and applicator for global microwave endometrial ablation. The applicator includes a triangular loop antenna that is deployed within the uterine cavity, and delivers microwave energy at 915 MHz.

---

[3] © 2018 IEEE. Reprinted, with permission, from P. Faridi, H. Fallahi, and P. Prakash, "Evaluation of the Effect of Uterine Fibroids on Microwave Endometrial Ablation Profiles," in *2018 40th Annual International Conference of the IEEE Engineering in Medicine and Biology Society (EMBC)*, Jul. 2018, pp. 3236–3239, doi: 10.1109/EMBC.2018.8513051. [42]

The ablation profile of the fabricated applicator was experimentally assessed in *ex vivo* tissues and was found to yield ablation depths within the standard range of 4 -10 mm required for endometrial ablation [198]. While our previous work has established the technical feasibility of delivering microwave energy to the uterine cavity for endometrial ablation, the sensitivity of the treatment outcome to heterogeneity in

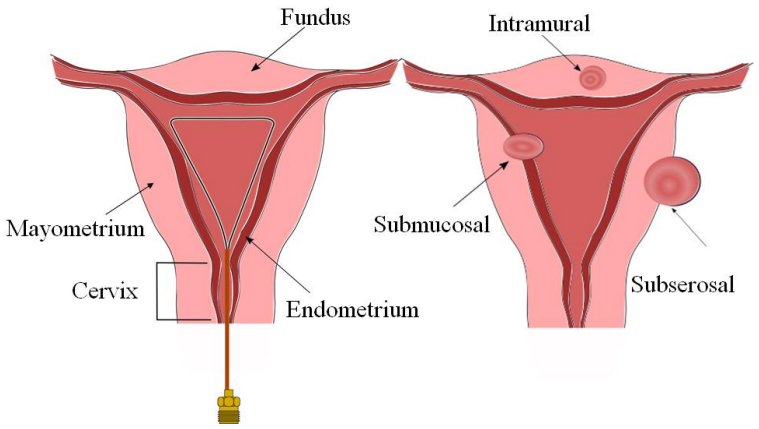


**Figure 4.1** Uterus geometry with single loop applicator in the uterine cavity on the left and 3 different fibroid types on the right

tissue dielectric properties, and non-ideal deployment of the antenna requires further investigation. Computational models of microwave ablation are an established method for assessing the sensitivity of ablation outcome to tissue biophysical properties [199].

Uterine fibroids, abnormal uterine muscle growth, are the most common pelvic tumor in women [200]. Fibroids grow either entirely or partially within the uterine cavity, and may alter the cavity shape. Fibroids are classified relative to their location within the uterus, as follows [201]:

- Submucosal fibroid: drives the endometrium toward the uterine cavity
- Intramural fibroid: grows within the uterine wall
- Subserosal fibroid: moves outward from uterine cavity

Fig. 4.1 illustrates the microwave ablation antenna deployed within a uterine cavity without fibroids, as well as example locations of submucosal, intramural, and subserosal fibroids. Fibroids are further categorized based on their pattern in the uterine wall and cavity. A solitary fibroid is a single fibroid of diameter 1-9 cm, while multiple small fibroids (number ranging from 4 to 20) may exist in proximity to each other, with fibroid being less that 12 cm [202].

As shown in Fig. 4.1, submucosal fibroids may push the endometrium towards the interior of the cavity and have potential to deform the shape of the deployed applicator. The objective of this work is to assess the sensitivity of microwave ablation in the presence of solitary uterine fibroids of diameter in the range of 1 – 3 cm. Since fibroids may have considerably different dielectric properties relative to uterus tissue due to variations in water content and also, as mentioned above, alter the applicator shape, we have assessed the effect of these two parameters, fibroid dielectric properties and applicator geometry change, using an experimentally validated computational model.

## 4.2. Method

We employed computational models of microwave tissue heating to numerically assess the effect of fibroids on the endometrial ablation profile. First, we assessed the validity of the model, by comparing simulated and experimentally measured ablation profiles. Next, we implemented simulations incorporating 1 – 3 cm fibroids in varying simulations, to assess their impact on ablation profiles, compared to those predicted by simulations in the absence of fibroids.

### 4.2.1. Experimental validation of GEA computational models

A 3D numerical model to simulate electromagnetic wave propagation, power deposition, and heat transfer, implemented with COMSOL Multiphysics, was employed for evaluating thermal ablation profiles generated by a 915 MHz loop antenna, previously reported in [198] The antenna

is built from UT-47 coaxial cable, with the outer conductor stripped over a 125 mm length, exposing the insulated inner conductor. The insulated inner conductor is shaped in a triangular loop and is electrically connected to the outer conductor, as illustrated in Fig. 4.2. Details of the computational model are presented in [198]. Briefly, the model solves the Helmholtz electromagnetic wave equation to determine the electric fields radiated into tissue. The model then determines transient temperature profiles using the absorbed electromagnetic power as the heat source. For these 60 W, 150 s ablations, the 60 °C isotherm was used as an estimate of the ablation zone extent.

The computational models were implemented to mimic the configurations employed for experimental evaluation of fabricated prototypes. Since ablation profiles created by the prototypes were assessed in *ex vivo* liver tissue, a widely used tissue model for evaluating thermal therapy devices [203], models used for comparison to experiment simulated ablations in liver tissue. One vertical and three horizontal cut-planes, equivalent to cuts applied to the liver tissue to evaluate the ablation profile in the experiment are considered for comparison to simulated ablation profiles, as illustrated in Fig. 4.2. The maximum difference in the ablation depth of all four cut planes are determined to compare the computational and experimental outcomes.

### 4.2.2. Modeling of uterine fibroids

After comparing experimentally measured and simulated ablation profiles, we adapted the model to include dielectric and thermal properties of uterine tissue. An important step for simulating microwave ablation in the presence of uterine fibroids is to develop suitable dielectric property models. To our knowledge, only a single measurement of fibroid dielectric properties at 100 MHz has been reported in the literature [204]. Since fibroids are an overgrowth of uterine muscle with different water content, we approximated the resultant variation in dielectric

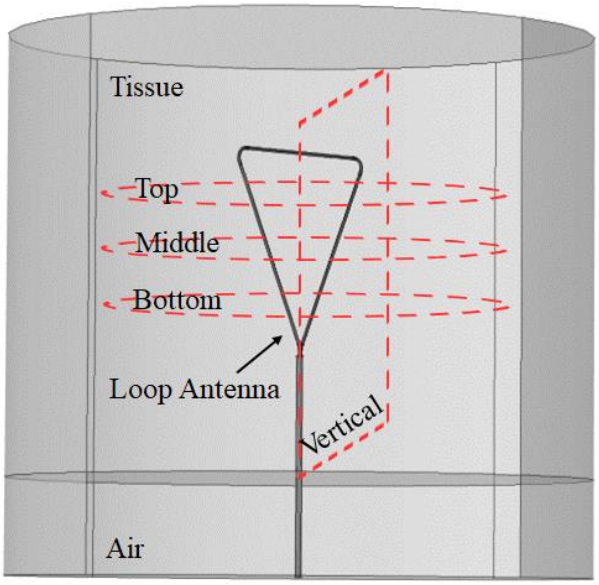


**Figure 4.2** Computational model geometry with 4 cutplanes correspondance to experimental tissue pieces

properties by scaling the dielectric properties with scaling factor *M*, in the range of 0.5 – 1.5 × that of uterine tissue, as illustrated in Table 4.1, to represent increased or decreased water content, as compared to normal uterine tissue [205].

**Table 4.1** Fibroid dielectric properties

| **Multiplication factor (*M*)** | **Tissue dielectric properties** | |
|---|---|---|
| | ***Permittivity, ε*** | ***Conductivity, σ (S/m)*** |
| 0.5 | 30.55 | 0.64 |
| 0.8 | 48.88 | 1.02 |
| 1.2 | 73.32 | 1.54 |
| 1.5 | 91.65 | 1.92 |

Next, we added solitary fibroids of diameter 1 – 3 cm to the left and right side of the uterine wall (myometrium) and the fundal region of uterus. In our models, we incorporated both fibroids that did and did not modify the shape of the deployed applicator. Fig. 4.3 shows four examples of the model geometry with fibroids of different sizes located at various sites. We compared changes

in the antenna's specific absorption rate (SAR) and temperature profiles in the presence of fibroids, to the SAR and temperature profiles, in the absence of fibroids.

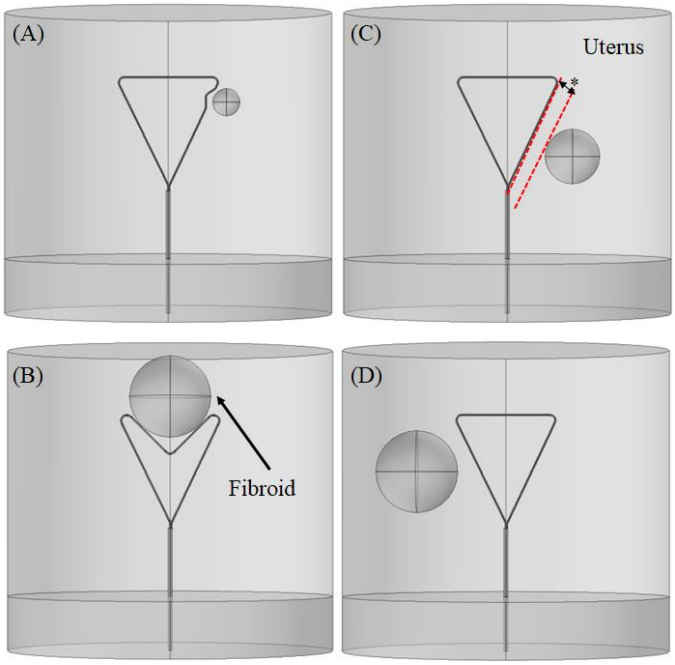


**Figure 4.3** Computational model geometry for (A) and (B) 1 and 3 cm fibroid squeezing the endometrium, (C) and (D) 2 and 3 cm fibroid touching the endometrium, * indicates the 8 mm endometrium gap between the fibroid and applicator

## 4.3. Results and discussions

Fig. 4.4 illustrates simulated and experimentally assessed temperature profiles in *ex vivo* liver tissue. Table 4.2 compares the simulated and measured ablation depth of the four measurement cut planes, as described in [198]. The average and standard deviation of the maximum discrepancy between simulated and experimentally measured ablation depths across the four cut planes was 1 ± 0.8 mm. These data illustrate the suitability of using computational models for estimating extents of ablation zone created by the 915 MHz microwave loop antenna.

Fig. 4.5 shows SAR patterns of the applicator with 60 W input power in the presence of fibroids of varying size and dielectric properties. As seen in Fig 4.5, both variations in dielectric properties and modification of the deployed antenna shape yield a change in SAR pattern.

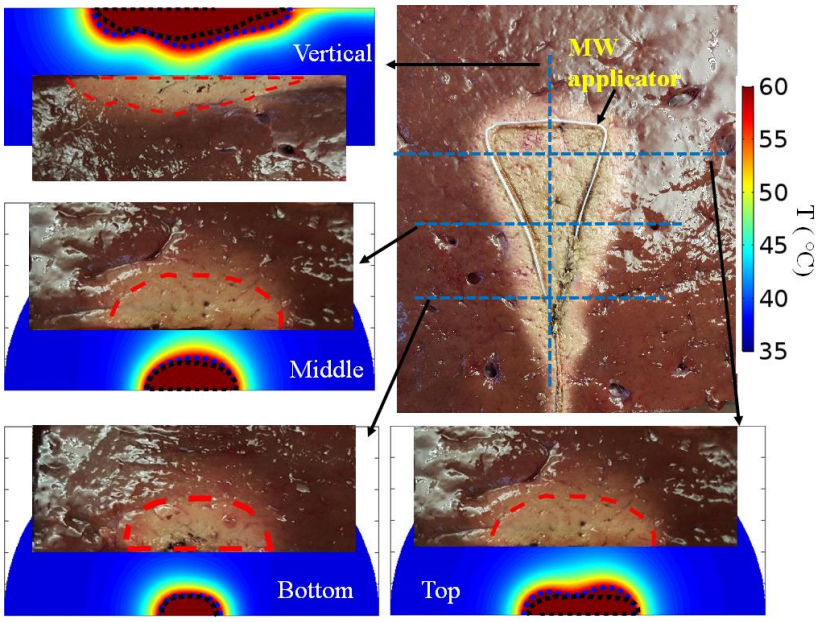


**Figure 4.4** Ablation profiles at time 150 s for *ex-vivo* liver tissue bench-top experiment and compuational modeling with an input power of 60 W on 4 different cut planes, black and blue dashed line on each simulation cut plane indicate a 60 °C contour for experimental and simulated liver tissue, repectively. Red dashed line segments the ablation depth for each cut plane of *ex-vivo* experiment.

Compared to the SAR pattern in a uterus without fibroids, changes in the SAR pattern were more significant for large fibroids that modified the shape of the deployed antenna, than changes due to dielectric heterogeneity between fibroids and background uterine tissue.

Fig. 4.6 illustrates simulated temperature profiles in four cut planes for a 3 cm fibroid in the fundal region, with four different dielectric property. The maximum distance between simulated extents of the ablation zone with and without fibroids, are noted on the illustration in Fig.4.6. Despite the SAR pattern change in Fig. 4.5, ablation depths in the four cut planes remain within the desired range defined for endometrial ablation, and are similar to simulated ablation depths for the case without uterine fibroids. There was little change in ablation depth across the range of dielectric properties of fibroids. Table 4.2 lists the maximum discrepancy in the ablation zone depth for fibroids located on the right or left walls of the uterine cavity. In this table, we have compared the ablation depth changes considering the dielectric change alone, and also, due to

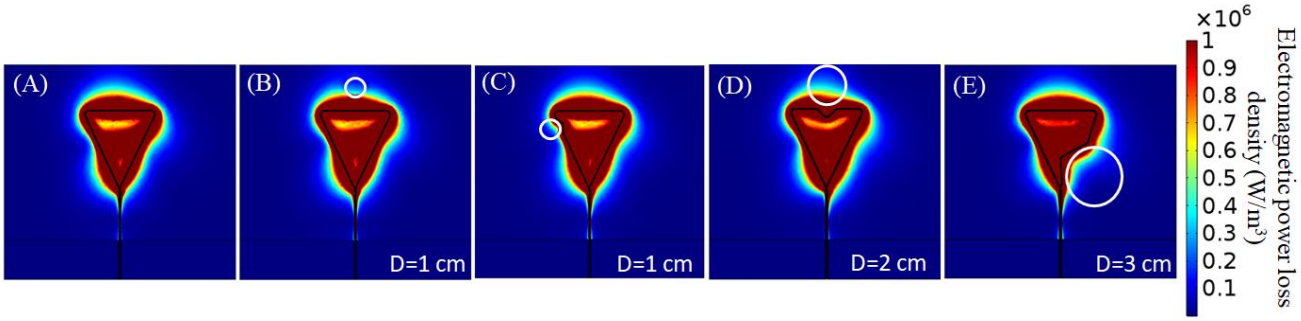


**Figure 4.5** Electromagnetic power depostion through uterine tissue without (A) or with (B-E) fibroid, (B) 1 cm fibroid touching the endometrium in the fundus, (C) 1 cm fibroid squeezing the endometrium on the left uterine wall, (D) 2 cm fibroid in the fundal region pushing the endometrium toward cavity, (E) 3 cm fibroid squeezing the endometrium on the right myometrium, dielectric properties for B-E are determined in Table 4.1 , rows 1-4, respectively.

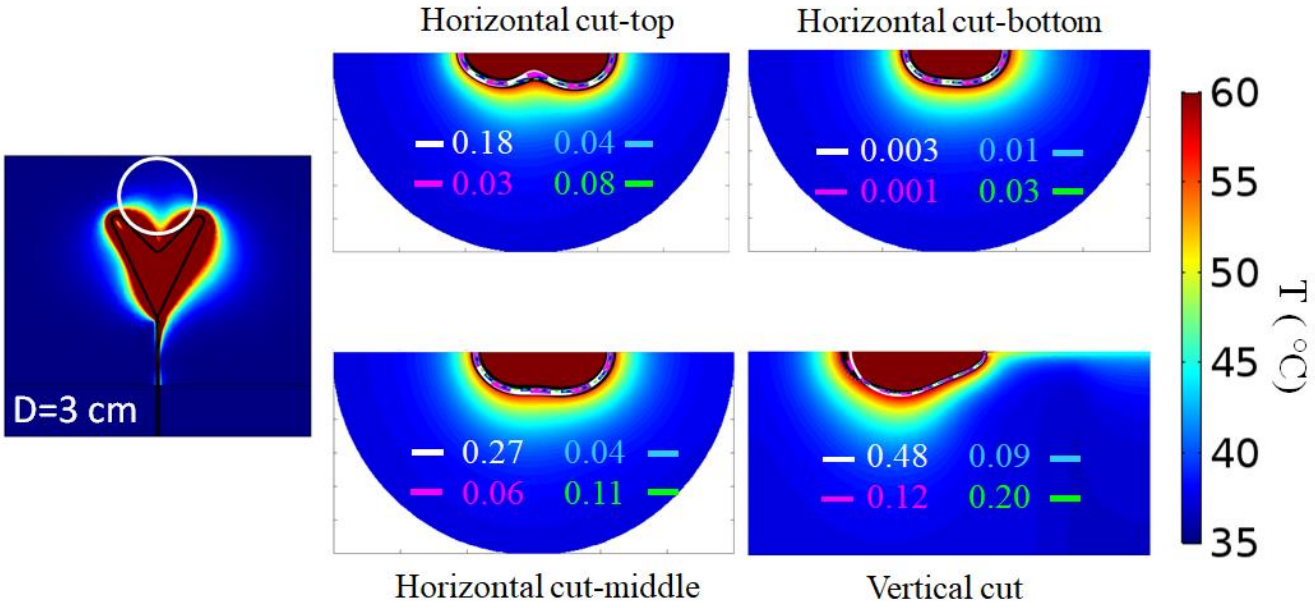


**Figure 4.6** Temperature profiles of 3 horizontal and one vertical cut planes for a SAR pattern generated by fibroid squeezing the endometrium on the fundal region, solid black line and 4 colored dashed lines indicate the 60 °C for plain uterus tissue and uterus with fibroid of 4 distinct dielectric properties. Values indicate the maximum difference (in mm) between uterus without and with fibroids with dielectric properties of Table 4.1.

changes in the applicator geometry. 3 cm diameter fibroids with dielectric properties that are 0.5 and 1.5 × uterus properties yield the greatest discrepancy among all the selection choices of fibroid dielectric properties, sizes and applicator modifications. Table 4.3 indicates that the differences

are in the range of 0.36 ± 0.33 mm.

**Table 4.2** Comparison of computational and experimental ablation depths

| **Absolute discrepancy between experimental [198] and simulated ablation depth [mm] following 150 s heating experiments** | | | | |
|---|---|---|---|---|
| | | | ***Experiment [198]*** | ***Simulation*** |
| Horizontal cut | Top | Left | 5.5 | 7 |
| | | Mid | 6.5 | 6.5 |
| | | Right | 5.5 | 5.3 |
| | Mid | Left | 6.9 | 8.5 |
| | | Mid | 9.5 | 10.3 |
| | | Right | 6.9 | 9.5 |
| | Botto m | Mid | 6.6 | 6.6 |
| Vertical cut | Top | | 6.3 | 7.1 |
| | Mid | | 8.6 | 9.9 |
| | Bottom | | 5.3 | 6.7 |

**Table 4.3** Effect of dielectric properties and applicator geometry on ablation depths

| **Maximum ablation depth [mm] discrepancy for 3 cm fibroid** | | | | | | | | |
|---|---|---|---|---|---|---|---|---|
| | ***ε and σ*** | | | | ***ε, σ and applicator geometry*** | | | |
| ***Site*** / ***M*** | Left myometrium | | | | Right myometrium | | | |
| | Top | Mid | Bot | Ver | Top | Mid | Bot | Ver |
| 0.5 | 0.6 | 1.0 | 0.1 | 1.1 | 0.0 | 0.1 | 0.0 | 0.3 |
| 1.5 | 0.6 | 0.4 | 0.3 | 0.7 | 0.0 | 0.1 | 0.0 | 0.0 |

A limitation of this study is that we did not include the effects of blood perfusion in our models. While we employed a wide range of dielectric properties for fibroids compared to normal uterus, our models did not include any heterogeneity in tissue thermal properties. Although we

have employed uterus tissue properties in the *ex vivo* liver tissue experimentally validated models, uterine tissue was not employed in any of bench top ablation experiments Future studies characterizing the biophysical properties of normal uterine tissue and fibroids are warranted.

## 4.4. Conclusion

We employed computational models to assess the impact of 1 – 3 cm diameter uterine fibroids with dielectric properties in the range of 0.5 – 1.5 × that of uterine tissue on microwave endometrial ablation profiles. Models predicted that the depth of ablation zones in the presence of fibroids were within 0.36 ± 0.33 mm of simulated ablation zones in the absence of fibroids. These findings suggest that 915 MHz loop antennas designed for endometrial ablation may yield similar ablation profiles in patients with and without fibroids.

# 5. Experimental assessment of microwave ablation computational modeling with MR thermometry[4]

## 5.1. Introduction

Computational models of thermal ablation procedures aim to predict the extent of the thermal ablation zone, which is a function of the transient temperature profile within the heated tissue, for a candidate set of treatment delivery parameters. Models of microwave ablation (MWA) are widely used during the design and optimization of ablation applicators, and are also frequently used to characterize applicator performance as part of regulatory submissions [157], [206]–[208]. Models are also used for comparative assessment of energy-delivery strategies [209] and for assessing the impact of various sources of uncertainty on ablation outcome [199], [210]–[213]. Recently, there has been growing interest in the development of computational models for guiding planning of clinical ablation procedures, and for assessing treatment outcome [214]. Experimental validation of MWA computational models is important to provide confidence in model predictions [30], [215]–[218] and may contribute to increased use of modeling tools in the clinical setting. Although the ultimate application of MWA technology is in pathologic tissue in the *in vivo* setting, extensive validation in the controlled *ex vivo* tissue environment represents an important first step for establishing model credibility.

MWA computational modeling consists of 1) defining the geometry of the ablation applicator and the medium (or media) within which the applicator is inserted; 2) assigning biophysical properties to each domain of the simulation geometry; 3) discretizing the computational domain,

[4] © 2020 American Association of Physicists in Medicine, Reprinted with permission, from P. Faridi, P. Keselman, H. Fallahi, and P. Prakash, "Experimental assessment of microwave ablation computational modeling with MR thermometry," *Med. Phys.*, 2020. http://dx.doi.org/10.1002/mp.14318 [44]

and solving the electromagnetic, bioheat transfer, and other equations, subject to the specified initial and boundary conditions. The electromagnetic power density profile serves as the heat source for the bioheat transfer equation [5] . The output of the MWA computational model is transient temperature profile from which thermal damage can be estimated [219]. The model outputs may be affected by several sources of uncertainty and variations (e.g. substantial changes in thermal and biophysical properties due to temperature change [220]).

Validation of a computational model is defined as determining the degree to which the model accurately represents of the physical world given the intended use of the model [221]. Validation of MWA computational models may be performed by comparing model outputs, such as transient temperature profiles and extents of the thermal damage/ ablation zone, with experimental measurements. A widely used approach to assess the validity of MWA models is to place point-based temperature sensors at a few discrete points during experimental ablations, and to compare the measured temperatures with simulated temperature profiles at the same location [5]–[7]. To compare the extent of the ablation zone, simulated thermal damage maps, derived from transient temperature profiles, may be compared with the extent of visibly discolored tissue. This comparison provides an additional level of validation as it accounts for the ablation zone size and shape, in addition to the transient temperature profiles at a few discrete points. However, determining the boundary of the experimental ablation zone (i.e. segmentation) may be subjective prone to inter- and intra-observer bias [222], and challenging with some tissue types, e.g. lung tissue in which ablation zone boundary may be diffuse and not visibly separated from the healthy tissue background [223]. In addition to providing temperature measurements at a large number of points, methods for measuring the transient evolution of spatial temperature profiles during ablation would enable calculation of the extent of the ablation boundary, for example, using the

Arrhenius thermal damage model [219]. In order to provide transient temperature profiles at more than just a few discrete points, infrared cameras have been used to measure spatial temperature profiles during MWA experiments [29]. However, this technique only provides surface temperature measurements and requires experimental apparatus that provides an optical window in the heated tissue, thus making it unsuitable for volumetric temperature measurements during ablation.

Magnetic resonance imaging (MRI) provides a means for spatial measurement of transient temperature profiles in multiple planes. A number of temperature-sensitive MR parameters have been investigated for monitoring of thermal therapy procedures, with the most widely used approach being the proton resonance frequency shift (PRFS) technique [39], [120]. Although tissue dielectric changes may lead to PRFS-measured temperature errors due to phase retardation, it should not significantly affect the temperature measurements when the heated volume is restricted to a small fraction of the imaged sample [224]. While MR thermometry has been widely applied for monitoring and guiding delivery of ultrasound and laser ablation [106], [143], [170], [225], [226], it has not been widely used with microwave ablation systems. Integrating microwave ablation systems with MRI may be challenging due to the need to design the ablation applicators and feeding cables from MRI-conditional materials, as well as considerable attenuation in long feeding cables due to the requirement that the microwave power source is placed outside the scanner room [227]. Some prior studies have investigated the use of 1.5 T MRI thermometry for monitoring microwave heating of *ex vivo* tissues such as brain, muscle, liver, kidney, *in vivo* rabbit brain, as well as ablation of prostate cancer in humans [228]–[230]. In these studies, MR thermometry images were acquired with different imaging sequences such as spoiled gradient-recalled echo (SPGR) and fast-SPGR in a single plane with an update time of ~13 – 26 s. Prior

studies have also employed gradient eco sequences (GRE) with *Z*-shimming for minimizing artifacts in the proximity of metallic microwave ablation applicator [231]. With advances in MR thermometry sequence development, multi-slice thermometry with update times of under 10 s are now available, offering a potential avenue for 3D measurement of transient temperature profiles during ablation procedures [120].

In our earlier study [187], we presented a preliminary assessment of 3D computational models of microwave thermal therapy (over the temperature range 20 °C – 45 °C) in an agar phantom using a 14.1 T ultra-high field small-animal MR scanner. Due to the limited size of the high-field small-animal scanner, the phantom diameter was restricted to 27 mm, and the use of power levels typically used during ablative exposures was precluded. The objective of current study was to develop an experimental MWA platform integrated with 3T MRI and to apply this platform for assessing the thermal profiles predicted by computational thermal models in comparison to thermal profiles measured with Magnetic Resonance Thermometry (MRT). We used a custom 2.45 GHz, water-cooled, microwave applicator for MWA experiments in *ex vivo* tissue performed inside the 3T MRI scanner. A 3D MWA computational model was implemented to predict transient temperature profiles during 30 – 50 W microwave exposure. Volumetric temperature maps and thermal damage profiles measured using MRT were compared to profiles predicted by MWA computational models. To further analyze the sources of uncertainty in measured temperature profiles, we studied the sensitivity of parameters affecting the model output and compared to experimentally measured thermal damage using our developed MWA platform.

## 5.2. Materials and methods

The overall goal of this study was to assess 3D transient temperature and ablation profiles predicted by MWA computational models with temperature profiles measured experimentally

using MRT. Measured transient temperature and ablation zone profiles were compared directly against model predictions. A sensitivity study was conducted to assess the impact of various sources of uncertainty on model outputs, for comparison against variability in experimental measurements.

### 5.2.1. *Ex vivo* tissue MR-guided microwave ablation experimental setup

We developed a custom apparatus for conducting MWA experiments in *ex vivo* tissue within the 3T MRI environment (Fig. 5.1). The MWA system consists of a 200 W, 2.45 GHz solid state generator (SAIREM, GMS 200 W, Neyron, France), peristaltic pump (Masterflex, 07554-90, Vernon Hills, IL), and a custom, water-cooled, microwave applicator fabricated from MR-conditional materials. The microwave generator was connected to power monitoring instrumentation (BirdRF 7022 statistical wideband power sensor, Bird Technologies, Solon, OH) to keep track of power delivered to the applicator. The generator, power monitoring instrumentation, and peristaltic pump were placed outside the MRI room in the controller room. The water-cooling lines and the fiber-optic temperature probe extensions were introduced into the scanner room via a waveguide. The microwave signal was coupled to the MWA applicator inside the MRI room via a penetration panel. The coaxial cable and water line tubing between the generator, pump and the applicator were 6 m long (5 m from microwave applicator to waveguide and 1 m from waveguide to the generator). This length of cables in between the microwave generator and the MWA applicator placed limits on maximum power applied at the MWA applicator connector. Considering the attenuation level of cables, with a generator of maximum 200 W, the maximum power at the applicator input port was limited to 52 W.

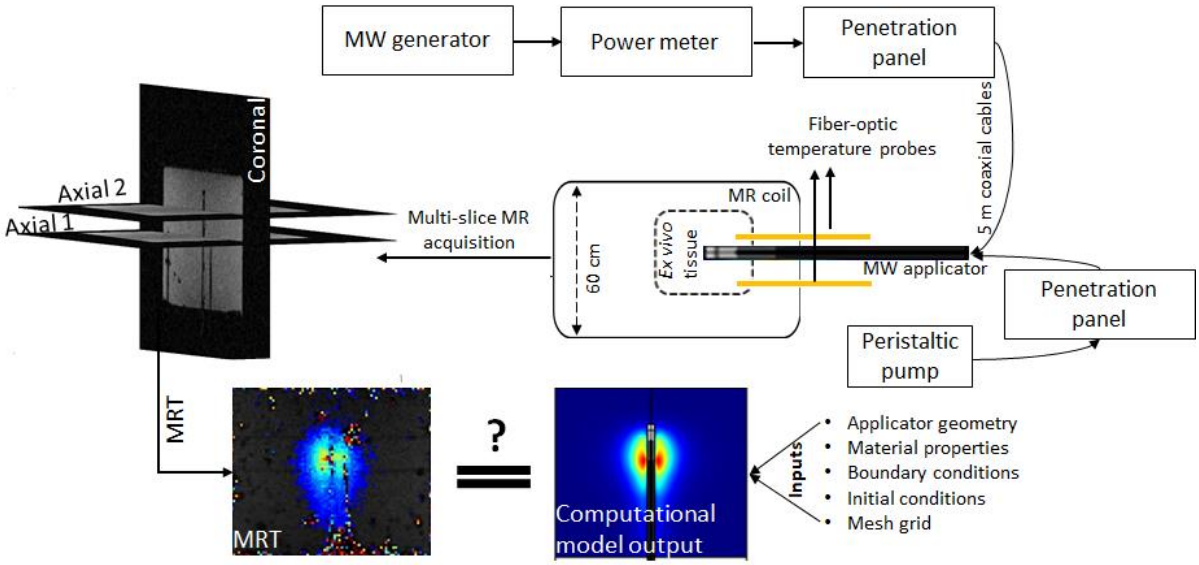


**Figure 5.1** Block diagram of the microwave ablation system integrated with 3T MRI

We performed MWA in *ex vivo* tissue (bovine liver) under 3T MRT guidance using a custom, 2.45 GHz cylindrically-symmetric water-cooled applicator. As illustrated in Fig. 5.2, the ablation applicator consists of a monopole antenna created by modifying the distal tip of a low-loss, coaxial cable with a non-magnetic copper jacket (UT-047C-LL; Microstock, Inc, PA, USA) to expose the center conductor. The antenna is concentrically positioned within a water in-flow tube (FEP, O.D. = 2 mm; I.D. = 1.4 mm) and an outer tube (PEEK, O.D. = 2.54 mm, I.D. = 2.4 mm) that provides a return flow path. Water flow around the distal tip of the radiating antenna, was employed to remove waste heating along the applicator's shaft due to attenuation within the coaxial cable, as well as to provide a high dielectric constant material that yields a short electromagnetic wavelength.

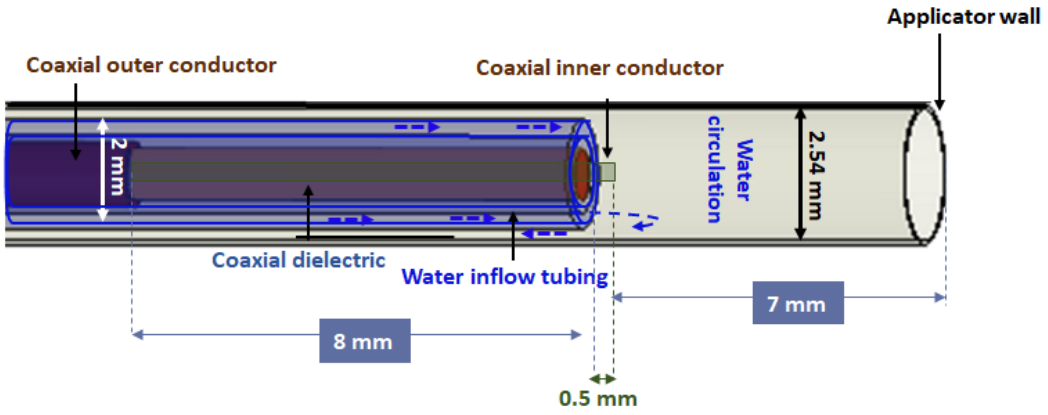


**Figure. 5.2** Geometry of the distal tip of the microwave ablation applicator

MR thermometry data were acquired on a 3T Siemens Skyra scanner using a vendor provided 15-channel Tx/Rx knee coil in one coronal (parallel to microwave ablation applicator) and two axial planes (perpendicular to coronal view). One axial plane was aligned with the distal point of fiber-optic temperature probes while the second one was placed 13 mm apart distally, to capture thermometry data in a plane near the tip of the radiating antenna element as illustrated in Fig. 5.1. Phase and magnitude maps were reconstructed from a series of fast low-angle shot (FLASH) images (TR/TE = 50/12.3 ms, FOV = 128 x 128 $mm^2$, matrix = 128 x 128, flip angle = 15°, slice thickness = 1.5 mm and acquisition time = 6.4 s per image) to measure changes in tissue temperature. The PRFS method, a widely used MR temperature monitoring technique, was utilized in this work to measure temperature changes during microwave heating [39], [120]. In this work, a fast spoiled GRE sequence (FLASH) was used due to its relatively short TE/TR, which decreases the scanning time that is appropriate for temperature monitoring and high accuracy in temperature monitoring spatially and temporally while maintaining a relatively high SNR [143].

To compensate for the magnetic field drift of MRT at 3T, we applied the phase drift correction [230] to our measurements as follows:

$$\Delta T = \frac{\Delta\phi(t) - \Delta\phi_{drift}(t)}{\alpha\gamma B_0 TE}, \begin{cases} \Delta\phi(t) = \phi(t) - \phi(0) \\ \Delta\phi_{drift}(t) = \phi_{drift}(t) - \phi_{drift}(0) \end{cases} \quad (12)$$

where $\alpha, \gamma, B_0$ and $TE$ are the PRF temperature coefficient, gyromagnetic ratio, the magnetic field and echo time defined in the MR scanning sequence, respectively. In the above equation, $\Delta\phi(t)$ is the phase change due to both temperature and other changes and $\phi_{drift}(t)$ is a 3×3 region of interest (ROI) selected far away from the applicator where no temperature change was expected. The first phase image during course of experiment was considered as the reference image, $\phi_{drift}(0)$, which was subtracted from the all other images to capture the non-temperature phase changes.

A total of 13 ablation experiments were conducted using 30 – 50 W applied power at the applicator input (corresponding to 100 – 180 W power level at the generator). MRT data were acquired for 2 min prior to heating, during 5-10 min microwave exposures, and for 3 min following heating. The MWA applicator was inserted 5 cm deep inside the tissue. Two fiber-optic temperature probes were introduced during ablation experiments to compare the monitored temperatures to MRT measurements ($FO_1$ at 5 mm and $FO_2$ at 35 mm radially from the applicator). The fiber-optic temperature probes were placed at pre-defined depths in regions where peak ($FO_1$) and moderate ($FO_2$) temperatures were anticipated. $FO_1$ was axially aligned to be in proximity to the junction of the coaxial outer and inner conductors. Initial tissue temperature was also monitored by $FO_1$ and $FO_2$, which later was used as a baseline temperature for MRT measurements to determine absolute temperature of tissue during ablation experiments. We used a 8×8×8 $cm^3$, 1 cm thick custom-made 3D printed container (polylatic acid, PLA, filament) to hold the same volume of *ex vivo* tissue for each experiment. The container's lid (1.5 cm thickness) had 3 holes to align the fiber-optic temperature probes with the microwave applicator at 5 mm and 35 mm radial distance from the applicator. This fixture was designed to produce repeatable experiment outcomes.

### 5.2.2. Microwave ablation computational modeling

We implemented MWA computational models using the finite element method with COMSOL Multiphysics (v 5.4) software. These models utilize time-harmonic wave propagation equation to calculate the electromagnetic power absorption profile in tissue. The electromagnetic model is coupled with the transient heat transfer equation to calculate 3D temperature profiles. Similar to state-of-art MWA computational models [199], [209], changes in tissue physical properties as a function of temperature change were incorporated within our model. Similar to prior modeling studies of water-cooled microwave ablation applicators [213], [232], we employed a convective heat transfer boundary condition assuming a constant cooling temperature for the circulating water flowing inside the applicator (during ablation experiments, a 1 °C change in circulating water was measured, see Fig. A.S.1 in the Appendix A). Since this study only considered experiments in *ex vivo* tissue, no perfusion term was included. Fig. 5.3 illustrates the various components of the computational model, including specification of boundary conditions, and how the electromagnetic and thermal model are coupled. Further details of the computational model were previously described in [157].

Similar to existing computational models of MWA [199], we incorporated temperature-dependent changes in tissue physical and thermal properties in our models.

Table 5.1 lists the equations for temperature dependent tissue properties which were used in the computational models in this work, similar to [199]. Briefly, the dielectric properties are represented with a sigmoidal temperature dependency, where both relative permittivity and effective conductivity transition from relatively high values at low temperatures to relatively low values at temperatures in excess of ~100 °C (attributed to desiccation) [210], [211]. The volumetric heat capacity incorporates the effects of latent heat of water vaporization at temperatures close to

**Table 5.1.** Temperature dependent tissue properties for microwave ablation computational model

| *Temperature dependent tissue properties* | *Equation used in the coupled computational model of microwave ablation* |
|---|---|
| $\sigma_{ef}(T)$ | $\sigma_{ef}.\left(1-\frac{1}{1+\exp\left(0.0697.\left(85.375+\Delta_{el}-T\right)\right)}\right)$ |
| $\epsilon_r(T)$ | $\epsilon_r.\left(1-\frac{1}{1+\exp\left(0.0764.\left(82.271+\Delta_{el}-T\right)\right)}\right)$ |
| *Pc (T)* | $\begin{cases} \rho c_0 & for \quad T<(100-\frac{\Delta T}{2}) \\ \frac{\rho c_0+\rho c_v}{2}+\frac{\rho_\omega.L.C}{\Delta T} & for \quad \left(100-\frac{\Delta T}{2}\right)<T<(100+\frac{\Delta T}{2}) \\ \rho c_v & for \quad T>(100+\frac{\Delta T}{2}) \end{cases}$ |
| *k (T)* | $\begin{cases} k_0+\Delta k\times(T-37) & for \quad T<100\,°C \\ k_0+\Delta k\times(100-37) & for \quad T>100\,°C \end{cases}$ |

100 °C [233]. Thermal conductivity is represented with a linear increase with increasing temperature, as reported in [234]. A non-uniform tetrahedral mesh grid was applied through the geometry such that the finest mesh was applied at the applicator input port boundry (maximum element edge length = 0.05 mm), with increasing element size at distant regions, with the largest mesh elements within the tissue domain (maximum element edge length = 3 mm).

The Arrhenius thermal damage model is a well-established model for assessing thermal damage following non-isothermal heating, and was used in this study to compare model-predicted thermal ablation zones with experimental measurement (Equation 14):

$$\Omega(\mathrm{T}) = \int_{t=0}^{\tau} A e^{-\frac{E_a}{R(T(t)+273.15)}} dt \tag{13}$$

In the above equation, the frequency factor ($A = 5.51\times10^{41}\ s^{-1}$) and energy barrier ($E_a = 2.769\times10^{5}\ J.mol^{-1}$), were selected for pig liver tissue whitening [219]. R is gas constant (8.3145 J $mol^{-1}\ k^{-1}$) and T(*t*) is the temperature (°C) at time *t*. A binary thermal damage map, showing the

extent of ablated area, was calculated using $I = \Omega(T) > 1$, which corresponds to 63% of the thermal damage process being completed.

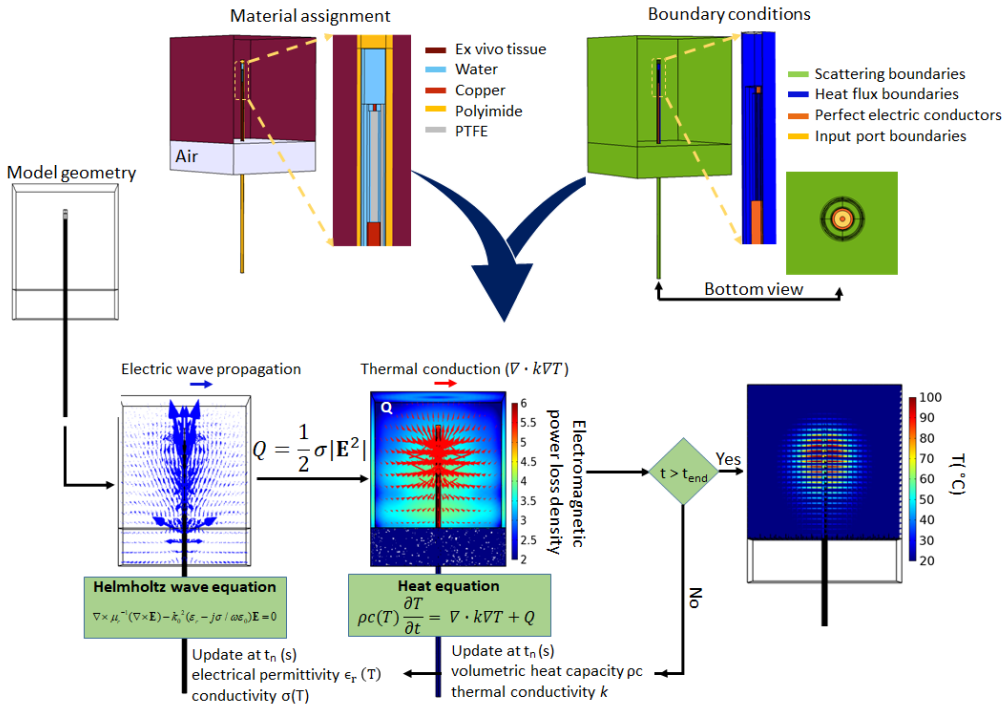


**Figure. 5.3** Schematic of the 3D microwave computational model

### 5.2.3. Experimental assessment of microwave ablation computational models

We compared 3D transient temperature profiles predicted by computational models with temperature profiles measured using MRT. To consider volumetric temporal and spatial distribution of temperature, we made the following comparisons between simulated and measured temperature profiles:

a) Transient temperature in multiple 3×3 ROIs in coronal and axial planes

b) Radial distribution of temperature at different time-points in the duration of experiments at multiple locations along the axis of the MWA applicator.

The mean absolute error (MAE %) between MRT and simulated temperature ($T_{MRT}$ and $T_{simulated}$ in equation 3, respectively) is reported for the above comparisons (a and b), as a percentage

of the maximum temperature change observed during experimental ablations. Equation 3 is used to measure MAE %:

$$MAE\ \% = \frac{avg|T_{MRT} - T_{simulated}|}{Max(T_{MRT})} \times 100 \quad (14)$$

MAE % is an established measure of difference between simulations and measurements relative to the largest measured value [213].

a) Extents of the ablation zone, using binary Arrhenius thermal damage maps. To compare simulated and MR-derived binary Arrhenius map, Dice similarity coefficient (DSC) is used (Equation 4, in which *I* is binary Arrhenius map).

$$DSC = \frac{2|I_{\text{measured}} \cap I_{\text{simulated}}|}{I_{\text{measured}} + I_{\text{simulated}}} \quad (15)$$

### 5.2.4. Sensitivity analysis

Tissue biophysical properties are known to vary considerably across patients, as well as a function of tissue pathological state. Prior studies of tissue dielectric and thermal properties made on *ex vivo* tissue have also demonstrated variability in these properties across samples [220]. The inter-sample variability of tissue dielectric and thermal properties may affect the experimental outcome. Similar to previous studies on sensitivity analysis of thermal ablation [199], [235], we used the Morris method to determine the sensitivty of microwave ablation zones to uncertainty in tissue physical properties. The seven variables considered for this sensitivity study and their range of tissue physical properties are defined and shown in Table 5.2. The equations describing the temperature dependence of the dielectric and thermal parameters is provided in Table 5.1. In this work, we have considered 30 starting points for the variables with significant influence on the ablation zone shape according to sensitivity study in (i.e. a total of 210 simulations).

**Table 5.2.** Range of values for tissue physical properties used in the sensitivity study

| *Sensitivity parameters* | *Definition* | *Range* | *Units* |
|---|---|---|---|
| $\varepsilon_r$ | Relative permittivity | 30.73 - 68.8 | - |
| $\sigma_{ef}$ | Effective conductivity | 1.14 – 2.55 | S/m |
| $\Delta_{el}$ | Temperature transition in sigmoid function (Temperature at which state of sigmoid function changes from high to low) | -15 to 15 | °C |
| $\rho c_0$ | Basline volumetric heat capacity | (3.7 – 4.3). $10^6$ | J/(°C.m$^3$) |
| $\Delta T$ | Temperature interval across which the tissue changes phase | 1 – 10 | °C |
| $k_0$ | Thermal conductivity | 0.46 – 0.57 | W/(°C.m) |
| $\Delta k$ | Thermal conductivity change with temperature | 0 – 0.0033 | W/(°C.m) |

## 5.3. Results

### 5.3.1. MRT validity assessment

MRT measurements were compared against fiber-optic temperature data for a wide range of temperatures, with a maximum temperature rise of 100 °C monitored with $FO_1$ at 5 mm radially from the ablation applicator. Prior to heating, the observed standard deviation of MRT data was in the range of 0.3- 0.7 °C, which provides an indication of the uncertainty in our MRT measurements. Fig. 5.4 shows exemplar transient temperature profiles prior to, during and post MWA measured with MRT and $FO_1$ and $FO_2$. Mean absolute error (MAE) between MRT and $FO_1$ and $FO_2$ during heating across 13 *ex vivo* tissue MWA experiments was in the range of 1 – 2.8 °C and 0.5 – 1.4 °C, respectively.

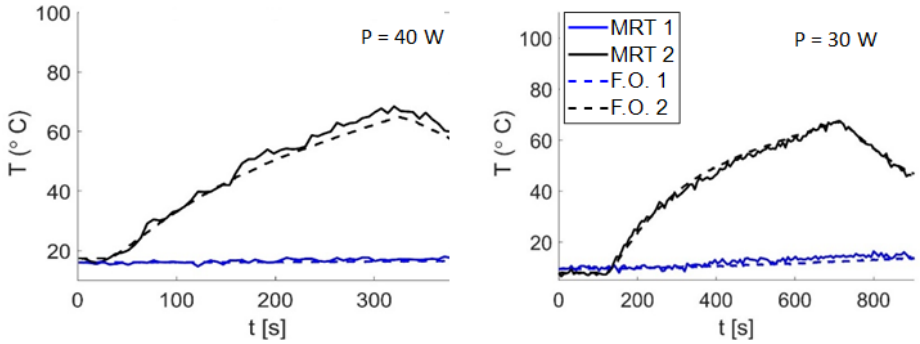

**Figure. 5.4** Experimental transient temperature measurments with fiber-optic temperature sensors in comparison to MRT at ROIs located at the tip of fiber-optic temperature probes in 5 mm (black lines) and 30 mm (blue lines) distance from the applicator with input power of 30 and 40 W.

### 5.3.2. Experimental assessment of computational models

Fig. 5.5 shows MRT measurements from four different experiments (labeled MRT 1- MRT 4) during microwave ablation of *ex vivo* tissue compared to simulated temperatures in multiple 3×3 ROIs in axial and coronal views. ROIs in proximity to the applicator were selected to include high temperatures and locations that dielectric and thermal properties of tissue were expected to change substantially during the ablation experiment. Conversely, ROIs further away from the applicator were also selected to include regions of lower temperatures. The MAE %, as a percentage of overall temperature rise, between experimentally measured and simulated temperatures was calculated for each of the transient temperature profiles shown in Fig. 5.5, which ranges between 1.2 % and 11 % with an average of 5.91 ± 1.1 %.

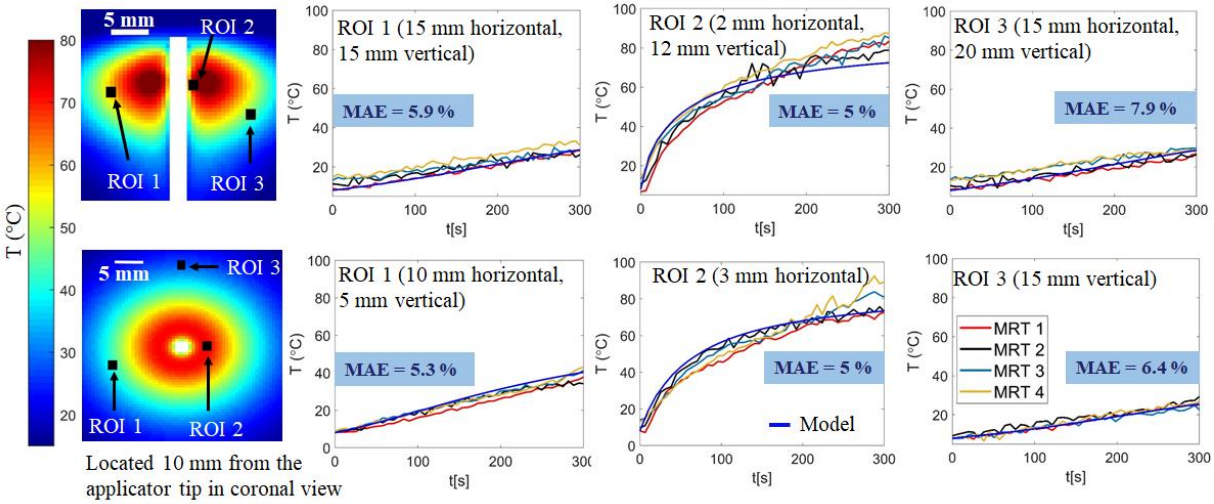


**Figure. 5.5** Experimentally measured and simulated transient temperature profiles at multiple ROIs in coronal (first row) and axial views (second row) for input power P = 30 W. MAE % reports the average percentage of mean absolute error between MRT1, MRT2, MRT3, MRT4 and model.

We further compared MR-measured and simulated temperatures radially at different time-points during the MWA experiments at multiple regions of tissue relative to the applicator distal point (Fig. 5.6). The MAE % between radial temperatures measured using MRI map and predicted

by 3D model is calculated. The MAE % shown on each of the temperature profiles in Fig. 5.6, is the mean of the MAE % between each of the MRTs and the model-predicted temperature profile.

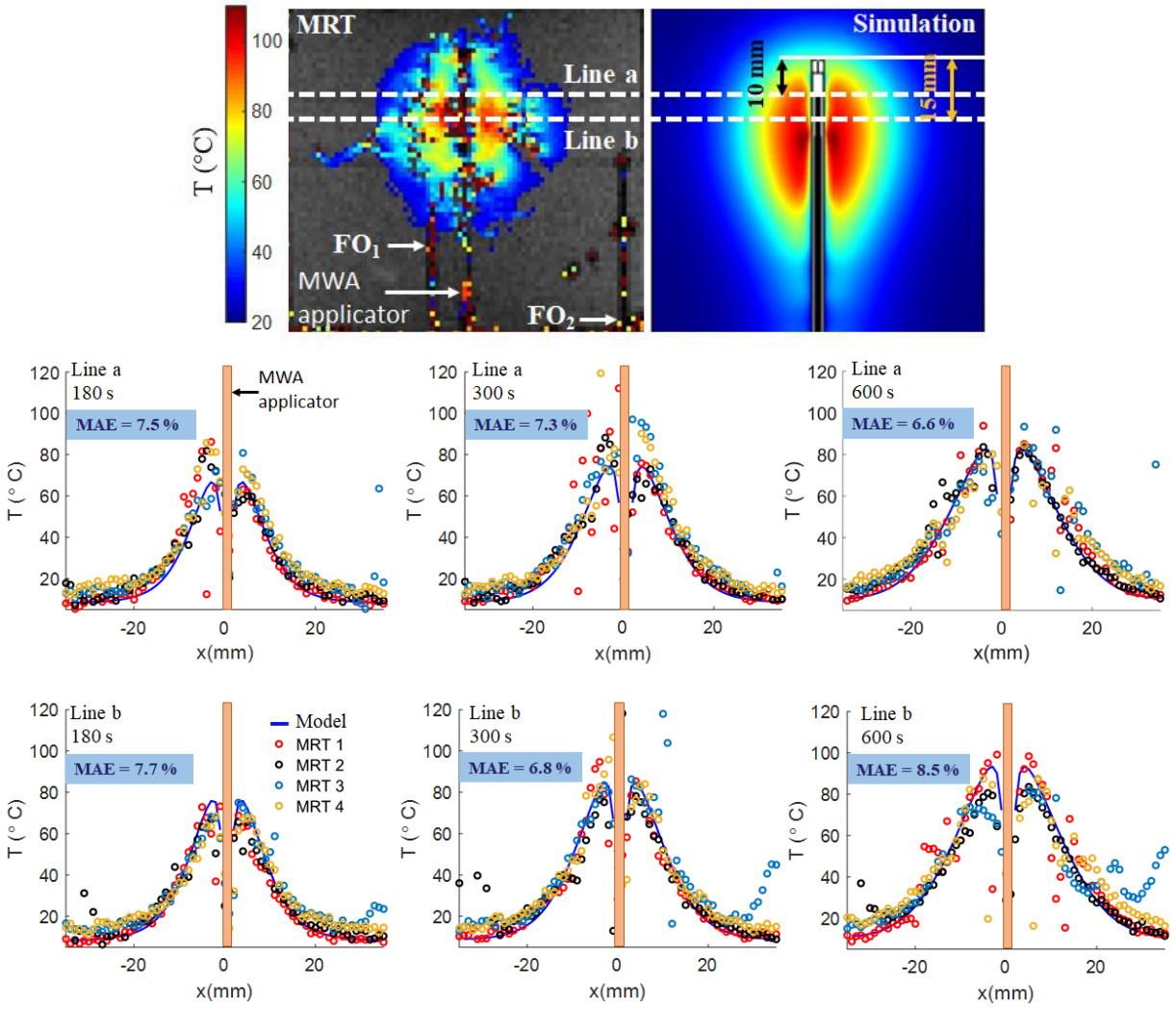


**Figure. 5.6** Experimentally measured and simulated radial temperature profiles located at 10 mm and 15 mm from the applicator tip at t = 180, 300 and 600 s followed by input power of 30 W. MAE % represents the mean absolute error as a percentage of maximum temperature between MRT1, MRT2, MRT3, MRT4 and simulations.

We also compared model-predicted ablation zone extents against MRT-derived Arrhenius thermal damage maps in 3D view. In Fig. 5.7, three examples of Arrhenius thermal damage maps with different combinations of power and ablation duration are illustrated. The DSC between model-predicted ablation zones and MRT derived Arrhenius thermal damage maps were 0.8 ± 0.0 (30 W, 10 min, *n*=4), 0.8 ± 0.08 (30 W, 5 min, *n*=8) and 0.75 ± 0.06 (50 W, 5 min, *n*=3).

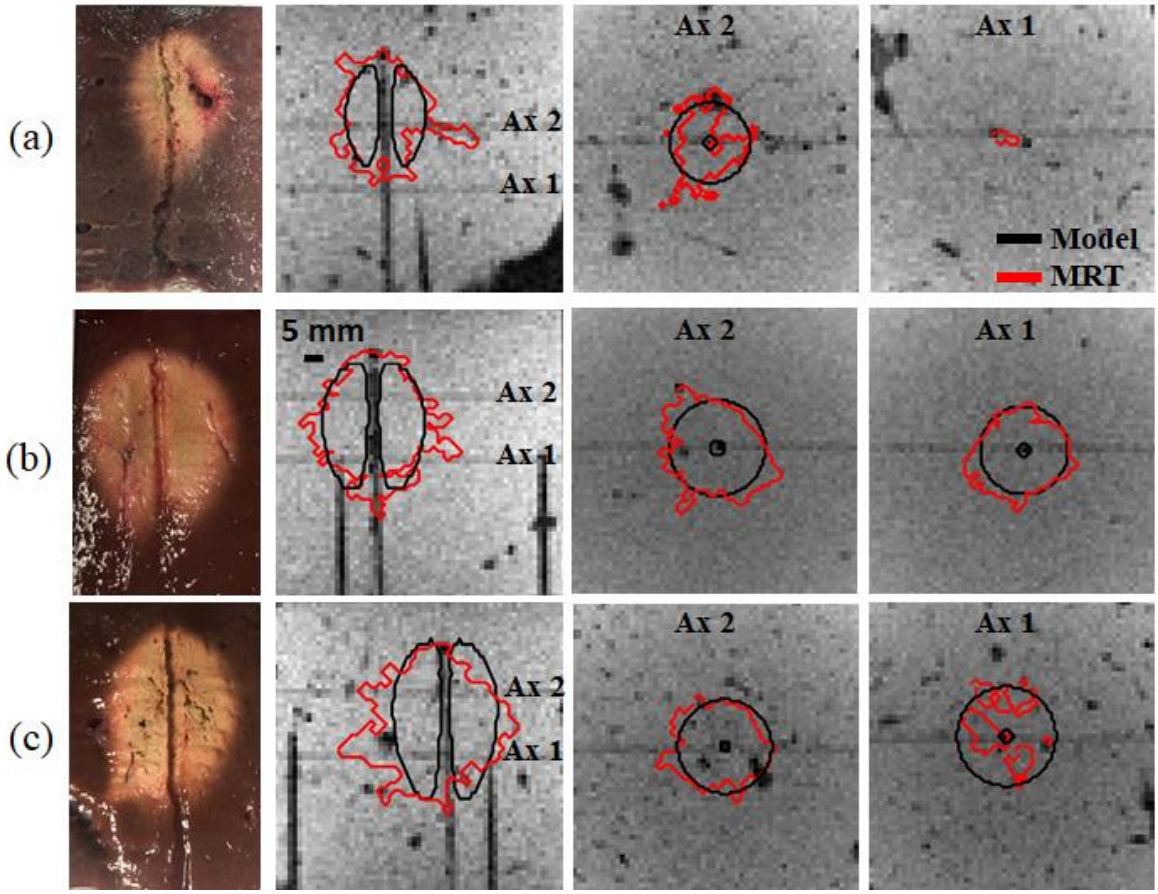


**Figure. 5.7** Thermal damage boundaries of MRT measured, coupled and uncoupled simulated arrhenuis map superimposed on the magnitude image collected a) with input power of 30 W after 300 s, b) with input power of 30 W after 600 s and c) with input power of 50 W followed by 300 s of ablation.

Fig. 5.8 depicts the variation of MRT-derived Arrhenius thermal damage maps across *ex vivo* tissue experiments. We have averaged the binary thermal damage maps computed from MRT measurements during *ex vivo* tissue MWA experiments for each particular power and time combination. This illustration provides an assessment of the variability of ablation outcome across multiple experiments. Regions which were ablated in all experiments yielded an average value of 1, while regions not ablated in any of the experiments yielded an average value of 0. Regions where the average value was between 0 and 1 were ablated in a subset of experiments. A single model-predicted thermal damage contour, using the average value of tissue physical properties, is superimposed on the averaged thermal damage map. As shown in Fig. 5.8, the simulated thermal

damage contour is in alignment with the ablated region that is in common among all *ex vivo* tissue MWA experiments (white regions in Fig. 5.8).

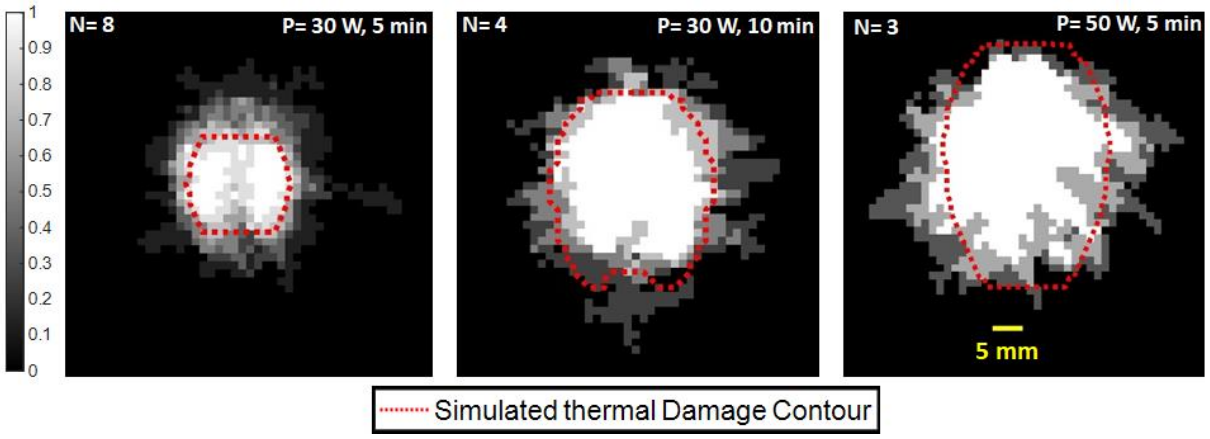


**Figure. 5.8** Experimentally measured Arrhenuis thermal damage maps averaged across multiple experiments, superimposed on the simulated arrhenuis map; white regions indicate ablation zones in common between all MRT-derived Arrhenuis thermal damage map, gray regions are areas ablated in a subset of experiments, and black regions are non-ablated tissues across all experiments.

The sensitivity of simulated experimental profiles to uncertain tissue dielectric and thermal properties and their temperature dependecies, is illustrated in Fig. 5.9. The data are presented as the average of the binary ablation maps across multiple experiments. Also illustrated are 20%, 50%, and 100% contours from both simulations and experiments, which provide an interpretation of the likelihood of ablation for a given location.

## 5.4. Discussion

Validation of MWA computational models would contribute to applying models to their full potential for ablation device design and characterization, comparative assessment of energy delivery strategies, and patient-specific pre-treatment planning. The objective of this work was to integrate a MWA system with 3T MRI, and to use the volumetric MR thermometry as a means for validating computational models. The MR-guided MWA platform that we developed offered 3D temperature measurements during ablation experiments in *ex vivo* tissue, facilitating comparison

against simulated temperatures in both axial and coronal planes. The present study considered an MWA applicator with a cylindrically symmetric pattern,

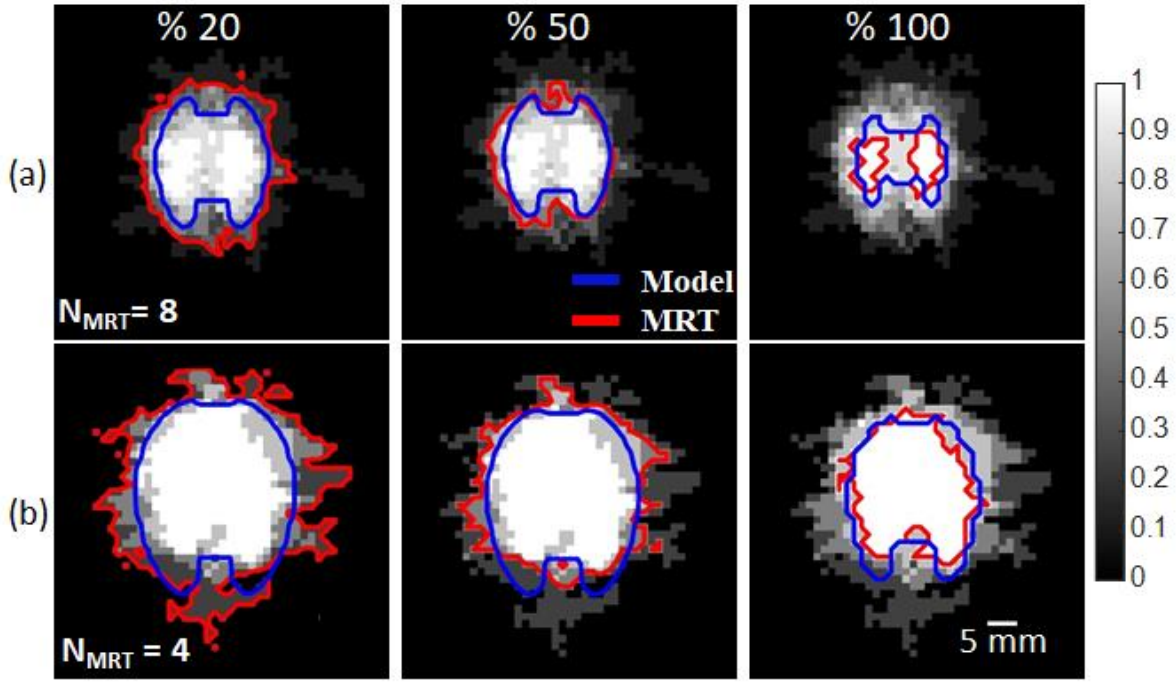


**Figure. 5.9** Probability of tissue being ablated in experimentally measured and simulated Arrhenuis thermal damage map with P = 30 W followed by (a) 5 min and (b) 10 min ablation duration. 210 simulations and $N_{MRT}$ number of MR-guided experiments were used to calculate the probability map.

similar to applicators in current clinical use, inserted within a homogenous medium. If evaluating thermal ablation profiles within more heterogeneous media, as in the clinical context, or when considering emerging MWA applicators with directional control of radiation [236], measurement of the 3D temperature profiles and ablation patterns enabled by the presented technique would offer considerably more detailed characterization of ablation profiles in contrast to the widely-used point-based temperature measurement which enables model assessment at only a few discrete points [213]. Evaluating the performance of computational models by insertion of few temperature probes not only monitors temperature in just few points at the location of temperature probes but it presents source of variability due to the inherent uncertainty in accurately localizing the temperature probe position relative to the ablation applicator.

Similar to several other prior studies [228]–[230], we employed fast spoiled GRE sequence (FLASH on Siemens scanners and SPGR on GE scanners) as the thermometry sequence. This sequence was selected as it has previously been validated for MR thermometry monitoring of ablation, although it is noted that several other thermometry sequences are available for monitoring tissue ablation, as reviewed in [120]. Since MRT measurements are known to be sensitive to B0 magnetic field inhomogeneity, which can be affected by the insertion of MWA applicator, we measured temperature changes in an agar phantom within regions of interest in proximity to the MWA applicator (5 mm) and distant (27 mm) from the applicator. Without any applied microwave power (i.e. no heating), standard deviation of MRT data over time at 5 mm was in the range of 0.38 – 0.47 °C, while the standard deviation of MRT data over time at 27 mm was in the range 0.37 – 0.41 °C. These results indicate that introducing our applicator into the tissue did not have a significant impact on the uncertainty of MRT data (see Fig. A.S.2 in the Appendix A). While prior studies [231] noted considerable impact of artifacts in proximity to metallic ablation probes, limited artifact may have been observed in the present study since the water-cooled ablation applicator does not have any metallic components in direct contact with tissue; rather, the antenna is surrounded by circulating water that is enclosed by plastic tubes.

Temperature profiles measured by MRT were used to comparatively assess the validity of the MWA computational model (Fig. 5.5 and Fig. 5.6). The mean absolute error (MAE %), expressed as a percentage of maximum change in temperature, of MRT measured and model predicted temperatures at different ROIs was 5.91 ± 1.1 %. Radial temperature profiles at multiple time-points during the experiment and different locations relative to the distal point of the applicator were then compared. As a result of this comparison, the average of MAE % was 7.4 ± 0.7. These data indicate that although discrepancies between model predicted and experimentally

measured temperatures can be quite large, in regions at the periphery of the ablation zone, simulated and measured temperatures are generally well aligned. We note that the presence of the MWA applicator may cause an artifact in the anatomical (i.e. magnitude) images acquired by FLASH sequence [237]. This may decrease the accuracy of locating the MWA applicator tip, which was used as a reference for temperature comparison between experimental and simulated temperatures. This may also be a source of discrepancy between MR-measured and simulated temperatures at different ROIs or radially measured temperatures especially in the proximity of the applicator (Fig. 5.5 and 5.6). We also anticipate the asymmetric water inflow inside the applicator as another potential source of discrepancy. While fabricating the microwave applicator, we attempted to center the inner conductor in the water inflow tube, however, it may have been slightly shifted toward one side of the water inlet tubing. In this case, the cooling effect would be higher on one side of the applicator relative to the other side while the cooling effect remains symmetric within the computational model. In Fig. 5.6, the discrepancy in the temperature measurements that are distances further from the applicator are primarily in regions with blood vessels, that are filled with air in this *ex vivo* tissue model.

A widely used approach for validation of MWA computational models is to compare experimental measurements of the extent of visible tissue discoloration, with simulated ablation zone, either using a thermal damage model, or with a temperature isotherm [10]. Another widely used approach is to compare transient temperatures at select discrete points with model predictions at corresponding locations [209]–[211]. Volumetric assessment, with MRT, enables both spatial and temporal comparison of temperature profiles and ablation zone size and shape (Fig. 5.7 and Fig. 5.8). It's noteworthy that in a few experiments, high power microwave exposure, $P > 40$ W ($n = 4$) or long duration of ablation exposure, $t = 600$ s ($n = 2$) were associated with extensive

water vaporization in proximity to the applicator, which corrupted MRT data in these regions. The discontinuity in the thermal damage profile of the transaxial views of Fig. 5.7 (c) is a result of this incident. Due to this limitation, conventional MRT measurements may not be an appropriate technique for monitoring tissue temperatures reaching elevated temperatures in excess of 100 °C, as are commonly observed during MWA. In spite of this limitation, the ability of MRT to provide volumetric assessment of ablation profiles, as well as accurately capture transient temperature profiles in regions below 100 °C, offers considerable added information over probe-based thermometry techniques.

We found the area of regions ablated in all experiments was 283 $mm^2$, and the area of regions ablated in only one experiment was 411 $mm^2$ (Figs. 5.8 and 5.9). In contrast, the corresponding areas of these regions in simulations were 327 $mm^2$ and 395 $mm^2$, respectively, after conducting 210 simulations using the Morris method. The relatively smaller difference between these areas in simulation suggests that, for the power levels and ablation durations considered in this study, the ablation zone is relatively insensitive to variability in tissue physical properties. This may be attributed to the applicator design, where the antenna is surrounded by a relatively static, high dielectric constant medium, achieved by circulating chilled water through the applicator up to the distal radiating tip. Prior sensitivity studies of MWA [199], [238] suggested larger variations due to uncertainty in tissue properties, but the antennas considered in those studies did not have water circulated to the radiating tip. The relatively larger variations observed in experiments may be due to additional sources of uncertainty not accounted for within simulations. These include variations in MRT slice localization relative to the applicator across various simulations and ablation zones affected by steam transport within vessels during these *ex vivo* tissue experiments. Nevertheless, the 100% contours from experiments and simulations were 283

$mm^2$ and 327 $mm^2$ and, the 50% contours from experiments and simulations were 503 $mm^2$ and 406 $mm^2$, respectively, indicating the model's ability to represent the ablation zone profiles observed experimentally.

This study had several limitations. During MWA, the center of ablation region in the proximity of applicator loses water first and the water is driven outwards, evaporates and may recondense in cooler regions away from the applicator [209], [239]. This effect was not incorporated in the 3D computational model we used for the assessment. Furthermore, changes in tissue physical properties at elevated temperatures (Table 5.1) were modeled as functions of temperature alone, based on the currently available models in the literature. However, it is plausible that tissue properties may also be a function of rate of heating, in addition to temperature. The impact of rate of heating and tissue water transport may be of most significance in proximity to the applicator, where the highest temperatures are observed, and could thus have contributed to the discrepancy between model and experiment in these regions. However, not accounting for these changes is not anticipated to have a significant impact on the extent of the ablation zone, which is governed by more temperatures at distances ~10-15 mm from the applicator [209]. Furthermore, our computational models did not account for tissue shrinkage [240], [241].

## 5.5. Conclusion

We have developed a system for characterizing 3D transient temperature profiles with MR thermometry in *ex vivo* tissue during 2.45 GHz MWA, and applied the system for experimental validation of MWA computational models. Experimentally measured and simulated temperatures as a function of time and distance were compared at multiple locations along the MWA applicator length and were in agreement with DSC in the range of 0.75 – 0.8. Ablation zone shape was also

compared between MRT-derived and model-predicted using thermal damage profile. The average of MAE % were in the range of 5 % – 8.5 %. These results report on the validity of transient temperature and ablation profiles predicted by the state-of-art computational models of microwave ablation and pave the way for further development and investigation of models for ultimate application in pre-treatment planning of MWA ablation procedures.

# 6. Conclusion and potential directions for further work

This dissertation contributes to the development of thermal therapy systems. Hyperthermia and ablation systems were modelled in 3D, configured and tested *in vivo* in small-animals and in *ex vivo* tissues, paving the path for further investigation to reach the ultimate goal which is development of technologies to address unmet healthcare needs.

To develop thermal therapy systems, one of the most important steps is designing an application-specific device (**key element 3**). This is often implemented by integrating computational modelling and prototyping and experimental evaluation. A significant challenge when using the 3D computational models for device design is the question of model validity **(Key element 2**). In chapter 3 and 4 experimental validation of computational model were considered as a first step to enable further investigations of application and tissue-specific models. Chapter 5 is particularly dedicated to assessing the validity of state-of-art microwave ablation 3D computational models. We developed a system for 2.45 GHz MWA integrated with MRI at 3T, and applied the system experimental validation of MWA computational models. In this dissertation, experimentally validated computational models are then used for device design and characterization for specific tissue and application as follow:

*For specific tissue*; we have employed experimentally validated microwave ablation computational models to evaluate the effect of presence of fibroids (abnormal uterine muscle growth) on endometrial ablation profile (chapter 4).

A possible future direction is to investigate the sensitivity of endometrial ablation profile to the presence of fibroid using microwave ablation computational models incorporating temperature dependent dielectric properties at 915 MHz that are recently measured in [242]. This could not be done at the time the research conducted in this dissertation was performed due to the

lack of published data on uterine fibroid dielectric properties, and their temperature dependencies. As this data becomes available from experimental studies, incorporating them into computational models would further enhance the utility of the modeling work presented in this dissertation.

*For specific application*; In chapter 3, we have developed a small-animal hyperthermia platform, to locally deliver energy to the target while thermally sparing the surroundings. To implement this, we used a model-based approach to design and characterize a microwave applicator and fabricated and tested the optimized applicator experimentally in both agar phantom and *in vivo* in mice. Since the creation of this device, devices have been shared with research groups at external institutions who are investigating its use in experimental studies involving triggered drug release from temperature-sensitive liposomes.

A possible future research direction is to investigate the validity of computational model *in vivo* in integration with 3T MRI. Developing an *in vivo* ablation platform integrated with MR thermometry may be challenging due to the presence of motion and blood perfusion. Motion compensation techniques may be applied to correct MRI estimates of temperature during the ablation experiments [243]–[245].

Real-time temperature monitoring is one of the main challenges of thermal therapy system developments **(Key element 1**). A combination of temperature and time is an indicator of the thermal dose delivery to the target. Therefore, measuring temperature during the heating experiment is of high significance, particularly for hyperthermia platform, where tissue temperature needs to be regulated within a narrow range. Real time monitoring of tissue temperature is a necessity for hyperthermia systems in order to ensure the delivered temperature profile is within the hyperthermic range to avoid irreversible thermal damage to the tissue. Temperature rise beyond the hyperthermic range could eliminate the hyperthermia-induced

physiological effects. Different methods for temperature monitoring during the heat exposure was reviewed in chapter 2. We developed a microwave hyperthermia system integrated with a 14 T ultra-high field small-animal MRI scanner to facilitate real-time temperature monitoring with MR thermometry. We implemented a real-time temperature-based feedback control to keep the target temperature in the desired range for prolonged period of time (chapter 3).

A possible direction for future research is to incorporate the developed hyperthermia platform to investigate the effect of heat on the immune system behavior in small - animals [246], [247] and to integrate temperature sensitive liposomes for drug delivery to the tumor site and implement a comparative assessment to study the density and performance of delivered drug in the absence and presence of heat [248]–[250].

In reference to above, the main contributions of this dissertation are: (1) assessing the validity microwave ablation computational models volumetrically in comparison to existing methods in literature such as using temperature sensors in few points or superficial temperature measurements with infrared cameras; (2) designing a 2.45 GHz microwave applicator integrated in a hyperthermia platform to focus heating to the tumor volume located at 1 - 3 mm from the skin surface, with minimal heating of the surrounding tissue; (3) development of small-animal hyperthermia platform with real-time temperature monitoring and input energy control schemes; (4) showing the impact of uterine fibroids on the extent of microwave endometrial ablation patterns achieved with the global endometrial ablation 915 MHz microwave applicator studied in this dissertation.

# References


[1] K. F. Chu and D. E. Dupuy, “Thermal ablation of tumours: biological mechanisms and advances in therapy,” *Nat. Rev. Cancer*, vol. 14, no. 3, pp. 199–208, Mar. 2014, doi: 10.1038/nrc3672.

[2] R. D. Issels *et al.*, “Neo-adjuvant chemotherapy alone or with regional hyperthermia for localised high-risk soft-tissue sarcoma: a randomised phase 3 multicentre study,” *Lancet Oncol.*, vol. 11, no. 6, pp. 561–570, Jun. 2010, doi: 10.1016/S1470-2045(10)70071-1.

[3] P. K. Sneed *et al.*, “Survival benefit of hyperthermia in a prospective randomized trial of brachytherapy boost +/- hyperthermia for glioblastoma multiforme,” *Int. J. Radiat. Oncol. Biol. Phys.*, vol. 40, no. 2, pp. 287–295, Jan. 1998, doi: 10.1016/s0360-3016(97)00731-1.

[4] E. L. Jones *et al.*, “Randomized trial of hyperthermia and radiation for superficial tumors,” *J. Clin. Oncol. Off. J. Am. Soc. Clin. Oncol.*, vol. 23, no. 13, pp. 3079–3085, May 2005, doi: 10.1200/JCO.2005.05.520.

[5] Z. Gu, C. M. Rappaport, P. J. Wang, and B. A. VanderBrink, “A 2 1/4-turn spiral antenna for catheter cardiac ablation,” *IEEE Trans. Biomed. Eng.*, vol. 46, no. 12, pp. 1480–1482, Dec. 1999, doi: 10.1109/10.804576.

[6] D. A. Hodgson, I. B. Feldberg, N. Sharp, N. Cronin, M. Evans, and L. Hirschowitz, “Microwave endometrial ablation: development, clinical trials and outcomes at three years,” *Br. J. Obstet. Gynaecol.*, vol. 106, no. 7, pp. 684–694, Jul. 1999, doi: 10.1111/j.1471-0528.1999.tb08368.x.

[7] J. Reeves, M. Birch, K. Munro, and R. Collier, “Investigation into the thermal distribution of microwave helical antennas designed for the treatment of Barrett’s oesophagus,” *Phys. Med. Biol.*, vol. 47, no. 19, pp. 3557–3564, Oct. 2002, doi: 10.1088/0031-9155/47/19/309.

[8] F. Fani, E. Schena, P. Saccomandi, and S. Silvestri, “CT-based thermometry: An overview,” *Int. J. Hyperthermia*, vol. 30, no. 4, pp. 219–227, 2014.

[9] J. Haveman, O. A. G. Smals, and H. M. Rodermond, “Effects of hyperthermia on the rat bladder: a pre-clinical study on thermometry and functional damage after treatment,” *Int. J. Hyperthermia*, vol. 19, no. 1, pp. 45–57, 2003.

[10] K. Arunachalam, P. R. Stauffer, P. F. Maccarini, S. Jacobsen, and F. Sterzer, “Characterization of a digital microwave radiometry system for noninvasive thermometry using a temperature-controlled homogeneous test load,” *Phys. Med. Biol.*, vol. 53, no. 14, p. 3883, 2008.

[11] P. Faridi, S. H. Bossmann, and P. Prakash, “Image-guided cancer thermal therapies,” in *Magnetic Nanomaterials*, 2017, pp. 195–220.

[12] B. A. Inman, P. R. Stauffer, O. A. Craciunescu, P. F. Maccarini, M. W. Dewhirst, and Z. Vujaskovic, “A pilot clinical trial of intravesical mitomycin-C and external deep pelvic hyperthermia for non-muscle-invasive bladder cancer,” *Int. J. Hyperthermia*, vol. 30, no. 3, pp. 171–175, 2014.

[13] P. Schildkopf *et al.*, “Biological rationales and clinical applications of temperature controlled hyperthermia-implications for multimodal cancer treatments,” *Curr. Med. Chem.*, vol. 17, no. 27, pp. 3045–3057, 2010.

[14] R. Colombo *et al.*, “Combination of intravesical chemotherapy and hyperthermia for the treatment of superficial bladder cancer: preliminary clinical experience,” *Crit. Rev. Oncol. Hematol.*, vol. 47, no. 2, pp. 127–139, 2003.

[15] V. Rieke and K. B. Pauly, “MR Thermometry,” *J. Magn. Reson. Imaging JMRI*, vol. 27, no. 2, pp. 376–390, Feb. 2008, doi: 10.1002/jmri.21265.
[16] G. Shafirstein and Y. Feng, “The role of mathematical modelling in thermal medicine,” *Int. J. Hyperth. Off. J. Eur. Soc. Hyperthermic Oncol. North Am. Hyperth. Group*, vol. 29, no. 4, pp. 259–261, Jun. 2013, doi: 10.3109/02656736.2013.800999.
[17] R. L. Siegel, K. D. Miller, and A. Jemal, “Cancer statistics, 2020,” *CA. Cancer J. Clin.*, vol. 70, no. 1, pp. 7–30, 2020, doi: 10.3322/caac.21590.
[18] K. E. Tschoep-Lechner *et al.*, “Gemcitabine and cisplatin combined with regional hyperthermia as second-line treatment in patients with gemcitabine-refractory advanced pancreatic cancer,” *Int. J. Hyperth. Off. J. Eur. Soc. Hyperthermic Oncol. North Am. Hyperth. Group*, vol. 29, no. 1, pp. 8–16, 2013, doi: 10.3109/02656736.2012.740764.
[19] T. Conroy *et al.*, “FOLFIRINOX versus gemcitabine for metastatic pancreatic cancer,” *N. Engl. J. Med.*, vol. 364, no. 19, pp. 1817–1825, May 2011, doi: 10.1056/NEJMoa1011923.
[20] X. Yu, Y. Zhang, C. Chen, Q. Yao, and M. Li, “Targeted drug delivery in pancreatic cancer,” *Biochim. Biophys. Acta BBA-Rev. Cancer*, vol. 1805, no. 1, pp. 97–104, 2010.
[21] M. Yu and I. F. Tannock, “Targeting Tumor Architecture to Favor Drug Penetration: A New Weapon to Combat Chemoresistance in Pancreatic Cancer?,” *Cancer Cell*, vol. 21, no. 3, pp. 327–329, Mar. 2012, doi: 10.1016/j.ccr.2012.03.002.
[22] Z. Bai *et al.*, “Intratumoral radiofrequency hyperthermia-enhanced direct chemotherapy of pancreatic cancer,” *Oncotarget*, vol. 8, no. 2, pp. 3591–3599, Sep. 2016, doi: 10.18632/oncotarget.12295.
[23] M. Kakehi *et al.*, “Multi-institutional clinical studies on hyperthermia combined with radiotherapy or chemotherapy in advanced cancer of deep-seated organs,” *Int. J. Hyperthermia*, vol. 6, no. 4, pp. 719–740, 1990.
[24] B. A. Ruggeri, F. Camp, and S. Miknyoczki, “Animal models of disease: pre-clinical animal models of cancer and their applications and utility in drug discovery,” *Biochem. Pharmacol.*, vol. 87, no. 1, pp. 150–161, Jan. 2014, doi: 10.1016/j.bcp.2013.06.020.
[25] Y. Xu *et al.*, “Fever-range whole body hyperthermia increases the number of perfused tumor blood vessels and therapeutic efficacy of liposomally encapsulated doxorubicin,” *Int. J. Hyperthermia*, vol. 23, no. 6, pp. 513–527, 2007.
[26] V. Kumar, R. Chodankar, and J. K. Gupta, “Endometrial Ablation for Heavy Menstrual Bleeding,” *Womens Health*, vol. 12, no. 1, pp. 45–52, Jan. 2016, doi: 10.2217/whe.15.86.
[27] H. Fallahi, J. Šebek, E. Frattura, J. Schenck, and P. Prakash, “Global microwave endometrial ablation for menorrhagia treatment,” in *Energy-based Treatment of Tissue and Assessment IX*, 2017, vol. 10066, p. 100660K.
[28] G. Shafirstein and Y. Feng, *The role of mathematical modelling in thermal medicine*. Taylor & Francis, 2013.
[29] G. Deshazer, P. Prakash, D. Merck, and D. Haemmerich, “Experimental measurement of microwave ablation heating pattern and comparison to computer simulations,” *Int. J. Hyperthermia*, vol. 33, no. 1, pp. 74–82, 2017.
[30] P. Prakash, V. A. Salgaonkar, and C. J. Diederich, “Modelling of endoluminal and interstitial ultrasound hyperthermia and thermal ablation: Applications for device design, feedback control and treatment planning,” *Int. J. Hyperthermia*, vol. 29, no. 4, pp. 296–307, 2013.

[31] J. Chiang, P. Wang, and C. L. Brace, “Computational modelling of microwave tumour ablations,” *Int. J. Hyperth. Off. J. Eur. Soc. Hyperthermic Oncol. North Am. Hyperth. Group*, vol. 29, no. 4, pp. 308–317, Jun. 2013, doi: 10.3109/02656736.2013.799295.
[32] V. Lopresto, R. Pinto, G. A. Lovisolo, and M. Cavagnaro, “Changes in the dielectric properties of ex vivo bovine liver during microwave thermal ablation at 2.45 GHz,” *Phys. Med. Biol.*, vol. 57, no. 8, pp. 2309–2327, Apr. 2012, doi: 10.1088/0031-9155/57/8/2309.
[33] Z. Ji and C. L. Brace, “Expanded modeling of temperature-dependent dielectric properties for microwave thermal ablation,” *Phys. Med. Biol.*, vol. 56, no. 16, pp. 5249–5264, Aug. 2011, doi: 10.1088/0031-9155/56/16/011.
[34] C. Rossmanna and D. Haemmerich, “Review of temperature dependence of thermal properties, dielectric properties, and perfusion of biological tissues at hyperthermic and ablation temperatures,” *Crit. Rev. Biomed. Eng.*, vol. 42, no. 6, pp. 467–492, 2014.
[35] D. T. Tompkins *et al.*, “Temperature-dependent versus constant-rate blood perfusion modelling in ferromagnetic thermoseed hyperthermia: results with a model of the human prostate,” *Int. J. Hyperth. Off. J. Eur. Soc. Hyperthermic Oncol. North Am. Hyperth. Group*, vol. 10, no. 4, pp. 517–536, Aug. 1994.
[36] J. Sebek, N. Albin, R. Bortel, B. Natarajan, and P. Prakash, “Sensitivity of microwave ablation models to tissue biophysical properties: A first step toward probabilistic modeling and treatment planning,” *Med. Phys.*, vol. 43, no. 5, p. 2649, May 2016, doi: 10.1118/1.4947482.
[37] D. Liu and C. L. Brace, “Numerical simulation of microwave ablation incorporating tissue contraction based on thermal dose,” *Phys. Med. Biol.*, vol. 62, no. 6, pp. 2070–2086, Mar. 2017, doi: 10.1088/1361-6560/aa5de4.
[38] M. Hurwitz and P. Stauffer, “Hyperthermia, radiation and chemotherapy: the role of heat in multidisciplinary cancer care,” in *Seminars in oncology*, 2014, vol. 41, pp. 714–729.
[39] V. Rieke and K. B. Pauly, “MR Thermometry,” *J. Magn. Reson. Imaging JMRI*, vol. 27, no. 2, pp. 376–390, Feb. 2008, doi: 10.1002/jmri.21265.
[40] P. Faridi, S. H. Bossmann, and P. Prakash, “Simulation-based design and characterization of a microwave applicator for MR-guided hyperthermia experimental studies in small animals,” *Biomed. Phys. Eng. Express*, vol. 6, no. 1, p. 015001, Nov. 2019, doi: 10.1088/2057-1976/ab36dd.
[41] S. Curto *et al.*, “An integrated platform for small-animal hyperthermia investigations under ultra-high-field MRI guidance,” *Int. J. Hyperth. Off. J. Eur. Soc. Hyperthermic Oncol. North Am. Hyperth. Group*, vol. 34, no. 4, pp. 341–351, 2018, doi: 10.1080/02656736.2017.1339126.
[42] P. Faridi, H. Fallahi, and P. Prakash, “Evaluation of the Effect of Uterine Fibroids on Microwave Endometrial Ablation Profiles,” in *2018 40th Annual International Conference of the IEEE Engineering in Medicine and Biology Society (EMBC)*, Jul. 2018, pp. 3236–3239, doi: 10.1109/EMBC.2018.8513051.
[43] P. Faridi and P. Prakash, “Experimental Validation of Computational Models of Microwave Tissue Heating with Magnetic Resonance Thermometry,” in *2018 IEEE/MTT-S International Microwave Symposium - IMS*, Jun. 2018, pp. 1282–1284, doi: 10.1109/MWSYM.2018.8439359.
[44] P. Faridi, P. Keselman, H. Fallahi, and P. Prakash, “Experimental assessment of microwave ablation computational modeling with MR thermometry,” *Med. Phys.*, 2020.

[45] P. Faridi, S. H. Bossmann, and P. Prakash, “Image-Guided Cancer Thermal Therapies,” in *Magnetic Nanomaterials*, 2017, pp. 195–220.
[46] R. D. Issels *et al.*, “Neo-adjuvant chemotherapy alone or with regional hyperthermia for localised high-risk soft-tissue sarcoma: a randomised phase 3 multicentre study,” *Lancet Oncol.*, vol. 11, no. 6, pp. 561–570, Jun. 2010, doi: 10.1016/S1470-2045(10)70071-1.
[47] E. L. Jones *et al.*, “Randomized trial of hyperthermia and radiation for superficial tumors,” *J. Clin. Oncol. Off. J. Am. Soc. Clin. Oncol.*, vol. 23, no. 13, pp. 3079–3085, May 2005, doi: 10.1200/JCO.2005.05.520.
[48] P. K. Sneed *et al.*, “Survival benefit of hyperthermia in a prospective randomized trial of brachytherapy boost +/- hyperthermia for glioblastoma multiforme,” *Int. J. Radiat. Oncol. Biol. Phys.*, vol. 40, no. 2, pp. 287–295, Jan. 1998.
[49] K. F. Chu and D. E. Dupuy, “Thermal ablation of tumours: biological mechanisms and advances in therapy,” *Nat. Rev. Cancer*, vol. 14, no. 3, pp. 199–208, 2014.
[50] V. Muralidharan, C. Malcontenti-Wilson, and C. Christophi, “Effect of blood flow occlusion on laser hyperthermia for liver metastases,” *J. Surg. Res.*, vol. 103, no. 2, pp. 165–174, 2002.
[51] C. W. Song, “Effect of local hyperthermia on blood flow and microenvironment: a review,” *Cancer Res.*, vol. 44, no. 10 Supplement, pp. 4721s–4730s, 1984.
[52] K. Liberek, A. Lewandowska, and S. Ziętkiewicz, “Chaperones in control of protein disaggregation,” *EMBO J.*, vol. 27, no. 2, pp. 328–335, 2008.
[53] R. H. Burdon, A. Slater, M. McMahon, and A. C. Cato, “Hyperthermia and the heat-shock proteins of HeLa cells.,” *Br. J. Cancer*, vol. 45, no. 6, p. 953, 1982.
[54] S. A. Sapareto, L. E. Hopwood, W. C. Dewey, M. R. Raju, and J. W. Gray, “Effects of hyperthermia on survival and progression of Chinese hamster ovary cells,” *Cancer Res.*, vol. 38, no. 2, pp. 393–400, Feb. 1978.
[55] M. W. Dewhirst, B. L. Viglianti, M. Lora-Michiels, M. Hanson, and P. J. Hoopes, “Basic principles of thermal dosimetry and thermal thresholds for tissue damage from hyperthermia,” *Int. J. Hyperth. Off. J. Eur. Soc. Hyperthermic Oncol. North Am. Hyperth. Group*, vol. 19, no. 3, pp. 267–294, Jun. 2003, doi: 10.1080/0265673031000119006.
[56] R. D. Issels, “Hyperthermia adds to chemotherapy,” *Eur. J. Cancer*, vol. 44, no. 17, pp. 2546–2554, 2008.
[57] S. B. Field and J. W. Hand, *An introduction to the practical aspects of clinical hyperthermia*. Taylor & Francis Group, 1990.
[58] G. P. Raaphorst, “Fundamental aspects of hyperthermic biology,” *Introd. Pract. Asp. Clin. Hyperth. Lond. Taylor Francis*, pp. 10–54, 1990.
[59] J. van der Zee, “Heating the patient: a promising approach?,” *Ann. Oncol.*, vol. 13, no. 8, pp. 1173–1184, 2002.
[60] C. W. Song, A. Shakil, R. J. Griffin, and K. Okajima, “Improvement of tumor oxygenation status by mild temperature hyperthermia alone or in combination with carbogen.,” in *Seminars in oncology*, 1997, vol. 24, pp. 626–632, Accessed: Sep. 08, 2016. [Online]. Available: http://europepmc.org/abstract/med/9422259.
[61] S. Rockwell, I. T. Dobrucki, E. Y. Kim, S. T. Marrison, and V. T. Vu, “Hypoxia and radiation therapy: past history, ongoing research, and future promise,” *Curr. Mol. Med.*, vol. 9, no. 4, pp. 442–458, 2009.

[62] A. Westra and W. C. Dewey, “Variation in sensitivity to heat shock during the cell-cycle of Chinese hamster cells in vitro,” *Int. J. Radiat. Biol. Relat. Stud. Phys. Chem. Med.*, vol. 19, no. 5, pp. 467–477, 1971.
[63] J. J. Skitzki, E. A. Repasky, and S. S. Evans, “Hyperthermia as an immunotherapy strategy for cancer,” *Curr. Opin. Investig. Drugs Lond. Engl. 2000*, vol. 10, no. 6, p. 550, 2009.
[64] H. Shi *et al.*, “Hyperthermia enhances CTL cross-priming,” *J. Immunol.*, vol. 176, no. 4, pp. 2134–2141, 2006.
[65] S. M. Todryk, A. A. Melcher, A. G. Dalgleish, and R. G. Vile, “Heat shock proteins refine the danger theory,” *Immunology*, vol. 99, no. 3, pp. 334–337, 2000.
[66] J. A. Dickson and S. K. Calderwood, “Temperature range and selective sensitivity of tumors to hyperthermia: a critical review,” *Ann. N. Y. Acad. Sci.*, vol. 335, no. 1, pp. 180–205, 1980.
[67] S. K. Calderwood, “Hyperthermia, the tumor microenvironment and immunity,” in *Tumor Ablation*, Springer, 2013, pp. 29–37.
[68] K. F. Chu and D. E. Dupuy, “Thermal ablation of tumours: biological mechanisms and advances in therapy,” *Nat. Rev. Cancer*, vol. 14, no. 3, pp. 199–208, 2014.
[69] R. K. Jain, “Barriers to drug dellivery in solid tumors,” *Sci. Am.*, vol. 271, no. 1, pp. 58–65, 1994.
[70] E. S. Gil and S. M. Hudson, “Stimuli-reponsive polymers and their bioconjugates,” *Prog. Polym. Sci.*, vol. 29, no. 12, pp. 1173–1222, 2004.
[71] A. Chilkoti, M. R. Dreher, D. E. Meyer, and D. Raucher, “Targeted drug delivery by thermally responsive polymers,” *Adv. Drug Deliv. Rev.*, vol. 54, no. 5, pp. 613–630, 2002.
[72] G. Kong *et al.*, “Efficacy of liposomes and hyperthermia in a human tumor xenograft model: importance of triggered drug release,” *Cancer Res.*, vol. 60, no. 24, pp. 6950–6957, 2000.
[73] C. J. Simon, D. E. Dupuy, and W. W. Mayo-Smith, “Microwave Ablation: Principles and Applications,” *RadioGraphics*, vol. 25, no. suppl_1, pp. S69–S83, Oct. 2005, doi: 10.1148/rg.25si055501.
[74] C. Gabriel, S. Gabriel, and E. Corthout, “The dielectric properties of biological tissues: I. Literature survey,” *Phys. Med. Biol.*, vol. 41, no. 11, pp. 2231–2249, Nov. 1996.
[75] S. Gabriel, R. W. Lau, and C. Gabriel, “The dielectric properties of biological tissues: III. Parametric models for the dielectric spectrum of tissues,” *Phys. Med. Biol.*, vol. 41, no. 11, pp. 2271–2293, Nov. 1996.
[76] D. Fatehi, J. van der Zee, M. de Bruijne, M. Franckena, and G. C. van Rhoon, “RF-power and temperature data analysis of 444 patients with primary cervical cancer: deep hyperthermia using the Sigma-60 applicator is reproducible,” *Int. J. Hyperth. Off. J. Eur. Soc. Hyperthermic Oncol. North Am. Hyperth. Group*, vol. 23, no. 8, pp. 623–643, Dec. 2007, doi: 10.1080/02656730701827557.
[77] K.-S. Cheng, V. Stakhursky, O. I. Craciunescu, P. Stauffer, M. Dewhirst, and S. K. Das, “Fast temperature optimization of multi-source hyperthermia applicators with reduced-order modeling of ‘virtual sources,’” *Phys. Med. Biol.*, vol. 53, no. 6, pp. 1619–1635, Mar. 2008, doi: 10.1088/0031-9155/53/6/008.
[78] P. R. Stauffer, “Evolving technology for thermal therapy of cancer,” *Int. J. Hyperth. Off. J. Eur. Soc. Hyperthermic Oncol. North Am. Hyperth. Group*, vol. 21, no. 8, pp. 731–744, Dec. 2005, doi: 10.1080/02656730500331868.

[79] I. Tudorancea *et al.*, “New experimental model for single liver lobe hyperthermia in small animals using non-directional microwaves,” *PLoS ONE*, vol. 12, no. 9, Sep. 2017, doi: 10.1371/journal.pone.0184810.
[80] E. A. L. Raaijmakers *et al.*, “An MR-compatible antenna and application in a murine superficial hyperthermia applicator,” *Int. J. Hyperth. Off. J. Eur. Soc. Hyperthermic Oncol. North Am. Hyperth. Group*, pp. 1–7, Sep. 2017, doi: 10.1080/02656736.2017.1369172.
[81] T. Motomura *et al.*, “Evaluation of systemic external microwave hyperthermia for treatment of pleural metastasis in orthotopic lung cancer model,” *Oncol. Rep.*, vol. 24, no. 3, pp. 591–598, 2010.
[82] P. Togni, J. Vrba, and L. Vannucci, “Microwave applicator for hyperthermia treatment on in vivo melanoma model,” *Med. Biol. Eng. Comput.*, vol. 48, no. 3, pp. 285–292, 2010.
[83] S. Salahi *et al.*, “Miniature microwave applicator for murine bladder hyperthermia studies,” *Int. J. Hyperthermia*, vol. 28, no. 5, pp. 456–465, 2012.
[84] T. P. Ryan, P. F. Turner, and B. Hamilton, “Interstitial microwave transition from hyperthermia to ablation: Historical perspectives and current trends in thermal therapy,” *Int. J. Hyperthermia*, vol. 26, no. 5, pp. 415–433, 2010.
[85] S. Curto, M. Taj-Eldin, D. Fairchild, and P. Prakash, “Microwave ablation at 915 MHz vs 2.45 GHz: A theoretical and experimental investigation,” *Med. Phys.*, vol. 42, no. 11, pp. 6152–6161, Nov. 2015, doi: 10.1118/1.4931959.
[86] J. F. Sawicki, J. D. Shea, N. Behdad, and S. C. Hagness, “The impact of frequency on the performance of microwave ablation,” *Int. J. Hyperth. Off. J. Eur. Soc. Hyperthermic Oncol. North Am. Hyperth. Group*, pp. 1–8, Jul. 2016, doi: 10.1080/02656736.2016.1207254.
[87] M. Cavagnaro, C. Amabile, P. Bernardi, S. Pisa, and N. Tosoratti, “A minimally invasive antenna for microwave ablation therapies: design, performances, and experimental assessment,” *IEEE Trans. Biomed. Eng.*, vol. 58, no. 4, pp. 949–959, 2011.
[88] C. L. Brace, P. F. Laeseke, L. A. Sampson, T. M. Frey, D. W. van der Weide, and F. T. Lee Jr, “Microwave Ablation with a Single Small-Gauge Triaxial Antenna: In Vivo Porcine Liver Model 1,” *Radiology*, vol. 242, no. 2, pp. 435–440, 2007.
[89] D. Yang *et al.*, “A floating sleeve antenna yields localized hepatic microwave ablation,” *IEEE Trans. Biomed. Eng.*, vol. 53, no. 3, pp. 533–537, 2006.
[90] A. M. Ierardi *et al.*, “A new system of microwave ablation at 2450 MHz: preliminary experience,” *Updat. Surg.*, vol. 67, no. 1, pp. 39–45, 2015.
[91] B. T. McWilliams, E. E. Schnell, S. Curto, T. M. Fahrbach, and P. Prakash, “A directional interstitial antenna for microwave tissue ablation: Theoretical and experimental investigation,” *IEEE Trans. Biomed. Eng.*, vol. 62, no. 9, pp. 2144–2150, 2015.
[92] M. Kuang *et al.*, “Liver Cancer: Increased Microwave Delivery to Ablation Zone with Cooled-Shaft Antenna—Experimental and Clinical Studies 1,” *Radiology*, vol. 242, no. 3, pp. 914–924, 2007.
[93] G. Carrafiello *et al.*, “Microwave tumors ablation: principles, clinical applications and review of preliminary experiences,” *Int. J. Surg.*, vol. 6, pp. S65–S69, 2008.
[94] W. Zhou *et al.*, “Comparison of ablation zones among different tissues using 2450-MHz cooled-shaft microwave antenna: results in ex vivo porcine models,” *PloS One*, vol. 8, no. 8, p. e71873, 2013.

[95] L. W. Organ, “Electrophysiologic principles of radiofrequency lesion making,” *Stereotact. Funct. Neurosurg.*, vol. 39, no. 2, pp. 69–76, 1976.
[96] J. W. Hand and G. ter Haar, “Heating techniques in hyperthermia,” *Br. J. Radiol.*, vol. 54, no. 642, pp. 443–466, 1981.
[97] A. S. Wright, L. A. Sampson, T. F. Warner, D. M. Mahvi, and F. T. Lee, “Radiofrequency versus Microwave Ablation in a Hepatic Porcine Model 1,” *Radiology*, vol. 236, no. 1, pp. 132–139, 2005.
[98] W. Clark, “Oscillatory desiccation in the treatment of accessible malignant growths and minor surgical conditions,” *J Adv Ther*, vol. 29, pp. 169–183, 1911.
[99] Y. Ni, S. Mulier, Y. Miao, L. Michel, and G. Marchal, “A review of the general aspects of radiofrequency ablation,” *Abdom. Imaging*, vol. 30, no. 4, pp. 381–400, 2005.
[100] A. L. Denys *et al.*, “Radio-frequency tissue ablation of the liver: in vivo and ex vivo experiments with four different systems,” *Eur. Radiol.*, vol. 13, no. 10, pp. 2346–2352, 2003.
[101] L. Carroll and T. R. Humphreys, “LASER-tissue interactions,” *Clin. Dermatol.*, vol. 24, no. 1, pp. 2–7, 2006.
[102] A. J. Welch, J. H. Torres, and W.-F. Cheong, “Laser physics and laser-tissue interaction,” *Tex. Heart Inst. J.*, vol. 16, no. 3, p. 141, 1989.
[103] R. Steiner, “Laser-tissue interactions,” in *Laser and IPL Technology in Dermatology and Aesthetic Medicine*, Springer, 2011, pp. 23–36.
[104] M. Ahmed, C. L. Brace, F. T. Lee Jr, and S. N. Goldberg, “Principles of and advances in percutaneous ablation,” *Radiology*, vol. 258, no. 2, pp. 351–369, 2011.
[105] R. Fernando, J. Downs, D. Maples, and A. Ranjan, “MRI-guided monitoring of thermal dose and targeted drug delivery for cancer therapy,” *Pharm. Res.*, vol. 30, no. 11, pp. 2709–2717, 2013.
[106] S. E. Norred and J. A. Johnson, “Magnetic resonance-guided laser induced thermal therapy for glioblastoma multiforme: a review,” *BioMed Res. Int.*, vol. 2014, 2014, Accessed: Jan. 13, 2017. [Online]. Available: http://www.hindawi.com/journals/bmri/2014/761312/abs/.
[107] C. M. Tempany, N. J. McDannold, K. Hynynen, and F. A. Jolesz, “Focused ultrasound surgery in oncology: overview and principles,” *Radiology*, vol. 259, no. 1, pp. 39–56, 2011.
[108] S. A. Sapareto and W. C. Dewey, “Thermal dose determination in cancer therapy,” *Int. J. Radiat. Oncol. Biol. Phys.*, vol. 10, no. 6, pp. 787–800, Jun. 1984.
[109] J. E. Kennedy *et al.*, “High-intensity focused ultrasound for the treatment of liver tumours,” *Ultrasonics*, vol. 42, no. 1, pp. 931–935, 2004.
[110] X. Fan and K. Hynynen, “A study of various parameters of spherically curved phased arrays for noninvasive ultrasound surgery,” *Phys. Med. Biol.*, vol. 41, no. 4, p. 591, 1996.
[111] H. Wan, P. VanBaren, E. S. Ebbini, and C. A. Cain, “Ultrasound surgery: Comparison of strategies using phased array systems,” *IEEE Trans. Ultrason. Ferroelectr. Freq. Control*, vol. 43, no. 6, pp. 1085–1098, 1996.
[112] T. Fjield and K. Hynynen, “The combined concentric-ring and sector-vortex phased array for MRI guided ultrasound surgery,” *IEEE Trans. Ultrason. Ferroelectr. Freq. Control*, vol. 44, no. 5, pp. 1157–1167, 1997.

[113] E. B. Hutchinson and K. Hynynen, “Intracavitary ultrasound phased arrays for prostate thermal therapies: MRI compatibility and in vivo testing,” *Med. Phys.*, vol. 25, no. 12, pp. 2392–2399, 1998.
[114] M. O. Köhler *et al.*, “Volumetric HIFU ablation under 3D guidance of rapid MRI thermometry,” *Med. Phys.*, vol. 36, no. 8, pp. 3521–3535, 2009.
[115] M. Hoogenboom *et al.*, “Development of a high-field MR-guided HIFU setup for thermal and mechanical ablation methods in small animals,” *J. Ther. Ultrasound*, vol. 3, no. 1, p. 1, 2015.
[116] M. Hoogenboom, D. Eikelenboom, M. H. den Brok, A. Heerschap, J. J. Fütterer, and G. J. Adema, “Mechanical high-intensity focused ultrasound destruction of soft tissue: working mechanisms and physiologic effects,” *Ultrasound Med. Biol.*, vol. 41, no. 6, pp. 1500–1517, 2015.
[117] N. Hijnen, S. Langereis, and H. Grüll, “Magnetic resonance guided high-intensity focused ultrasound for image-guided temperature-induced drug delivery,” *Adv. Drug Deliv. Rev.*, vol. 72, pp. 65–81, Jun. 2014, doi: 10.1016/j.addr.2014.01.006.
[118] B. Denis de Senneville, B. Quesson, and C. T. Moonen, “Magnetic resonance temperature imaging,” *Int. J. Hyperthermia*, vol. 21, no. 6, pp. 515–531, 2005.
[119] S. Liu and Y. Zhou, “MR temperature imaging using PRF phase difference and a geometric model-based fat suppression method,” *Technol. Health Care*, vol. 23, no. s2, pp. S587–S592, 2015.
[120] L. Winter *et al.*, “Magnetic resonance thermometry: Methodology, pitfalls and practical solutions,” *Int. J. Hyperth. Off. J. Eur. Soc. Hyperthermic Oncol. North Am. Hyperth. Group*, vol. 32, no. 1, pp. 63–75, 2016, doi: 10.3109/02656736.2015.1108462.
[121] L. G. Merckel *et al.*, “First clinical experience with a dedicated MRI-guided high-intensity focused ultrasound system for breast cancer ablation,” *Eur. Radiol.*, vol. 26, no. 11, pp. 4037–4046, Nov. 2016, doi: 10.1007/s00330-016-4222-9.
[122] O. Seror *et al.*, “Real time monitoring of radiofrequency ablation based on MR thermometry and thermal dose in the pig liver in vivo,” *Eur. Radiol.*, vol. 18, no. 2, pp. 408–416, Feb. 2008, doi: 10.1007/s00330-007-0761-4.
[123] V. Rieke and K. Butts Pauly, “MR thermometry,” *J. Magn. Reson. Imaging*, vol. 27, no. 2, pp. 376–390, 2008.
[124] V. Rieke, K. K. Vigen, G. Sommer, B. L. Daniel, J. M. Pauly, and K. Butts, “Referenceless PRF shift thermometry,” *Magn. Reson. Med.*, vol. 51, no. 6, pp. 1223–1231, 2004.
[125] A. Seginer, R. Schmidt, A. Leftin, E. Solomon, and L. Frydman, “Referenceless reconstruction of spatiotemporally encoded imaging data: Principles and applications to real-time MRI,” *Magn. Reson. Med.*, vol. 72, no. 6, pp. 1687–1695, 2014.
[126] K. K. Vigen, B. L. Daniel, J. M. Pauly, and K. Butts, “Triggered, navigated, multi-baseline method for proton resonance frequency temperature mapping with respiratory motion,” *Magn. Reson. Med.*, vol. 50, no. 5, pp. 1003–1010, 2003.
[127] R. Seip, P. VanBaren, C. A. Cain, and E. S. Ebbini, “Noninvasive real-time multipoint temperature control for ultrasound phased array treatments,” *IEEE Trans. Ultrason. Ferroelectr. Freq. Control*, vol. 43, no. 6, pp. 1063–1073, 1996.
[128] L. Curiel, R. Chopra, and K. Hynynen, “In vivo monitoring of focused ultrasound surgery using local harmonic motion,” *Ultrasound Med. Biol.*, vol. 35, no. 1, pp. 65–78, 2009.

[129] M. A. Lewis, R. M. Staruch, and R. Chopra, “Thermometry and ablation monitoring with ultrasound,” *Int. J. Hyperthermia*, vol. 31, no. 2, pp. 163–181, Mar. 2015, doi: 10.3109/02656736.2015.1009180.
[130] B. A. Rabkin, V. Zderic, and S. Vaezy, “Hyperecho in ultrasound images of HIFU therapy: involvement of cavitation,” *Ultrasound Med. Biol.*, vol. 31, no. 7, pp. 947–956, 2005.
[131] F. Fani, E. Schena, P. Saccomandi, and S. Silvestri, “CT-based thermometry: an overview,” *Int. J. Hyperthermia*, vol. 30, no. 4, pp. 219–227, 2014.
[132] D. E. Thrall *et al.*, “Using units of CEM 43°C T90, local hyperthermia thermal dose can be delivered as prescribed,” *Int. J. Hyperthermia*, vol. 16, no. 5, pp. 415–428, Jan. 2000, doi: 10.1080/026567300416712.
[133] C. Lafon *et al.*, “Cylindrical thermal coagulation necrosis using an interstitial applicator with a plane ultrasonic transducer: in vitro and in vivo experiments versus computer simulations,” *Int. J. Hyperth. Off. J. Eur. Soc. Hyperthermic Oncol. North Am. Hyperth. Group*, vol. 16, no. 6, pp. 508–522, Dec. 2000.
[134] V. Salgaonkar *et al.*, “Implementation of sonication and feedback control strategies for targeted hyperthermia in prostate with a commercial MR-guided endorectal ultrasound ablation array,” *J. Ther. Ultrasound*, vol. 3, no. 1, p. 1, 2015.
[135] J. K. Enholm, M. O. Kohler, B. Quesson, C. Mougenot, C. T. Moonen, and S. D. Sokka, “Improved volumetric MR-HIFU ablation by robust binary feedback control,” *IEEE Trans. Biomed. Eng.*, vol. 57, no. 1, pp. 103–113, 2010.
[136] D. Arora *et al.*, “MR thermometry-based feedback control of efficacy and safety in minimum-time thermal therapies: Phantom and in-vivo evaluations,” *Int. J. Hyperthermia*, vol. 22, no. 1, pp. 29–42, 2006.
[137] B. Z. Fite *et al.*, “Magnetic resonance thermometry at 7T for real-time monitoring and correction of ultrasound induced mild hyperthermia,” *PloS One*, vol. 7, no. 4, p. e35509, 2012.
[138] D. Haemmerich and J. G. Webster, “Automatic control of finite element models for temperature-controlled radiofrequency ablation,” *Biomed. Eng. Online*, vol. 4, no. 1, p. 1, 2005.
[139] R. Staruch, R. Chopra, and K. Hynynen, “Hyperthermia in Bone Generated with MR Imaging–controlled Focused Ultrasound: Control Strategies and Drug Delivery,” *Radiology*, vol. 263, no. 1, pp. 117–127, 2012.
[140] P. VanBaren and E. S. Ebbini, “Multipoint temperature control during hyperthermia treatments: theory and simulation,” *IEEE Trans. Biomed. Eng.*, vol. 42, no. 8, pp. 818–827, 1995.
[141] E. Hutchinson, M. Dahleh, and K. Hynynen, “The feasibility of MRI feedback control for intracavitary phased array hyperthermia treatments,” *Int. J. Hyperthermia*, vol. 14, no. 1, pp. 39–56, 1998.
[142] D. Arora, M. Skliar, and R. B. Roemer, “Model-predictive control of hyperthermia treatments,” *IEEE Trans. Biomed. Eng.*, vol. 49, no. 7, pp. 629–639, Jul. 2002, doi: 10.1109/TBME.2002.1010846.
[143] B. Z. Fite *et al.*, “Magnetic resonance thermometry at 7T for real-time monitoring and correction of ultrasound induced mild hyperthermia,” *PloS One*, vol. 7, no. 4, p. e35509, 2012.

[144] A. Jackson, “Analysis of dynamic contrast enhanced MRI,” *Br. J. Radiol.*, 2014, Accessed: Oct. 31, 2016. [Online]. Available: http://www.birpublications.org/doi/full/10.1259/bjr/16652509.
[145] S.-D. Chen, “A new image quality measure for assessment of histogram equalization-based contrast enhancement techniques,” *Digit. Signal Process.*, vol. 22, no. 4, pp. 640–647, 2012.
[146] M. Kitano, H. Sakamoto, and M. Kudo, “Endoscopic ultrasound: contrast enhancement,” *Gastrointest. Endosc. Clin. N. Am.*, vol. 22, no. 2, pp. 349–358, 2012.
[147] L. D. Chen *et al.*, “Enhancement patterns of intrahepatic cholangiocarcinoma: comparison between contrast-enhanced ultrasound and contrast-enhanced CT,” *Br. J. Radiol.*, 2014, Accessed: Oct. 31, 2016. [Online]. Available: http://www.birpublications.org/doi/full/10.1259/bjr/22318475.
[148] S.-C. Huang and C.-H. Yeh, “Image contrast enhancement for preserving mean brightness without losing image features,” *Eng. Appl. Artif. Intell.*, vol. 26, no. 5, pp. 1487–1492, 2013.
[149] G. Jiang *et al.*, “Image contrast enhancement with brightness preservation using an optimal gamma correction and weighted sum approach,” *J. Mod. Opt.*, vol. 62, no. 7, pp. 536–547, 2015.
[150] V. N. Varghees, M. S. Manikandan, and R. Gini, “Adaptive MRI image denoising using total-variation and local noise estimation,” in *Advances in Engineering, Science and Management (ICAESM), 2012 International Conference on*, 2012, pp. 506–511, Accessed: Oct. 31, 2016. [Online]. Available: http://ieeexplore.ieee.org/xpls/abs_all.jsp?arnumber=6216055.
[151] J. V. Manjón, P. Coupé, L. Concha, A. Buades, D. L. Collins, and M. Robles, “Diffusion weighted image denoising using overcomplete local PCA,” *PloS One*, vol. 8, no. 9, p. e73021, 2013.
[152] H. M. Golshan, R. P. Hasanzadeh, and S. C. Yousefzadeh, “An MRI denoising method using image data redundancy and local SNR estimation,” *Magn. Reson. Imaging*, vol. 31, no. 7, pp. 1206–1217, 2013.
[153] J. Klosowski and J. Frahm, “Image Denoising for Real-Time MRI,” *Magn. Reson. Med.*, 2016, Accessed: Oct. 31, 2016. [Online]. Available: http://onlinelibrary.wiley.com/doi/10.1002/mrm.26205/full.
[154] S. L. Fossheim, K. A. Il’yasov, J. Hennig, and A. Bjørnerud, “Thermosensitive paramagnetic liposomes for temperature control during MR imaging-guided hyperthermia: in vitro feasibility studies,” *Acad. Radiol.*, vol. 7, no. 12, pp. 1107–1115, 2000.
[155] N. McDannold, S. L. Fossheim, H. Rasmussen, H. Martin, N. Vykhodtseva, and K. Hynynen, “Heat-activated Liposomal MR Contrast Agent: Initial in Vivo Results in Rabbit Liver and Kidney 1,” *Radiology*, vol. 230, no. 3, pp. 743–752, 2004.
[156] L. Frich, A. Bjørnerud, S. Fossheim, T. Tillung, and I. Gladhaug, “Experimental application of thermosensitive paramagnetic liposomes for monitoring magnetic resonance imaging guided thermal ablation,” *Magn. Reson. Med.*, vol. 52, no. 6, pp. 1302–1309, 2004.
[157] P. Faridi, S. H. Bossmann, and P. Prakash, “Simulation-based design and characterization of a microwave applicator for MR-guided hyperthermia experimental studies in small animals,” *Biomed. Phys. Eng. Express*, vol. 6, no. 1, p. 015001, 2020.

[158] N. R. Datta *et al.*, “Local hyperthermia combined with radiotherapy and-/or chemotherapy: recent advances and promises for the future,” *Cancer Treat. Rev.*, vol. 41, no. 9, pp. 742–753, Nov. 2015, doi: 10.1016/j.ctrv.2015.05.009.
[159] G. C. van Rhoon, “Is CEM43 still a relevant thermal dose parameter for hyperthermia treatment monitoring?,” *Int. J. Hyperthermia*, vol. 32, no. 1, pp. 50–62, 2016.
[160] T. Ohguri *et al.*, “Relationships between thermal dose parameters and the efficacy of definitive chemoradiotherapy plus regional hyperthermia in the treatment of locally advanced cervical cancer: data from a multicentre randomised clinical trial,” *Int. J. Hyperthermia*, vol. 34, no. 4, pp. 461–468, 2018.
[161] J. Mahmood *et al.*, “Immunotherapy, radiotherapy, and hyperthermia: A combined therapeutic approach in pancreatic cancer treatment,” *Cancers*, vol. 10, no. 12, p. 469, 2018.
[162] B. Frey *et al.*, “Old and new facts about hyperthermia-induced modulations of the immune system,” *Int. J. Hyperthermia*, vol. 28, no. 6, pp. 528–542, 2012.
[163] S. Toraya-Brown and S. Fiering, “Local tumour hyperthermia as immunotherapy for metastatic cancer,” *Int. J. Hyperthermia*, vol. 30, no. 8, pp. 531–539, 2014.
[164] A. Gasselhuber *et al.*, “Targeted drug delivery by high intensity focused ultrasound mediated hyperthermia combined with temperature-sensitive liposomes: computational modelling and preliminary in vivo validation,” *Int. J. Hyperthermia*, vol. 28, no. 4, pp. 337–348, 2012.
[165] M. N. Centelles *et al.*, “Image-guided thermosensitive liposomes for focused ultrasound drug delivery: Using NIRF-labelled lipids and topotecan to visualise the effects of hyperthermia in tumours,” *J. Controlled Release*, vol. 280, pp. 87–98, 2018.
[166] L. Willerding *et al.*, “Method of hyperthermia and tumor size influence effectiveness of doxorubicin release from thermosensitive liposomes in experimental tumors,” *J. Control. Release Off. J. Control. Release Soc.*, vol. 222, pp. 47–55, Jan. 2016, doi: 10.1016/j.jconrel.2015.12.004.
[167] A. L. Bredlau *et al.*, “Thermal Therapy Approaches for Treatment of Brain Tumors in Animals and Humans,” *Crit. Rev. Biomed. Eng.*, vol. 44, no. 6, pp. 443–457, 2016, doi: 10.1615/CritRevBiomedEng.2017021249.
[168] N. Farr *et al.*, “Hyperthermia-enhanced targeted drug delivery using magnetic resonance-guided focussed ultrasound: a pre-clinical study in a genetic model of pancreatic cancer,” *Int. J. Hyperth. Off. J. Eur. Soc. Hyperthermic Oncol. North Am. Hyperth. Group*, pp. 1–8, Jul. 2017, doi: 10.1080/02656736.2017.1336675.
[169] C. Bing *et al.*, “Localised hyperthermia in rodent models using an MRI-compatible high-intensity focused ultrasound system,” *Int. J. Hyperthermia*, vol. 31, no. 8, pp. 813–822, 2015.
[170] R. Staruch, R. Chopra, and K. Hynynen, “Hyperthermia in bone generated with MR imaging–controlled focused ultrasound: Control strategies and drug delivery,” *Radiology*, vol. 263, no. 1, pp. 117–127, 2012.
[171] M. E. Poorman *et al.*, “Open-source, small-animal magnetic resonance-guided focused ultrasound system,” *J. Ther. Ultrasound*, vol. 4, no. 1, p. 22, 2016.
[172] J. E. Lee *et al.*, “Assessing high-intensity focused ultrasound treatment of prostate cancer with hyperpolarized 13C dual-agent imaging of metabolism and perfusion,” *NMR Biomed.*, p. e3962, 2018.

[173] T. J. Vogl *et al.*, “MR-based thermometry of laser induced thermotherapy: temperature accuracy and temporal resolution in vitro at 0.2 and 1.5 T magnetic field strengths,” *Lasers Surg. Med.*, vol. 44, no. 3, pp. 257–265, 2012.
[174] F. Zhang *et al.*, “Intrabiliary RF Heat-enhanced Local Chemotherapy of a Cholangiocarcinoma Cell Line: Monitoring with Dual-Modality Imaging—Preclinical Study,” *Radiology*, vol. 270, no. 2, pp. 400–408, Feb. 2014, doi: 10.1148/radiol.13130866.
[175] S. Curto *et al.*, “An integrated platform for small-animal hyperthermia investigations under ultra-high-field MRI guidance,” *Int. J. Hyperth. Off. J. Eur. Soc. Hyperthermic Oncol. North Am. Hyperth. Group*, pp. 1–11, Jul. 2017, doi: 10.1080/02656736.2017.1339126.
[176] Y. Yang *et al.*, “Microwave hyperthermia enhances the sensitivity of lung cancer cells to gemcitabine through reactive oxygen species-induced autophagic death,” *Oncol. Rep.*, vol. 41, no. 5, pp. 3100–3110, May 2019, doi: 10.3892/or.2019.7085.
[177] A. A. Petryk *et al.*, “Comparison of iron oxide nanoparticle and microwave hyperthermia alone or combined with cisplatinum in murine breast tumors,” *Proc. SPIE-- Int. Soc. Opt. Eng.*, vol. 7901, Feb. 2011, doi: 10.1117/12.876535.
[178] A. A. Petryk, A. J. Giustini, R. E. Gottesman, B. S. Trembly, and P. J. Hoopes, “Comparison of magnetic nanoparticle and microwave hyperthermia cancer treatment methodology and treatment effect in a rodent breast cancer model,” *Int. J. Hyperth. Off. J. Eur. Soc. Hyperthermic Oncol. North Am. Hyperth. Group*, vol. 29, no. 8, pp. 819–827, Dec. 2013, doi: 10.3109/02656736.2013.845801.
[179] D. B. Rodrigues, “Target-specific multiphysics modeling for thermal medicine applications,” 2013.
[180] S. Salahi, *Target-Specific Microwave Antenna Optimization for Pre-Clinical and Clinical Bladder Hyperthermia Devices*, vol. 73. 2012.
[181] J. Hew *et al.*, “The effects of dietary macronutrient balance on skin structure in aging male and female mice,” *PloS One*, vol. 11, no. 11, p. e0166175, 2016.
[182] C. A. Balanis, *Advanced engineering electromagnetics*. John Wiley & Sons, 1999.
[183] D. Haemmerich and D. J. Schutt, “RF ablation at low frequencies for targeted tumor heating: In vitro and computational modeling results,” *IEEE Trans. Biomed. Eng.*, vol. 58, no. 2, pp. 404–410, 2011.
[184] P. A. Hasgall, E. Neufeld, M. C. Gosselin, A. Klingenböck, and N. Kuster, “IT’IS Database for thermal and electromagnetic parameters of biological tissues,” *Version 30*, 2015.
[185] B. T. McWilliams, E. E. Schnell, S. Curto, T. M. Fahrbach, and P. Prakash, “A Directional Interstitial Antenna for Microwave Tissue Ablation: Theoretical and Experimental Investigation,” *IEEE Trans. Biomed. Eng.*, vol. 62, no. 9, pp. 2144–2150, Sep. 2015, doi: 10.1109/TBME.2015.2413672.
[186] J. Sebek, S. Curto, R. Bortel, and P. Prakash, “Analysis of minimally invasive directional antennas for microwave tissue ablation,” *Int. J. Hyperth. Off. J. Eur. Soc. Hyperthermic Oncol. North Am. Hyperth. Group*, vol. 33, no. 1, pp. 51–60, 2017, doi: 10.1080/02656736.2016.1195519.
[187] P. Faridi and P. Prakash, “Experimental Validation of Computational Models of Microwave Tissue Heating with Magnetic Resonance Thermometry,” in *2018 IEEE/MTT-S International Microwave Symposium-IMS*, 2018, pp. 1282–1284.

[188] C. Bing *et al.*, “Drift correction for accurate PRF-shift MR thermometry during mild hyperthermia treatments with MR-HIFU,” *Int. J. Hyperth. Off. J. Eur. Soc. Hyperthermic Oncol. North Am. Hyperth. Group*, vol. 32, no. 6, pp. 673–687, 2016, doi: 10.1080/02656736.2016.1179799.
[189] W. A. Grissom *et al.*, “Hybrid referenceless and multibaseline subtraction MR thermometry for monitoring thermal therapies in moving organs,” *Med. Phys.*, vol. 37, no. 9, pp. 5014–5026, 2010.
[190] A. Alivar, P. Faridi, P. Prakash, and B. Natarajan, “An enhanced hybrid MRI thermometry technique for monitoring microwave thermal therapy,” in *Medical Imaging 2019: Image-Guided Procedures, Robotic Interventions, and Modeling*, 2019, vol. 10951, p. 109512P.
[191] C. Bischoff-Everding, R. Soeder, and B. Neukirch, “Economic and clinical benefits of endometrial radiofrequency ablation compared with other ablation techniques in women with menorrhagia: a retrospective analysis with German health claims data,” *Int. J. Womens Health*, vol. 8, pp. 23–29, Jan. 2016, doi: 10.2147/IJWH.S89468.
[192] M. Y. Bongers, “Second-generation endometrial ablation treatment: Novasure,” *Best Pract. Res. Clin. Obstet. Gynaecol.*, vol. 21, no. 6, pp. 989–994, 2007.
[193] M. S. Baggish and P. Baltoyannis, “New techniques for laser ablation of the endometrium in high-risk patients,” *Am. J. Obstet. Gynecol.*, vol. 159, no. 2, pp. 287–292, Aug. 1988.
[194] “Heated balloon having a reciprocating fluid agitator,” Dec. 31, 1996.
[195] N. R. van der Walt, J. H. Xiao, and D. W. Vancelette, “Cryosurgical devices for endometrial ablation,” Jun. 2008.
[196] S. L. Corson, “A multicenter evaluation of endometrial ablation by Hydro ThermAblator and rollerball for treatment of menorrhagia,” *J. Am. Assoc. Gynecol. Laparosc.*, vol. 8, no. 3, pp. 359–367, Aug. 2001.
[197] M. G. Lubner, C. L. Brace, J. L. Hinshaw, and F. T. Lee Jr, “Microwave tumor ablation: mechanism of action, clinical results, and devices,” *J. Vasc. Interv. Radiol.*, vol. 21, no. 8, pp. S192–S203, 2010.
[198] H. Fallahi, J. Šebek, E. Frattura, J. Schenck, and P. Prakash, “Global microwave endometrial ablation for menorrhagia treatment,” Feb. 2017, p. 100660K, doi: 10.1117/12.2254097.
[199] J. Sebek, N. Albin, R. Bortel, B. Natarajan, and P. Prakash, “Sensitivity of microwave ablation models to tissue biophysical properties: A first step toward probabilistic modeling and treatment planning,” *Med. Phys.*, vol. 43, no. 5, p. 2649, May 2016, doi: 10.1118/1.4947482.
[200] V. Medikare, L. R. Kandukuri, V. Ananthapur, M. Deenadayal, and P. Nallari, “The Genetic Bases of Uterine Fibroids; A Review,” *J. Reprod. Infertil.*, vol. 12, no. 3, pp. 181–191, 2011.
[201] M. G. Munro, H. O. D. Critchley, M. S. Broder, I. S. Fraser, and for the FIGO Working Group on Menstrual Disorders, “FIGO classification system (PALM-COEIN) for causes of abnormal uterine bleeding in nongravid women of reproductive age,” *Int. J. Gynecol. Obstet.*, vol. 113, no. 1, pp. 3–13, Apr. 2011, doi: 10.1016/j.ijgo.2010.11.011.
[202] “Different Types of Fibroids and Myomas.” http://www.cmdrc.com/menstrual-disorders-fibroids/fibroids/no-two-fibroids-are-alike/ (accessed Feb. 01, 2018).
[203] C. Amabile *et al.*, “Microwave ablation of primary and secondary liver tumours: ex vivo, in vivo, and clinical characterisation,” *Int. J. Hyperth. Off. J. Eur. Soc. Hyperthermic*

*Oncol. North Am. Hyperth. Group*, vol. 33, no. 1, pp. 34–42, Feb. 2017, doi: 10.1080/02656736.2016.1196830.
[204] K. R. Foster and J. L. Schepps, "Dielectric properties of tumor and normal tissues at radio through microwave frequencies," *J. Microw. Power*, vol. 16, no. 2, pp. 107–119, Jun. 1981.
[205] J. L. Schepps and K. R. Foster, "The UHF and microwave dielectric properties of normal and tumour tissues: variation in dielectric properties with tissue water content," *Phys. Med. Biol.*, vol. 25, no. 6, pp. 1149–1159, Nov. 1980.
[206] M. Cavagnaro, C. Amabile, P. Bernardi, S. Pisa, and N. Tosoratti, "A minimally invasive antenna for microwave ablation therapies: design, performances, and experimental assessment," *IEEE Trans. Biomed. Eng.*, vol. 58, no. 4, pp. 949–959, 2010.
[207] M. Cavagnaro, C. Amabile, S. Cassarino, N. Tosoratti, R. Pinto, and V. Lopresto, "Influence of the target tissue size on the shape of ex vivo microwave ablation zones," *Int. J. Hyperthermia*, vol. 31, no. 1, pp. 48–57, 2015.
[208] C. L. Brace, "Dual-slot antennas for microwave tissue heating: Parametric design analysis and experimental validation," *Med. Phys.*, vol. 38, no. 7, pp. 4232–4240, 2011.
[209] J. Chiang, P. Wang, and C. L. Brace, "Computational modelling of microwave tumour ablations," *Int. J. Hyperthermia*, vol. 29, no. 4, pp. 308–317, 2013.
[210] V. Lopresto, R. Pinto, G. A. Lovisolo, and M. Cavagnaro, "Changes in the dielectric properties of ex vivo bovine liver during microwave thermal ablation at 2.45 GHz," *Phys. Med. Biol.*, vol. 57, no. 8, p. 2309, 2012.
[211] Z. Ji and C. L. Brace, "Expanded modeling of temperature-dependent dielectric properties for microwave thermal ablation," *Phys. Med. Biol.*, vol. 56, no. 16, p. 5249, 2011.
[212] P. Wang and C. L. Brace, "Tissue dielectric measurement using an interstitial dipole antenna," *IEEE Trans. Biomed. Eng.*, vol. 59, no. 1, pp. 115–121, 2011.
[213] M. Cavagnaro, R. Pinto, and V. Lopresto, "Numerical models to evaluate the temperature increase induced by ex vivo microwave thermal ablation," *Phys. Med. Biol.*, vol. 60, no. 8, pp. 3287–3311, Apr. 2015, doi: 10.1088/0031-9155/60/8/3287.
[214] G. R. Lyons and B. B. Pua, "Ablation Planning Software for Optimizing Treatment: Challenges, Techniques, and Applications," *Tech. Vasc. Interv. Radiol.*, vol. 22, no. 1, pp. 21–25, Mar. 2019, doi: 10.1053/j.tvir.2018.10.005.
[215] D. Fuentes, C. Walker, A. Elliott, A. Shetty, J. D. Hazle, and R. J. Stafford, "Magnetic resonance temperature imaging validation of a bioheat transfer model for laser-induced thermal therapy," *Int. J. Hyperthermia*, vol. 27, no. 5, pp. 453–464, 2011.
[216] T. P. Ryan and C. L. Brace, "Interstitial microwave treatment for cancer: historical basis and current techniques in antenna design and performance," *Int. J. Hyperthermia*, vol. 33, no. 1, pp. 3–14, 2017.
[217] G. C. Kagadis, K. Katsanos, D. Karnabatidis, G. Loudos, G. C. Nikiforidis, and W. R. Hendee, "Emerging technologies for image guidance and device navigation in interventional radiology," *Med. Phys.*, vol. 39, no. 9, pp. 5768–5781, 2012.
[218] W. Zhai, J. Xu, Y. Zhao, Y. Song, L. Sheng, and P. Jia, "Preoperative surgery planning for percutaneous hepatic microwave ablation," in *International Conference on Medical Image Computing and Computer-Assisted Intervention*, 2008, pp. 569–577.
[219] J. A. Pearce, "Models for thermal damage in tissues: processes and applications," *Crit. Rev. Biomed. Eng.*, vol. 38, no. 1, 2010.

[220] C. Rossmanna and D. Haemmerich, “Review of temperature dependence of thermal properties, dielectric properties, and perfusion of biological tissues at hyperthermic and ablation temperatures,” *Crit. Rev. Biomed. Eng.*, vol. 42, no. 6, pp. 467–492, 2014, doi: 10.1615/critrevbiomedeng.2015012486.
[221] “Reporting of Computational Modeling Studies in Med.pdf.” Accessed: May 20, 2020. [Online]. Available: https://www.fda.gov/media/87586/download.
[222] J. Egger *et al.*, “RFA-cut: Semi-automatic segmentation of radiofrequency ablation zones with and without needles via optimal st-cuts,” in *2015 37th Annual International Conference of the IEEE Engineering in Medicine and Biology Society (EMBC)*, 2015, pp. 2423–2429.
[223] A. Pfannenstiel, T. Keast, S. Kramer, H. Wibowo, and P. Prakash, “Flexible microwave ablation applicator for the treatment of pulmonary malignancies,” in *Energy-based Treatment of Tissue and Assessment IX*, Feb. 2017, vol. 10066, p. 100660M, doi: 10.1117/12.2255504.
[224] R. D. Peters and R. M. Henkelman, “Proton-resonance frequency shift MR thermometry is affected by changes in the electrical conductivity of tissue,” *Magn. Reson. Med. Off. J. Int. Soc. Magn. Reson. Med.*, vol. 43, no. 1, pp. 62–71, 2000.
[225] L. Chen, J. P. Wansapura, G. Heit, and K. Butts, “Study of laser ablation in the in vivo rabbit brain with MR thermometry,” *J. Magn. Reson. Imaging Off. J. Int. Soc. Magn. Reson. Med.*, vol. 16, no. 2, pp. 147–152, 2002.
[226] L. G. Merckel *et al.*, “First clinical experience with a dedicated MRI-guided high-intensity focused ultrasound system for breast cancer ablation,” *Eur. Radiol.*, pp. 1–10, 2016.
[227] R. Hoffmann *et al.*, “Preclinical evaluation of an MR-compatible microwave ablation system and comparison with a standard microwave ablation system in an ex vivo bovine liver model,” *Int. J. Hyperthermia*, vol. 33, no. 6, pp. 617–623, 2017.
[228] J. C. Chen *et al.*, “Prostate cancer: MR imaging and thermometry during microwave thermal ablation-initial experience,” *Radiology*, vol. 214, no. 1, pp. 290–297, 2000.
[229] J. A. Moriarty *et al.*, “MRI monitoring of interstitial microwave-induced heating and thermal lesions in rabbit brain in vivo,” *J. Magn. Reson. Imaging JMRI*, vol. 8, no. 1, pp. 128–135, Feb. 1998, doi: 10.1002/jmri.1880080125.
[230] R. T. Peters, R. S. Hinks, and R. M. Henkelman, “Ex vivo tissue-type independence in proton-resonance frequency shift MR thermometry,” *Magn. Reson. Med.*, vol. 40, no. 3, pp. 454–459, 1998.
[231] Y. Zhang, M. E. Poorman, and W. A. Grissom, “Dual-echo Z-shimmed proton resonance frequency-shift magnetic resonance thermometry near metallic ablation probes: Technique and temperature precision,” *Magn. Reson. Med.*, vol. 78, no. 6, pp. 2299–2306, Dec. 2017, doi: 10.1002/mrm.26634.
[232] H. Fallahi, D. Clausing, A. Shahzad, M. O’Halloran, M. C. Dennedy, and P. Prakash, “Microwave antennas for thermal ablation of benign adrenal adenomas,” *Biomed. Phys. Eng. Express*, vol. 5, no. 2, p. 025044, Feb. 2019, doi: 10.1088/2057-1976/ab068b.
[233] G. Shafirstein *et al.*, “Conductive interstitial thermal therapy device for surgical margin ablation: in vivo verification of a theoretical model,” *Int. J. Hyperth. Off. J. Eur. Soc. Hyperthermic Oncol. North Am. Hyperth. Group*, vol. 23, no. 6, pp. 477–492, Sep. 2007, doi: 10.1080/02656730701591476.

[234] A. Bhattacharya and R. L. Mahajan, “Temperature dependence of thermal conductivity of biological tissues,” *Physiol. Meas.*, vol. 24, no. 3, pp. 769–783, Aug. 2003, doi: 10.1088/0967-3334/24/3/312.
[235] S. K. Hall, E. H. Ooi, and S. J. Payne, “Cell death, perfusion and electrical parameters are critical in models of hepatic radiofrequency ablation,” *Int. J. Hyperthermia*, vol. 31, no. 5, pp. 538–550, 2015.
[236] A. Pfannenstiel *et al.*, “Directional Microwave Ablation: Experimental Evaluation of a 2.45-GHz Applicator in Ex Vivo and In Vivo Liver,” *J. Vasc. Interv. Radiol. JVIR*, Mar. 2020, doi: 10.1016/j.jvir.2020.01.016.
[237] R. Hoffmann *et al.*, “In vitro artefact assessment of a new MR-compatible microwave antenna and a standard MR-compatible radiofrequency ablation electrode for tumour ablation,” *Eur. Radiol.*, vol. 26, no. 3, pp. 771–779, Mar. 2016, doi: 10.1007/s00330-015-3891-0.
[238] V. Lopresto, R. Pinto, L. Farina, and M. Cavagnaro, “Microwave thermal ablation: Effects of tissue properties variations on predictive models for treatment planning,” *Med. Eng. Phys.*, vol. 46, pp. 63–70, 2017, doi: 10.1016/j.medengphy.2017.06.008.
[239] D. Yang, M. C. Converse, D. M. Mahvi, and J. G. Webster, “Expanding the bioheat equation to include tissue internal water evaporation during heating,” *IEEE Trans. Biomed. Eng.*, vol. 54, no. 8, pp. 1382–1388, 2007.
[240] C. L. Brace, T. A. Diaz, J. L. Hinshaw, and F. T. Lee Jr, “Tissue contraction caused by radiofrequency and microwave ablation: a laboratory study in liver and lung,” *J. Vasc. Interv. Radiol.*, vol. 21, no. 8, pp. 1280–1286, 2010.
[241] C. M. Sommer *et al.*, “Quantification of tissue shrinkage and dehydration caused by microwave ablation: experimental study in kidneys for the estimation of effective coagulation volume,” *J. Vasc. Interv. Radiol.*, vol. 24, no. 8, pp. 1241–1248, 2013.
[242] H. Fallahi, J. Sebek, and P. Prakash, “Broadband Dielectric Properties of Ex Vivo Bovine Liver Tissue Characterized at Ablative Temperatures,” *IEEE Trans. Biomed. Eng.*, 2020.
[243] A. Alivar, P. Faridi, P. Prakash, and B. Natarajan, “An enhanced hybrid MRI thermometry technique for monitoring microwave thermal therapy,” in *Medical Imaging 2019: Image-Guided Procedures, Robotic Interventions, and Modeling*, 2019, vol. 10951, p. 109512P.
[244] W. A. Grissom *et al.*, “Hybrid referenceless and multibaseline subtraction MR thermometry for monitoring thermal therapies in moving organs,” *Med. Phys.*, vol. 37, no. 9, pp. 5014–5026, Sep. 2010, doi: 10.1118/1.3475943.
[245] K. K. Vigen, B. L. Daniel, J. M. Pauly, and K. Butts, “Triggered, navigated, multi-baseline method for proton resonance frequency temperature mapping with respiratory motion,” *Magn. Reson. Med.*, vol. 50, no. 5, pp. 1003–1010, Nov. 2003, doi: 10.1002/mrm.10608.
[246] S. S. Evans, E. A. Repasky, and D. T. Fisher, “Fever and the thermal regulation of immunity: the immune system feels the heat,” *Nat. Rev. Immunol.*, vol. 15, no. 6, pp. 335–349, Jun. 2015, doi: 10.1038/nri3843.
[247] A. Jolesch, K. Elmer, H. Bendz, R. D. Issels, and E. Noessner, “Hsp70, a messenger from hyperthermia for the immune system,” *Eur. J. Cell Biol.*, vol. 91, no. 1, pp. 48–52, Jan. 2012, doi: 10.1016/j.ejcb.2011.02.001.
[248] K. Hynynen, “Hyperthermia-induced drug delivery in humans,” *Nat. Biomed. Eng.*, vol. 2, no. 9, pp. 637–639, 2018, doi: 10.1038/s41551-018-0297-8.

[249] D. Haemmerich, “Non-invasive image-guided targeted drug delivery,” *Lancet Oncol.*, vol. 19, no. 8, pp. 1000–1001, 2018, doi: 10.1016/S1470-2045(18)30419-4.
[250] D. Haemmerich and A. Motamarry, “Thermosensitive Liposomes for Image-Guided Drug Delivery,” *Adv. Cancer Res.*, vol. 139, pp. 121–146, 2018, doi: 10.1016/bs.acr.2018.04.004.
[251] P. Faridi, S. H. Bossmann, and P. Prakash, “Simulation-based design and characterization of a microwave applicator for MR-guided hyperthermia experimental studies in small animals,” *Biomed. Phys. Eng. Express*, vol. 6, no. 1, p. 015001, Nov. 2019, doi: 10.1088/2057-1976/ab36dd.

# Appendix A - Experimental assessment of microwave ablation computational modeling with MR thermometry – Supplementary data

To evaluate the modelled water flow in the MWA applicator during the course of heating, we measured temperature of water at the applicator inlet and outlet during ablation experiment. When using an input power of 30 W (at the applicator), change in temperature of the inflowing water was ~ 1 - 2 ˚C over the duration of the 10 min experiment. During the 5 min ablation experiment at 50 W, change in temperature of inflowing water was ~ 1 ˚C. The figure below shows the measured temperature changes for inflowing/outflowing water during the experiments. Based on these experiments, we anticipate a 1 ˚C change in the circulating water temperature, and that these would not be expected to have a significant effect on tissue temperatures and ablation zone extents.

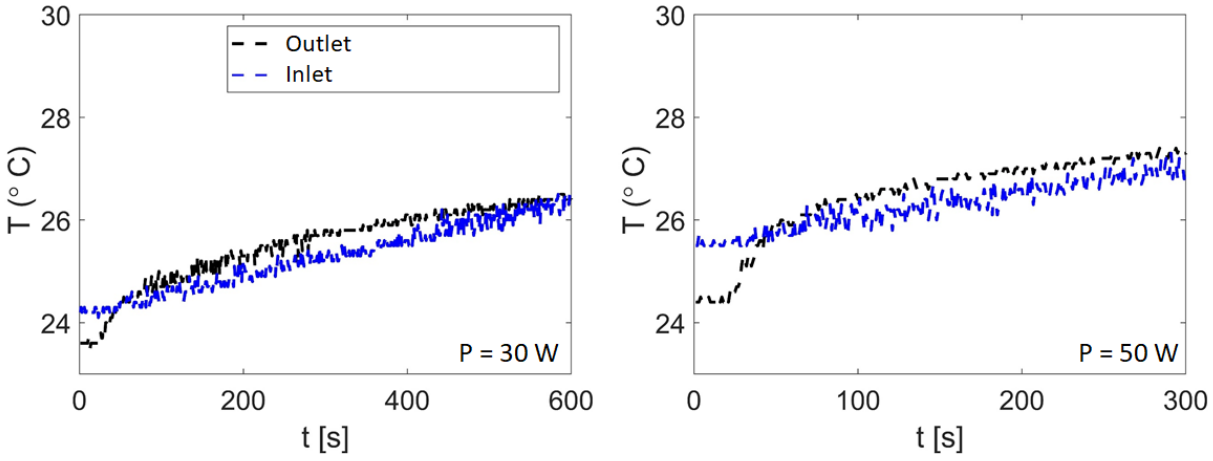


**Fig. A.S.1.** Experimental transient temperature measurments with fiber-optic temperature sensors in the inlet and outlet of circulating water of MWA applicator.

To assess the potential impact of susceptibility artifact on the uncertainty of MR thermometry in proximity to the antenna, we compared the uncertainty of temperature measurements in an agar phantom, in ROIs positioned in proximity to (5 mm) and distant from (27 mm) the applicator (see Fig. A.S.2). With no applied microwave power, the temperature change in all regions of the phantom was anticipated to be zero. As shown in the figure, the standard deviation in the proximity (5 mm) of MWA applicator over time is in the range of 0.38 – 0.47 °C while the standard deviation further away from the applicator (27 mm) is in the range of 0.37 – 0.41 °C. The difference between the temperature change in the ROIs close to the applicator and ROIs further away is minimal. Thus, we concluded that the susceptibility artifacts in proximity to the applicator had negligible impact on MR thermometry.

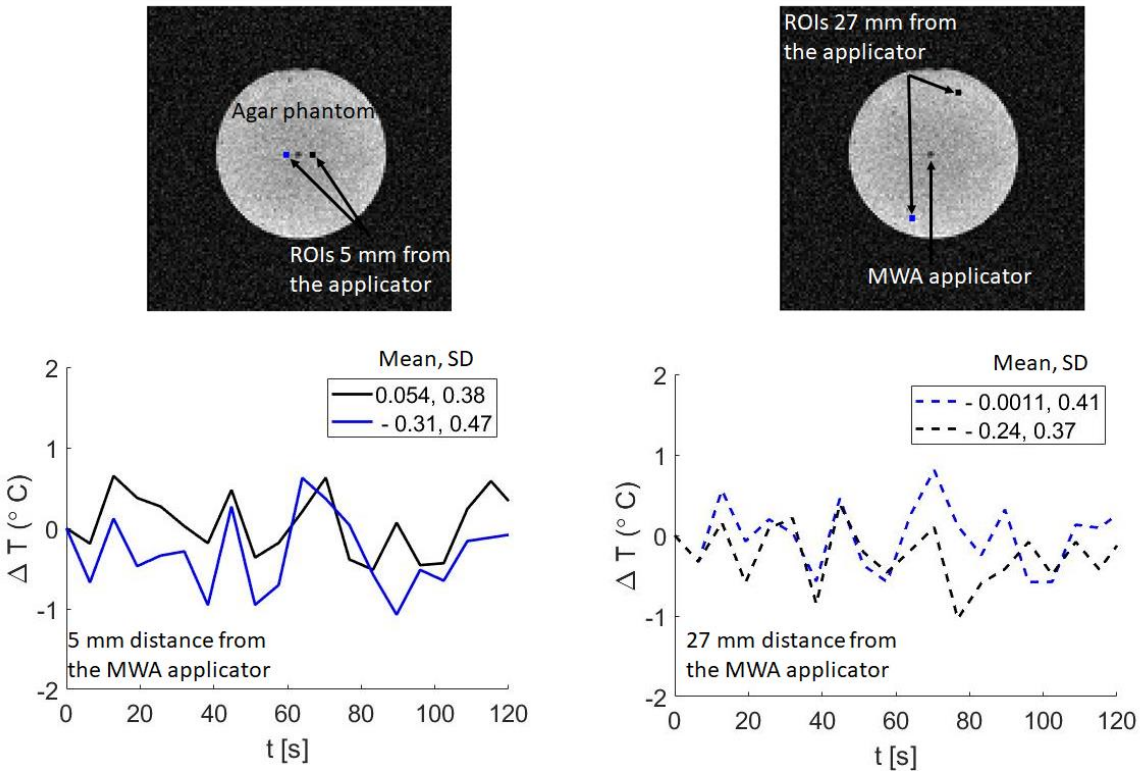


**Fig. A.S.2.** MRT-measured transient temperature in agar phantom in ROIs in the proximity (5 mm) and distant (27 mm) from the MWA applicator in the absence of heat.